Chapter 2

Copper(II) complexes with hydrazide blocking ligands

Part (A): Pseudohalides copper(II) complexes with a hydrazide blocking ligand: Synthesis, spectral characterization and evaluation of antioxidant superoxide dismutase activity

1 Introduction

Hydrazone complexes of transition metal complexes are known to furnish useful models for the illumination of the mechanism of enzyme inhibition of hydrazine derivatives [1] and their probable pharmacological applications [2, 3]. In addition, hydrazone complexes have been studied for many years owing to their antitumor and antibacterial activities [4-10]. In recent times, it is established that such potential ligands can act as effective catalysts towards the alkene epoxidation [11] and as binders to transition metals [2, 12].

In this chapter, our aim is the synthesis and spectral characterization of copper(II) complexes with hydrazone and pseudo halides as co-ligands. The coordination sites of copper(II) ion prefer square pyramidal geometry, which is generally blocked by tridentate Schiff bases. To saturate the coordination number of the copper(II) ion a bridging ligand *viz* (N3, NCS, NCO) is used. Several transition metal complexes with tridentate and bridging ligands (pseudo halides) have already been reported [13-21]. These pseudohalides bridged complexes have got diverse structures and potential applications in magnetic materials. Pseudo halide ligands can coordinate to transition metal ions in different ways. For two ions the most common modes are (i) end-to-end and (ii) end-on fashion (Scheme 1).

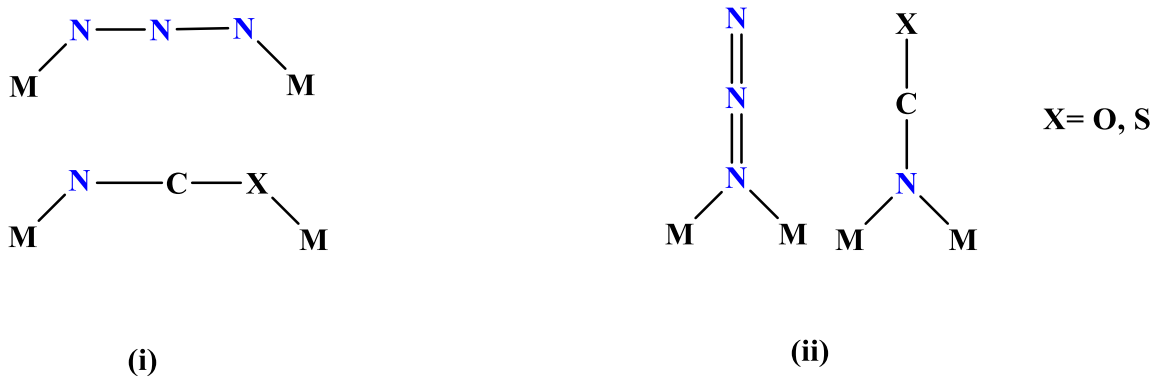

Scheme 1 Common bridging modes of pseudohalides.

The end-on coordination is often found in cynato [22-39] and end-to-end thiocynato in bridged complexes [21, 30-35]. Whereas end-on coordination mode is most common in azido bridged complexes [20, 36-38]. The HL acts as a potentially tridentate blocking ligand and can coordinate to a metal ion *viz.*, the pyridine nitrogen, the imine nitrogen and the amide oxygen atoms [39-41]. Furthermore, this ligand exhibits keto-enol tautomerism [41]. (Scheme 2).

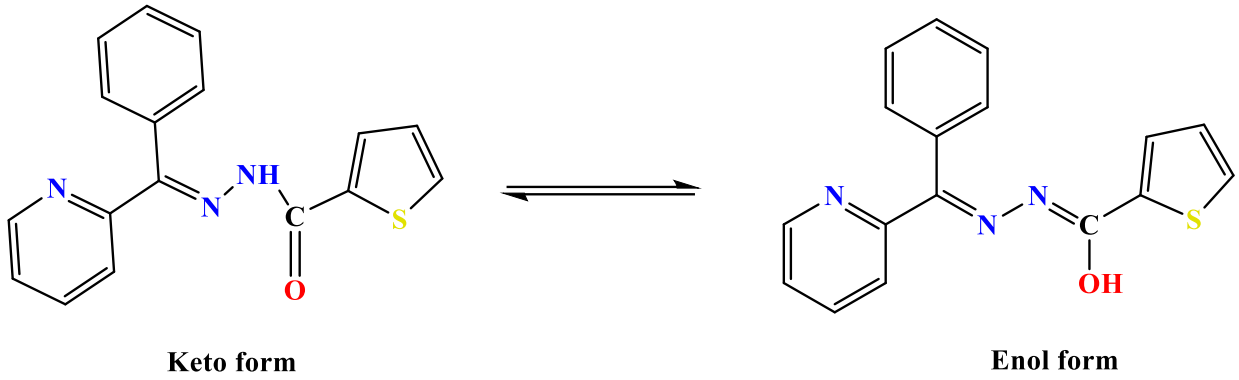

Scheme 2 Keto-enol form of HL.

In this chapter using (E)-N'-(phenyl(pyridin-2-yl)methylene)thiophene-2-carbohydrazide (HL) ligand, four copper(II) mono and binuclear complexes like $[Cu(L)(ClO_4)(H_2O)]$ (**1**), $[(Cu)(L)(N_3)]_2$ (**2**), $[(Cu)(L)(OCN)]_2$ (**3**), and $[(Cu)(L)(CNS)]_2$ (**4**) have been synthesized and characterized using UV-vis, infrared and Epr spectroscopic techniques. The electrochemical behaviour of these complexes was also studied using cyclic and differentials pulse voltammetry (CV and DPV). Additionally, the antioxidant superoxide dismutase (SOD) activity of these complexes has been also evaluated.

2 Experimental

2.1 Synthesis of ligand (HL)

The pro-ligand was synthesized by condensing thiophene-2-carboxylic acid hydrazide (0.71 g, 10 mmol) with 2-benzoyl pyridine (0.96 g, 10 mmol) in ethanol 40 mL according to the procedure as reported previously [42, 43]. The reaction mixture was refluxed for 3 hrs. The resulting solution was filtered and filtrate left for evaporation at RT, whereas solid mass was obtained. The obtained solid mass was washed with cold ethanol and stored in calcium chloride desiccators. The ligand was characterized by elemental analysis and the NMR method.

M.P.: 125°C. Yield ~ 80%. Molecular Weight: 307.37. Anal. Calc. for $C_{17}H_{13}N_3OS$: C, 66.43; H, 4.26; N, 13.67%. Found: C, 66.49; H, 4.24; N, 13.69%. FTIR (KBr, cm^{-1}): ν(NH) 3174, ν(OH) 3306, ν(C=O) 1645, ν(C=N) 1604. ^{1}H NMR (DMSO-d_6, 400MHz) δ: 11.3 (s, 1H, -NH-), 9.1 (s, 1H, -CH=N-), 8.9 (s, 1H, -CH-S-), 8.5-7.1 (m, 10H, Ar-H) ppm. ^{13}C NMR

(DMSO-d_6, 400MHz) δ: 185.9 (C=O), 156.8 (Ar-C, -C=C), 149 (-CH=N), 138.1 (-CH-S), 148-116 (Ar-C) ppm.

2.2 Synthesis of complex $[Cu(L)(ClO_4)(H_2O)]$ 1

To a 10 mL methanolic solution of $Cu(ClO_4).6H_2O$ (0.370g, 1 mmol) was added 10 mL methanol solution of HL (0.307g, 1 mmol) and stirred for 1 hrs. The mixture was filtered and the filtrate was left for evaporation at room temperature. After one-week blue coloured complex separated. The product was collected by filtration, washed with cold methanol and stored in calcium chloride desiccators.

Yield ~ 74%. Molecular Weight: 487.37. Anal. Calc. for $C_{17}H_{14}ClCuN_3O_6S$: C, 41.88; H, 2.89; N, 8.61%. Found: C, 41.90; H, 2.90; N, 8.62%. FTIR bands (KBr, cm^{-1}): ν(C=N) 1575, ν(C−O¯) 1292**,** ν(ClO_4^-) 1073. ESI-Mass (m/z): 487.12.

2.3 Synthesis of complex $[Cu(L)(N_3)]_2$ 2

To a 20 mL methanolic solution of $Cu(ClO_4).6H_2O$ (0.379 g, 1 mmol) and HL (0.307 g, 1 mmol) were added sodium azide (0.065 g, 1 mmol) solution prepared in a minimum volume of water and methanol. The reaction mixture was stirred for 1 hrs and filtered. The filtrate was left for slow evaporation in the air at room temperature. After few days polycrystalline green product was obtained. The product was collected by filtration, washed with methanol and dried in calcium chloride desiccators.

Yield ~ 68%. Molecular Weight: 823.86. Anal. Calc. for $C_{34}H_{24}Cu_2N_{12}O_2S_2$: C, 49.57; H, 2.94; N, 20.40%. Found: C, 49.59; H, 2.90; N, 20.46%. FTIR bands (KBr, cm^{-1}): ν(C=N) 1572, ν(C−O¯) 1289. ESI-Mass (m/z): 825.52.

2.4 Synthesis of complex $[Cu(L)(OCN)]_2$ 3

Complex **3** was prepared similarly as discussed for **2**, except that sodium cyanate (0.065 g, 1 mmol) was used in place of sodium azide. Green microcrystalline powder collected by filtration and stored in calcium chloride desiccators.

Yield ~ 76%. Molecular Weight: 823.85. Anal. Calc. for $C_{36}H_{24}Cu_2N_8O_2S_4$: C, 52.49; H, 2.98; N, 13.61%. Found: C, 52.48; H, 2.94; N, 13.60%. FTIR bands (KBr, cm^{-1}): ν(C=N) 1573, ν(C−O¯) 1285. ESI-Mass (m/z): 823.45.

2.5 Synthesis of $[Cu(L)(CNS)]_2$ 4

This complex was synthesized by following similar methods as described for complex **2** and **3**. In this synthesis potassium thiocyanate (0.097 g, 1 mmol) was used. The green coloured microcrystalline powder was separated after a week. The product was filtered, washed with methanol and kept in calcium chloride desiccators.

Yield ~ 79%. Molecular Weight: 855.97. Anal. Calc. for $C_{36}H_{24}Cu_2N_8O_4S_4$: C, 50.52; H, 2.83; N, 13.09%; Found C, 50.54; H, 2.85; N, 13.10%. FTIR bands (KBr, cm^{-1}): ν(C=N) 1599, ν(C−O¯) 1289. ESI-Mass (m/z): 855.97.

2.6 Physical measurements

Infrared (FTIR) spectra were recorded on a Bruker spectrophotometer at normal temperature. KBr pellets were prepared by grinding the sample with KBr (IR grade), in the range of 400 to 4000 cm^{-1}. NMR spectra of HL were recorded in DMSO-d_6 on Bruker Advance 400 (FT-NMR) multinuclear spectrometer. Electronic absorption spectra (300–900 nm) were recorded with a Shimadzu UV-Vis recording spectrophotometer UV-1601 in solution. The electrochemistry of the complex (3×10^{-3} M) in DMSO containing 0.1 M tetra-butylammonium perchlorate (TBAP) as supporting electrolyte was determined at room temperature by cyclic voltammetry (CV) using a three-electrode system under de-aerated conditions and a BAS 100 electrochemical analyser. A glassy-carbon electrode and platinum wire were used as the working electrode and the counter electrode, respectively. The reversibility of the electrochemical process was evaluated by standard procedures and all potentials were recorded against an Ag/AgCl reference electrode. All measurements were carried out at 298 K under nitrogen. All solutions were purged with nitrogen gas before measurements. The low and room temperature electron paramagnetic resonance (EPR) spectra were obtained with a Varian E-line Century Series Spectrometer equipped with a dual cavity and operating at X-band with 100 kHz modulation frequency. Varian quartz tubes were used for obtaining the EPR spectra of the polycrystalline samples and frozen solutions with tetracyanoethylene (TCNE) as a marker (g = 2.00277).

2.7 Computational method

Full geometry optimizations were carried out using the density functional theory (DFT) method at the B3LYP level for complex [44]. All elements except Cu were assigned the 6-31G(d) basis set [45]. LANL2DZ with effective core potential for Cu atom was used

[46]. The vibrational frequency calculations were performed to ensure that the optimized geometries represent the local minima and that there is only a positive Eigenvalue. In the computational model, the cationic complex was taken into account. All calculations were performed with the GAUSSIAN09 program [47], with the aid of the Gauss View visualization program. Vertical electronic excitations based on B3LYP optimized geometries were computed using the time-dependent density functional theory (TDDFT) formalism [48] in DMSO, using a conductor-like polarizable continuum model (CPCM) [49].

3 Results and discussion

3.1 Synthesis and general aspects

The tridentate hydrazone ligand (HL) was synthesized by the condensation of thiophenes-2-carboxylic acid hydrazide and 2-benzoyl pyridine following the reported method (Scheme 3) [42, 43]. The monocondensed hydrazone ligand (HL), on reaction with copper perchlorate hexahydrate and different pseudo halides, gave complexes as shown in Scheme 4. The ligand and complexes were characterized from their analytical and physicochemical data as given in the experimental section. The molar conductance data exhibit the non-ionic nature of complexes (**1-4**). These complexes are air-stable and soluble in polar solvents but sparingly soluble in non-polar solvents.

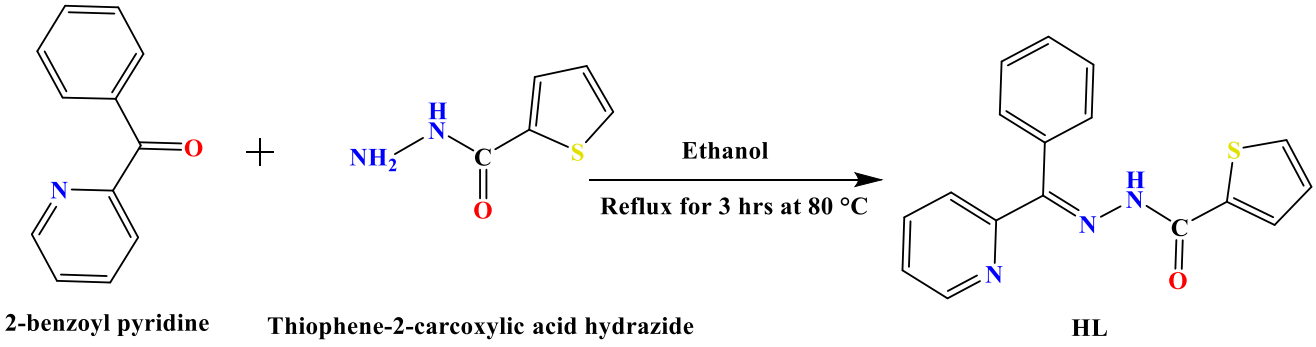

Scheme 3 Synthesis of hydrazone ligand **HL**.

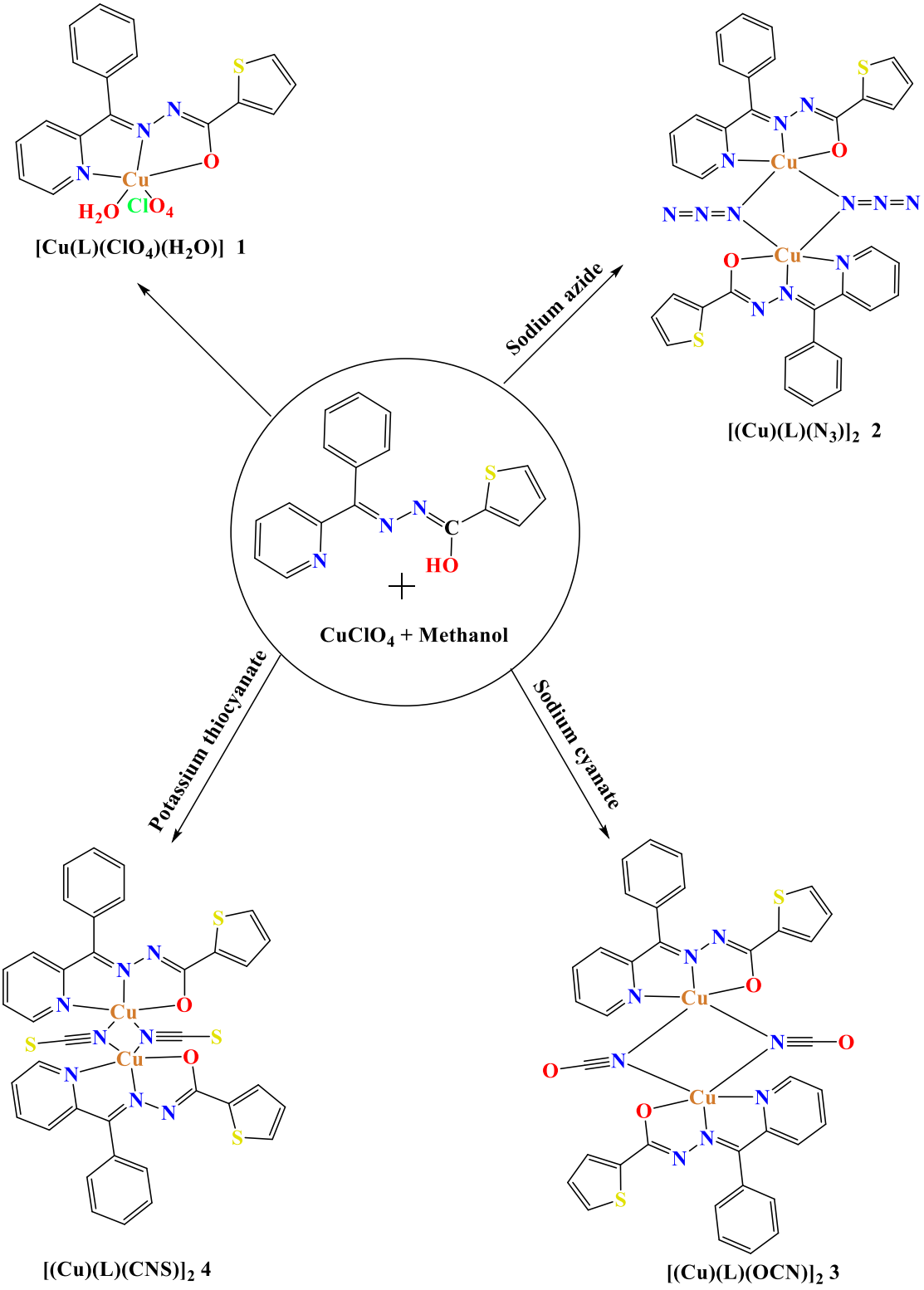

Scheme 4 Synthetic route of complexes **1-4**.

3.2 NMR spectra of ligand

The ^{1}H NMR and ^{13}C NMR of ligand were recorded in DMSO-d_6 solvent. The NMR spectra of the ligand give the right information of the ligand structure. In ^{1}H NMR of ligand we find a singlet peak at 11.3 ppm is due to hydrazide (-NH-) proton. Similarly, azomethine (-CH=N-) proton peak is observed at 9.1 ppm and (-CH-S) peak is obtained at 8.9 ppm. All other aromatic protons peaks are observed in the range of 8.5-7.1 ppm. ^{1}H NMR spectrum is shown in (Fig. 1). In ^{13}C NMR spectra, we find that carbonyl carbon peak at 185.9 ppm, (C=C) peak is obtained at 156 ppm, Similarly, azomethine carbon peak at 149 ppm and (CH-S) carbon peak is obtained at 138.1 ppm. All other aromatic carbon peaks are observed in the range of 156-116 ppm. ^{13}C NMR spectrum is shown in (Fig. 2).

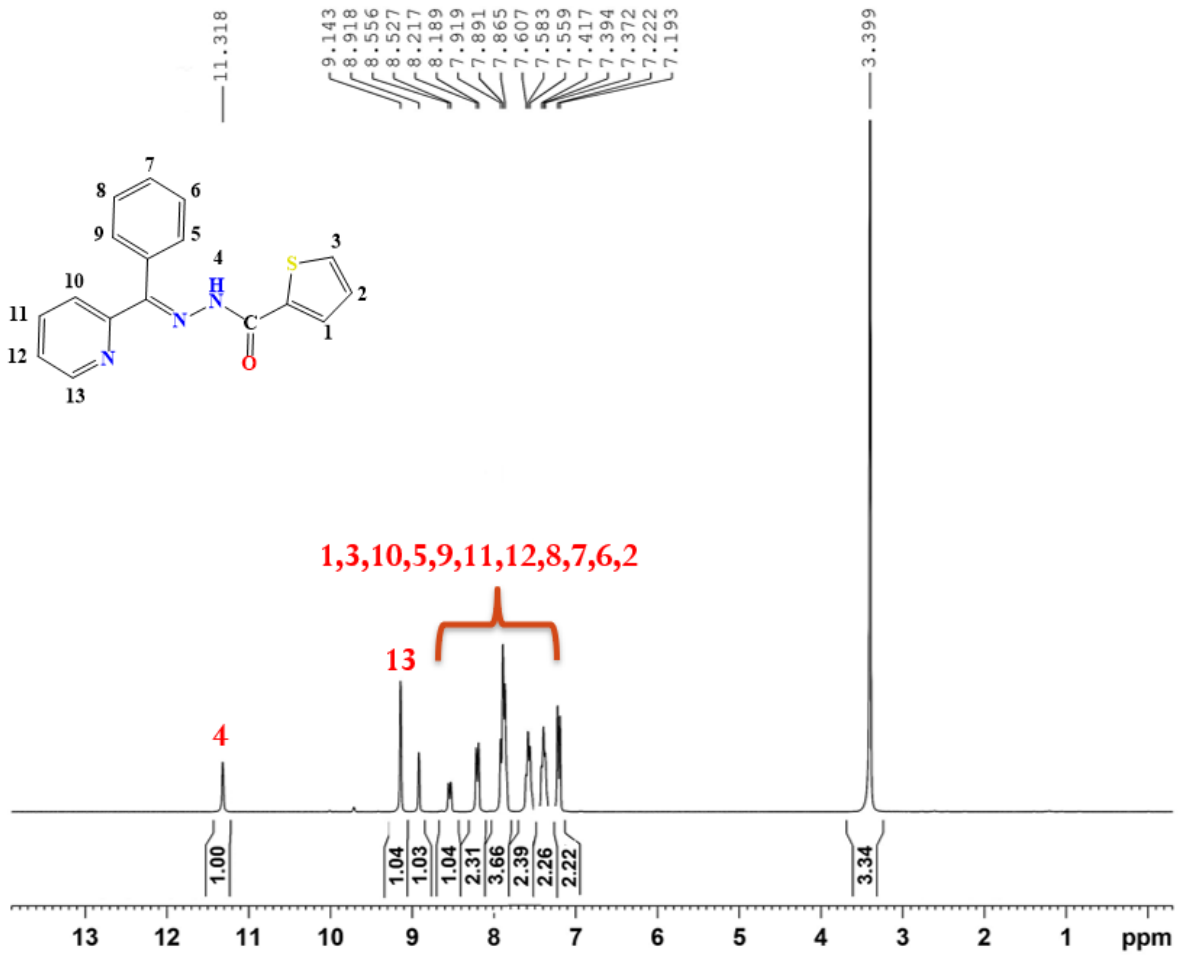

Fig. 1. ^{1}H NMR of ligand **HL**.

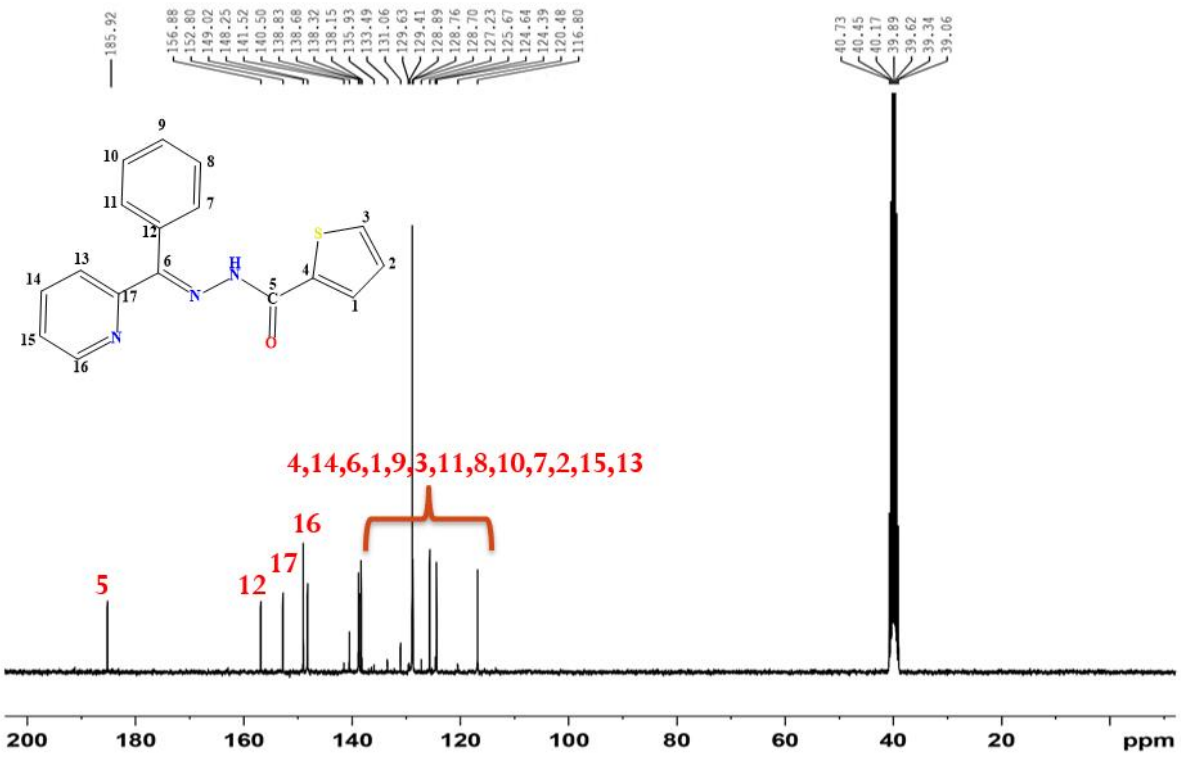

Fig. 2. ^{13}C NMR of ligand **HL**.

3.3 FTIR Spectral studies

FTIR spectra of complexes (**1-4**) were analysed in comparison to free unbound ligand (HL). The FTIR spectrum of the HL shows a band ~ 3174 cm^{-1} due to ν(N-H) and ν(OH) at 3306 cm^{-1}. The FTIR band at ~1604 cm^{-1} indicates the presence of the ν(>C=N) group. The FTIR spectra of complexes (**1-4**) show absorption bands in the 1572-1599 cm^{-1} region, which can be assigned to the >C=N stretching frequency of the coordinated L. The shift of this absorption band on complexation towards lower wave number reveals the coordination of the azomethine nitrogen to the copper centre [50]. The absence of 3174 ν(N−H) and ν(C=O) bands and appearance of a new ν(C−O^{-}) band in the range 1292-1285 cm^{-1} in all the metal complexes indicate that the ligand enolizes during complexation and bonding occurs through a deprotonated enolate-O with metal. Complex **1** shows a band at 620 and 1100 cm^{-1} due to coordinated perchlorate anion to copper centre. The band observed at 3418 cm^{-1} in **1** is due to coordinated water. FTIR spectrum of the complexes showed a strong absorption band at 2018 cm^{-1}indicating azido ligand, sodium cyanate at 2016 cm^{-1} and a band at 1959 cm^{-1} indicating thiocyanate ligands [51]. The FTIR spectrum of complexes shows two bands at 2110 and 2138 cm^{-1} indicating the presence of bridging thiocyanate [52]. The ligand coordination to the

copper centre is confirmed by two peaks are seen in IR spectrum of each complex, at 406-491 cm^{-1} and 423-467 cm^{-1} due to ν(Cu-N) and ν(Cu-O) respectively. The FTIR peaks of ligand and complexes are shown in Table 1 and spectra are shown in Fig. 3-7.

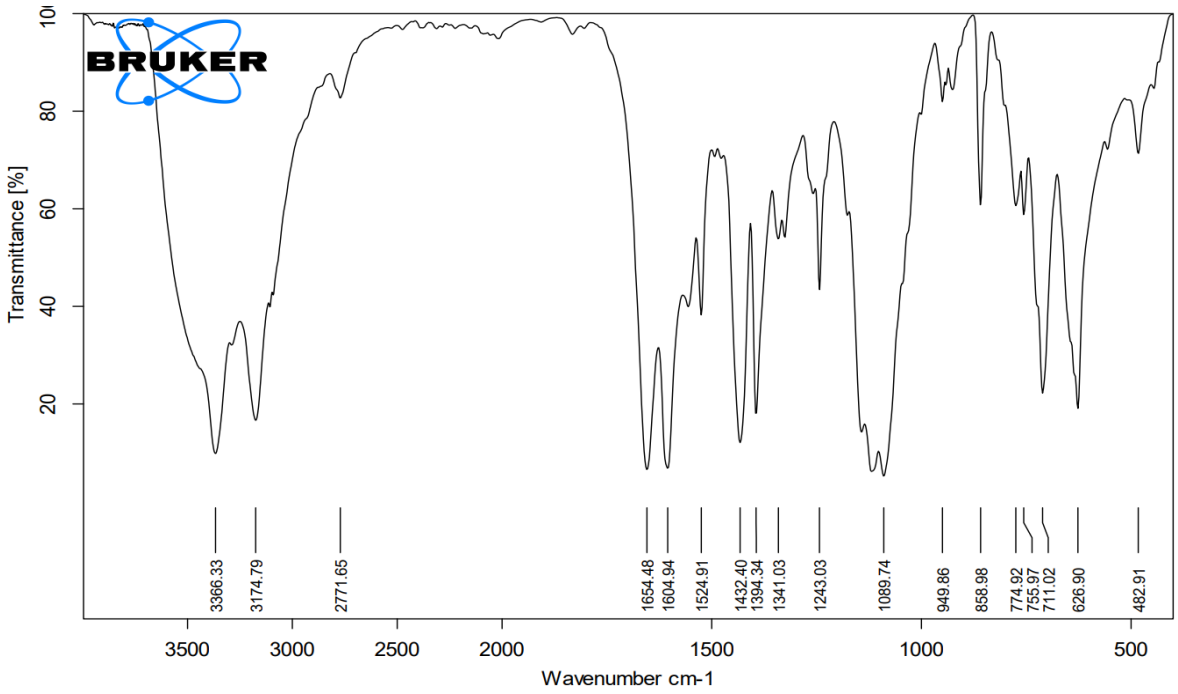

Fig. 3. FTIR spectrum of Ligand (**HL**).

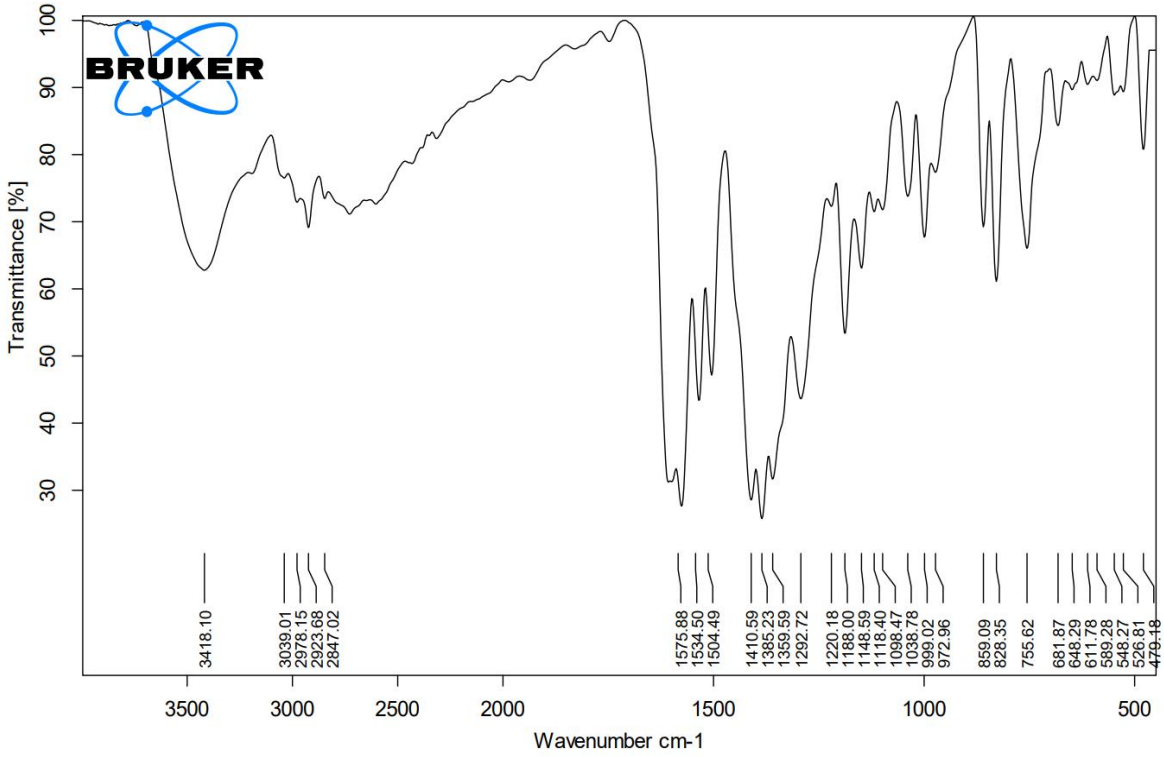

Fig. 4. FTIR spectrum of complex **1**.

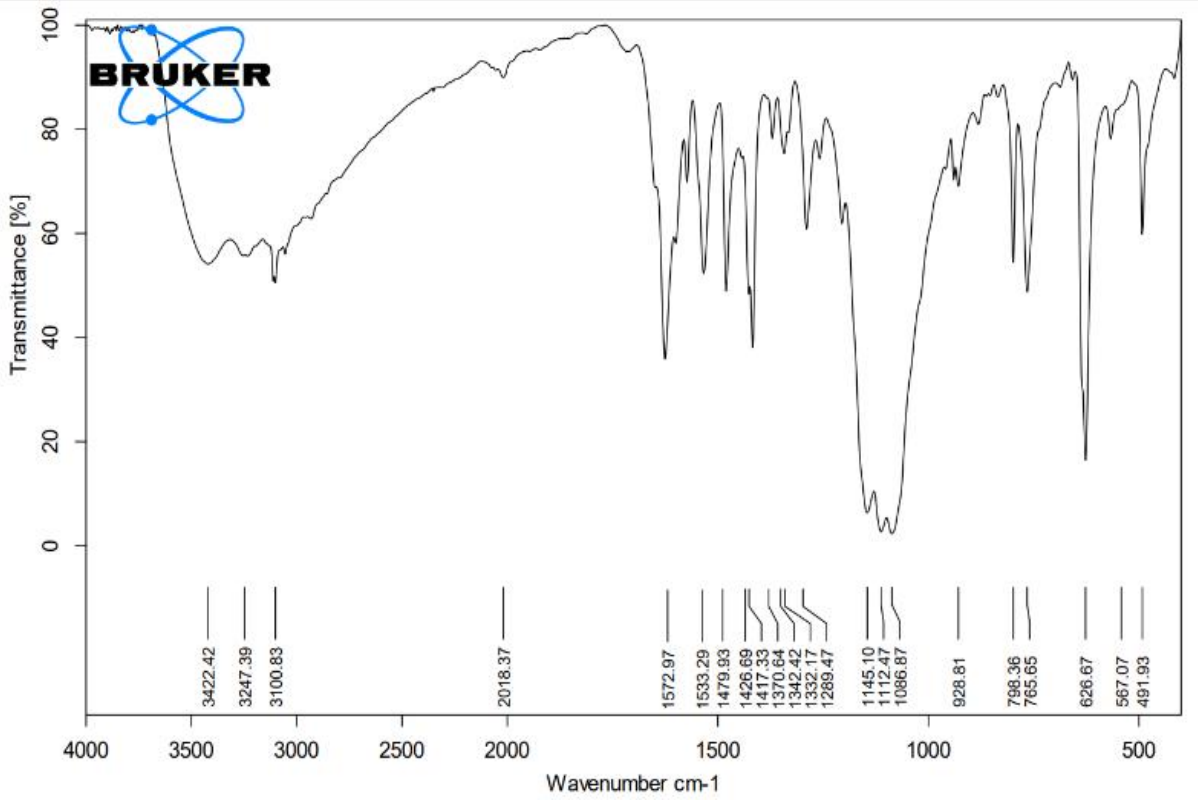

Fig. 5. FTIR spectrum of complex **2**.

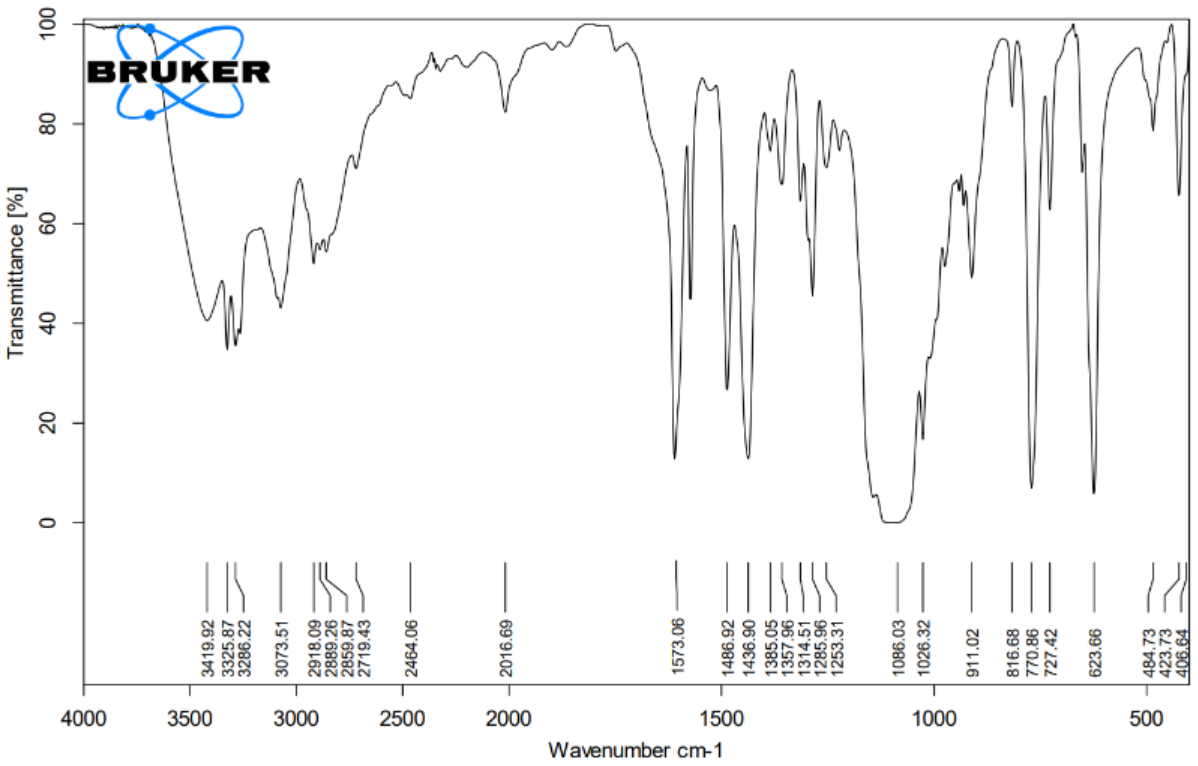

Fig. 6. FTIR spectrum of complex **3**.

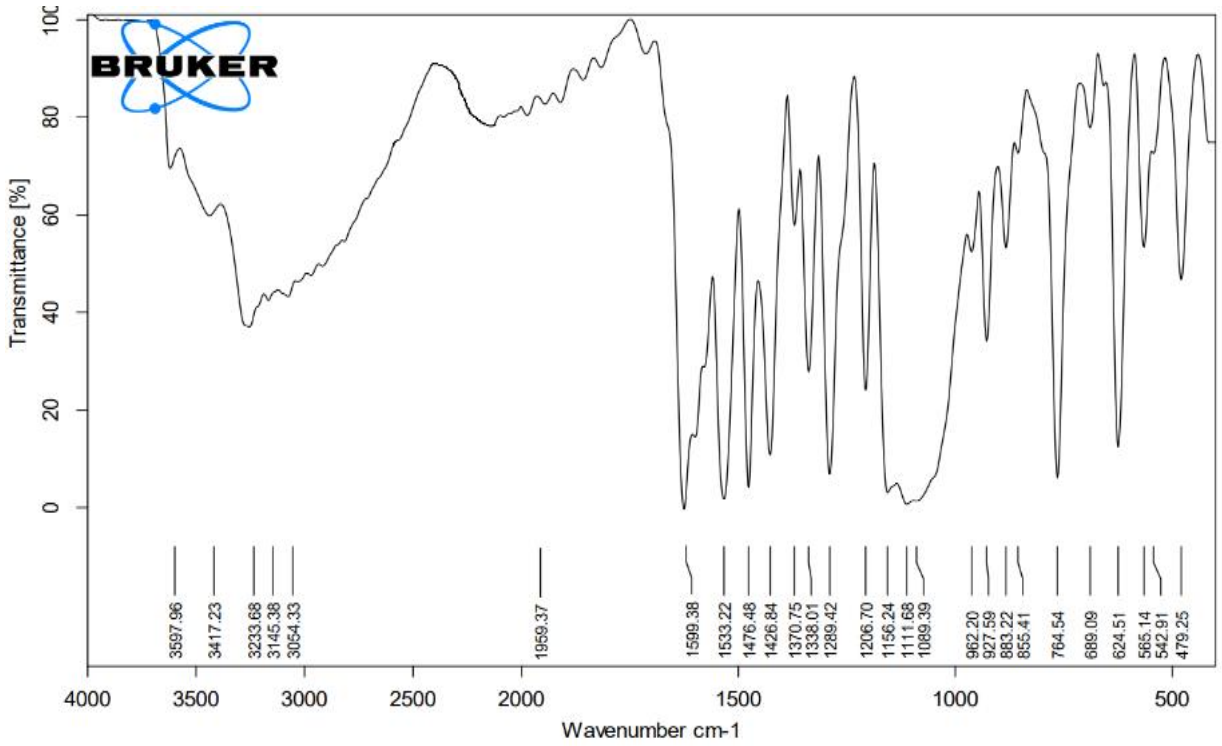

Fig. 7. FTIR spectrum of complex **4**.

Table 1 FTIR peaks of ligand and compounds.

Compound	ν(N–H)	ν(OH)	ν(C=O)	ν(C=N)	ν(N–N)	ν(C–O¯)	ν(M–O)	ν(M–N)
HL	3174	3306	1645	1604	858			
1	-	3418	-	1575	972	1292	526	479
2	-	-	-	1572	928	1289	567	491
3	-	-	-	1573	1026	1285	423	406
4	-	-	-	1599	1089	1289	542	479

3.4 Electronic spectra

The electronic spectra of complexes recorded in DMSO solutions (3.0×10^{-3}M) of all complexes. The absorption band observed in the range 402-405 nm may be attributed to the ligand-to-metal charge transfer (LMCT) transition for each complex (Fig. 8). In the visible region, all complexes display a single absorption band in the range 680-705 nm, agreeing with the expected five-coordinate geometry around copper center [53, 54]. Complex **1** shows the band at 660 and the other shows at 725 nm (Fig. 9) this difference in band position is due to the mono and binuclear nature of complexes. One more absorption band found at ~300 nm in all complexes is consistent with the π-π*/n- π* transition. This highest energy transition is

ligand based [55]. In general five coordinate copper(II) complexes possess square pyramidal or distorted square pyramidal geometry, whereas the corresponding trigonal bipyramidal complexes generally show a maximum at >>800 nm with a higher energy shoulder [56, 57]. In present complexes observed d-d bands remain the range 680-725 nm indicating the distortion in square pyramidal geometry. This absorption maxima present in the visible region arises from a $^2E \rightarrow {}^2T_1$ transition [52, 58].

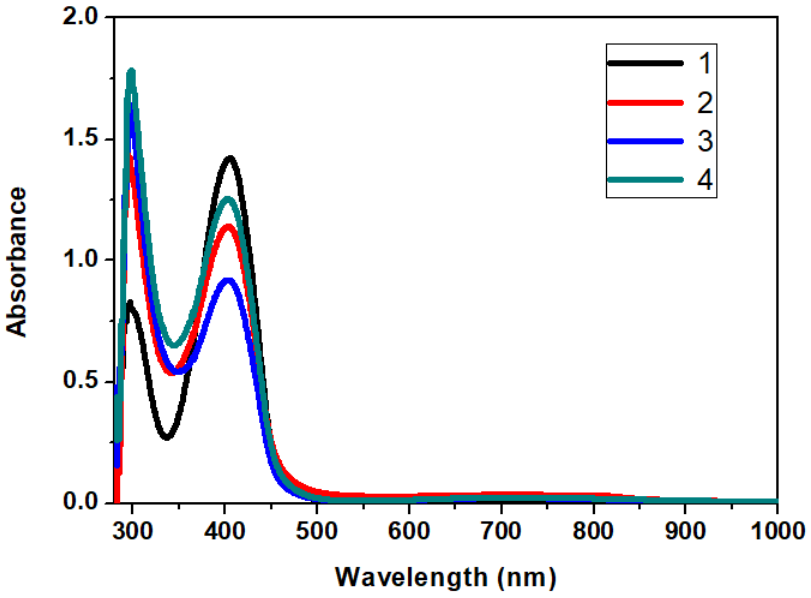

Fig. 8. UV-visible spectra of copper(II) complexes **1-4** in 3.0×10^{-3} M DMSO solution.

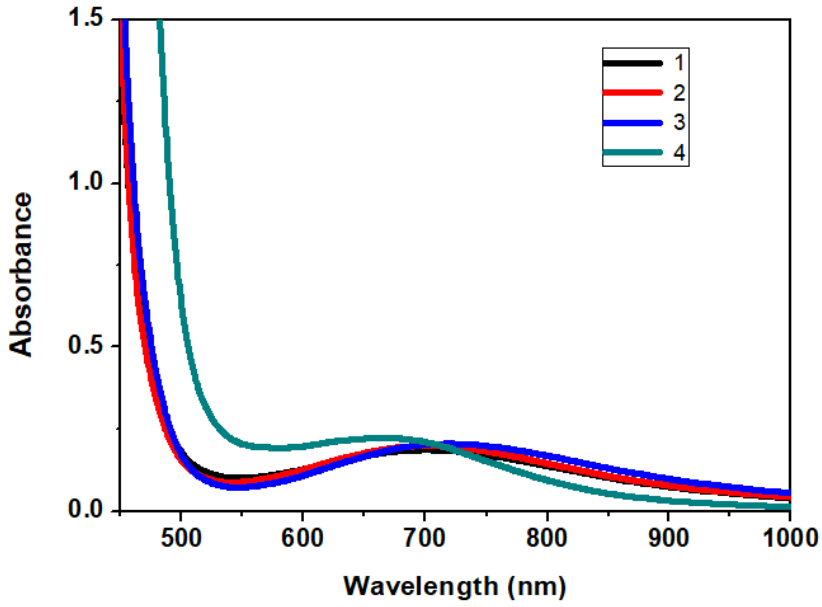

Fig. 9. UV-visible spectra of copper(II) complexes **1-4** in 6.0×10^{-5} M DMSO solution.

3.5 Powder X-ray Diffractions study (PXRD)

The single-crystal structures of the compounds are a well-suited source of information regarding the molecular structure, the difficulty of getting suitable single crystals for a single-crystal X-ray diffraction study. Therefore, in the absence of the single-crystal structure of complexes, PXRD patterns are useful to deduce the crystalline nature of complexes. The PXRD patterns for **1-4** complexes are shown in Fig. 10-13. Each of these (**1-4**) shows the sharp peaks (Fig. 10-13) indicating crystalline nature [60-63]. All the polycrystalline samples gave well-resolved patterns over the range of 5˚< 2Θ< 70˚. The diffraction peaks of the mononuclear complex **1** and binuclear complexes (**2-4**) are different. Some peaks disappear in the **2-4** and some new peaks appear or shifted towards higher 2Θ. This could be attributed to the formation of the binuclear complexes [64]. The major peak regions in **1**, remain 8.05-38.13˚ while complexes **2-4** show the peaks at 2Θ =10.1- 28.29˚.

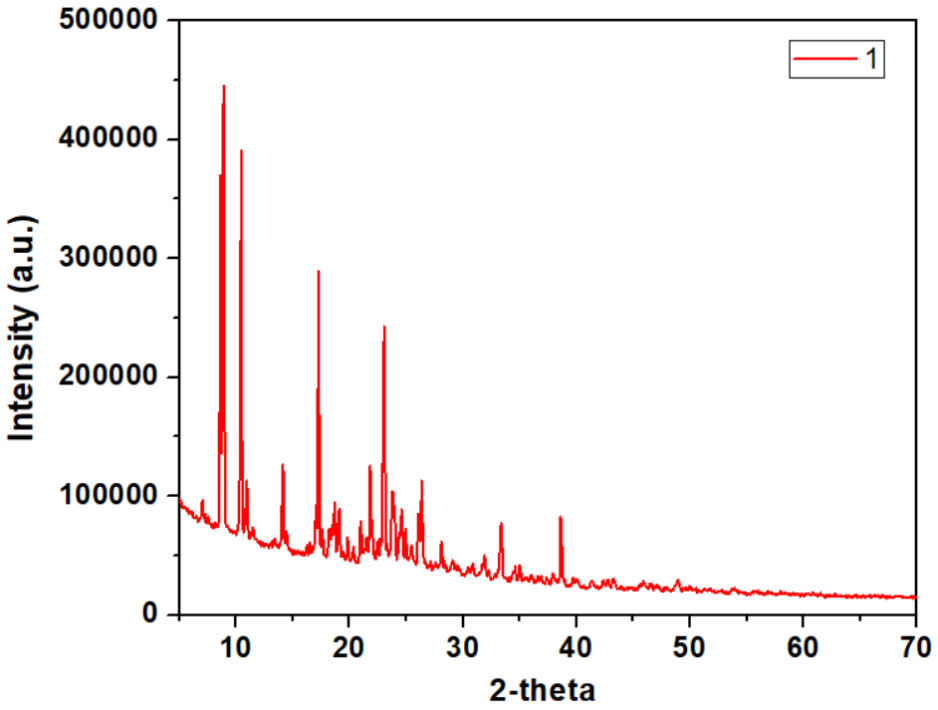

Fig. 10. Powder XRD pattern of complex **1**.

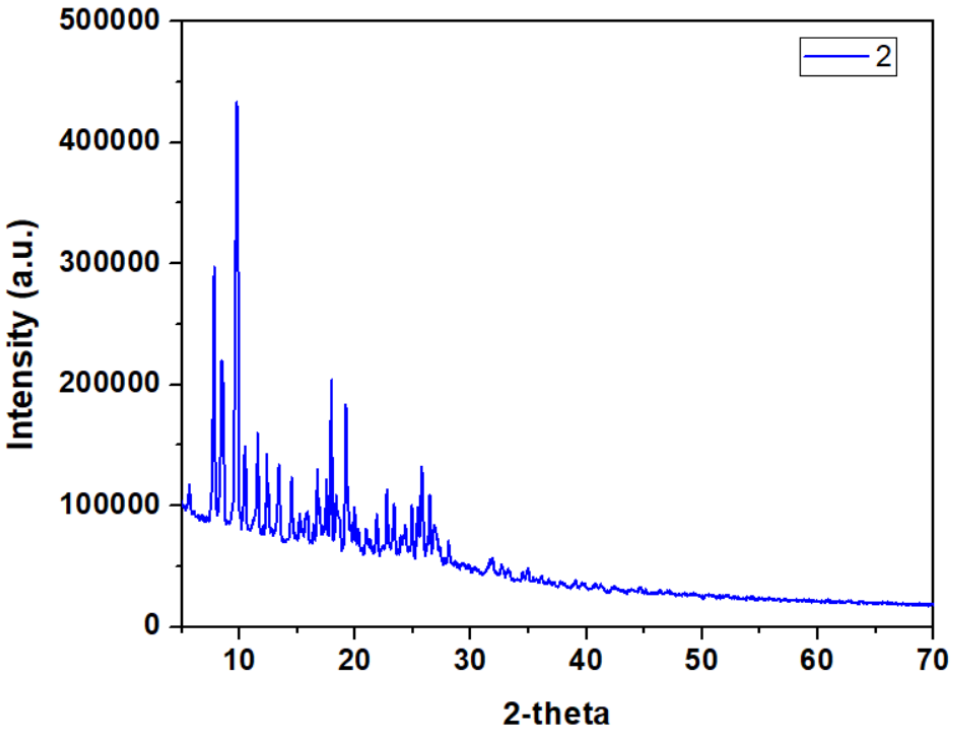

Fig. 11. Powder XRD pattern of complex **2**.

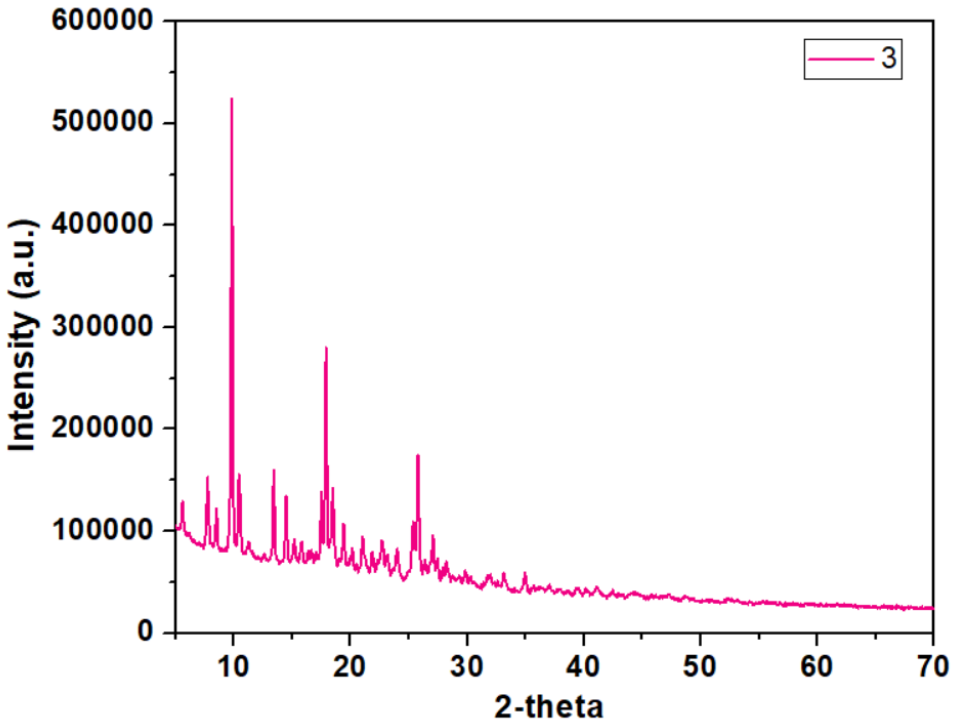

Fig. 12. Powder XRD pattern of complex **3**.

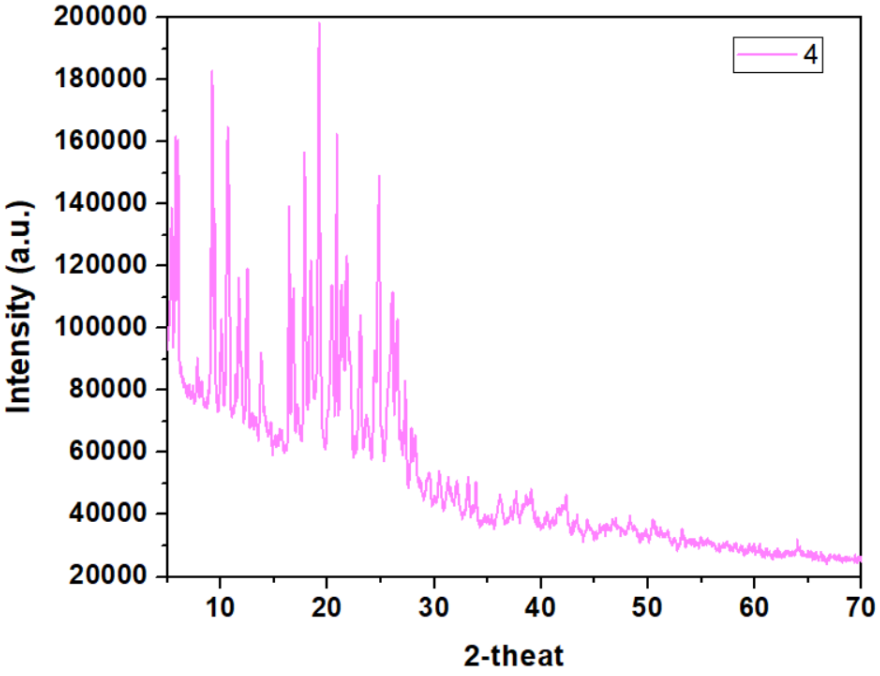

Fig. 13. Powder XRD pattern of complex **4**.

3.6 Epr studies

X-band epr spectra of four new copper(II) complexes were recorded of polycrystalline samples at room temperature (RT) and liquid samples in DMSO (3.0×10^{-3} M) at liquid nitrogen temperature(LNT). Epr spectra are shown in Fig. 14-17 and epr spectral parameters are collected in Table 2. For complex **1**, the spectrum of the polycrystalline sample at RT is broad and almost isotropic. This yields two signals $g_{\parallel}$ = 2.224 and$g_{\perp}$= 2.205. The exchange interaction parameter (G) for this complex is 4.21 indicating no interaction between two dipolar units. Polycrystalline spectra of remaining complexes **2-4** show the polycrystalline spectra with the well-defined half-field signal in the range 1560-1535 G [65]. The presence of such a half-field signal resembling the characteristic signals of exchange-coupled complexes [66, 67]. The G value of these complexes is also less than 4, revealing the interaction in between two dipole units. As these complexes are binuclear, therefore the nature of the interaction is dipole-dipole intramolecular interaction. The bandwidth (ΔB_{pp}) of the perpendicular component is also estimated and given in Table 2. The ΔB_{pp} allows a better evaluation of exchange interaction. The value of ΔB_{pp} for **1** is 140 G and for remaining complexes ~105 G. The reduced ΔB_{pp} of complexes **2-4** also reveals exchange interaction.

Low temperature solution spectra of all complexes were also measured in frozen DMSO solution (Fig. 14-17). Complex **1** shows well-resolved esr spectrum with $g_{\parallel}$ = 2.210

and $g_{\perp}$= 2.068 corresponding to mononuclear complexes with $g_{\parallel} > g_{\perp} >$ 2.0023 [68, 69]. The overall epr spectral features are almost similar for the remaining three complexes (**2-4**). In epr spectra, all three complexes $g_{\parallel}$ region show six $g_{\parallel}$ signals. The presence of six $g_{\parallel}$ signals indicates that the binuclear complex dissociates in solution. Therefore, each spectrum results from the overlap of two species, as is evident in $g_{\parallel}$ region and parameters are collected in Table 2.

Also, the half-field signals in epr were absent or very weak of the present (Fig. 14-17). From these observations, low temperature $g_{\parallel}$ region indicates the contemporary presence of the two mononuclear complexes or equilibrium of mono and binuclear complexes. The $g_{\perp}$regions are merged and only a single maximum absorption is seen in each case with no super hyperfine lines.

Table 2 Spin Hamiltonian parameters for complexes **1-4**.

	RT (Polycrystalline)				LNT (Solution)				
Complex	$g_{\parallel}$	$g_{\perp}$	**G**	ΔB_{pp}(G)	$g_{\parallel}^{1}$	$g_{\parallel}^{2}$	$A_{\parallel}^{1}$(G)	$A_{\parallel}^{2}$(G)	$g_{\perp}$
1	2.224	2.055	4.21	140	2.210	-	160	-	2.068
2	2.210	2.055	3.89	103	2.241	2.203	157	159	2.067
3	2.218	2.068	3.281	105	2.233	2.203	170	170	2.058
4	2.218	2.061	3.61	107	2.207	2.213	160	160	2.065

The binuclear complexes decompose into mononuclear discrete species [Cu(L)X] (X = N_3^-, NCO^- and NCS^-). These mononuclear species yield epr parameters ($g_{\parallel}$ = 2.203-2.241, $g_{\perp}$= 2.058-2.068 and $A_{\parallel}$= 159-170 G), which are similar to that of complex **1**. Such observations in bridged pseudo halides complexes in solution low-temperature epr spectra have already been reported [70-73].

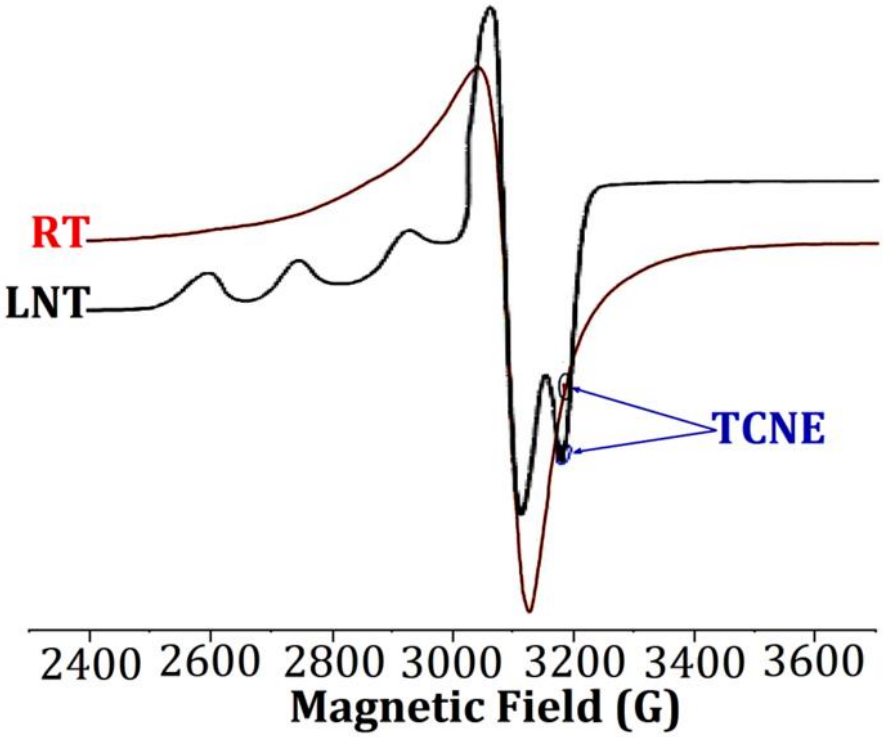

Fig. 14. EPR spectra of complex **1**.

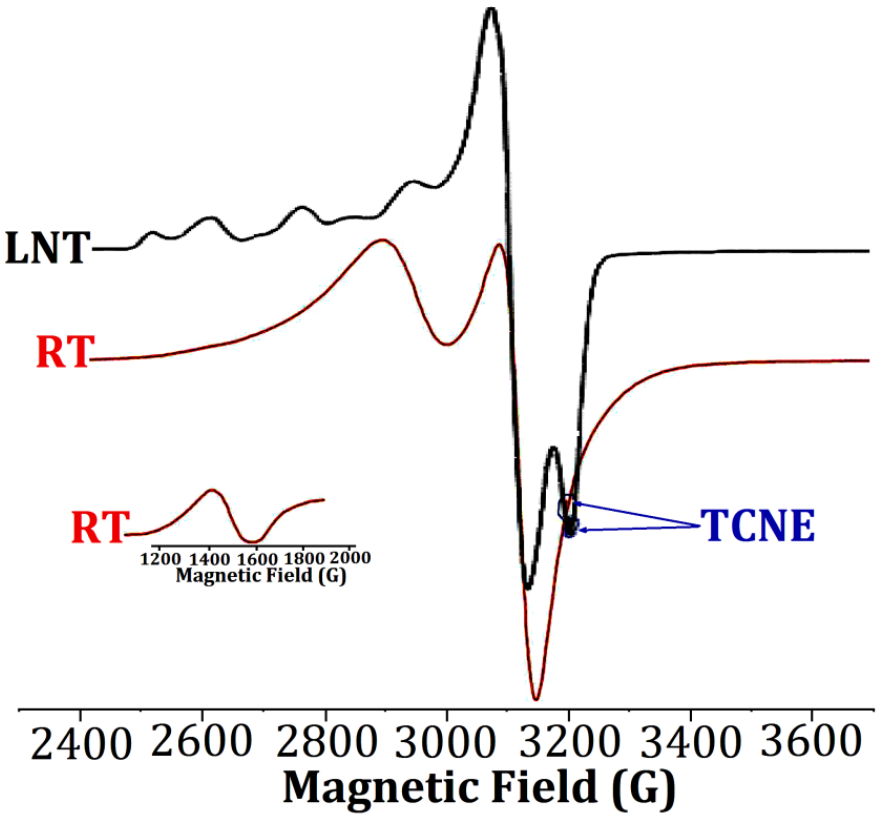

Fig. 15. EPR spectra of complex **2**.

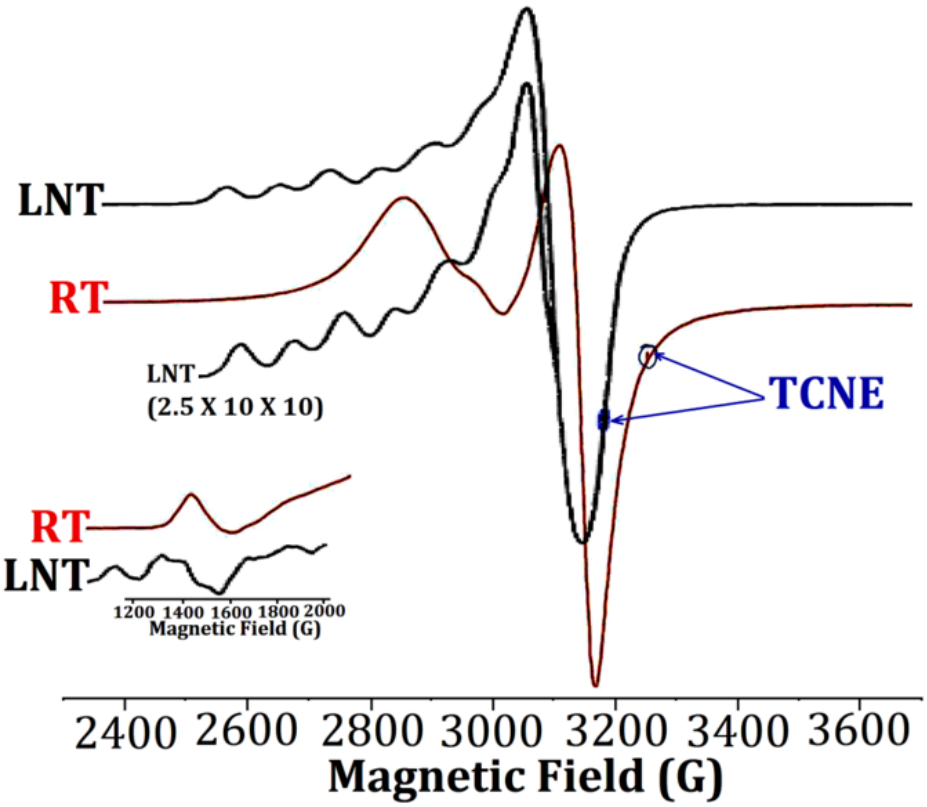

Fig. 16. EPR spectra of complex **3**.

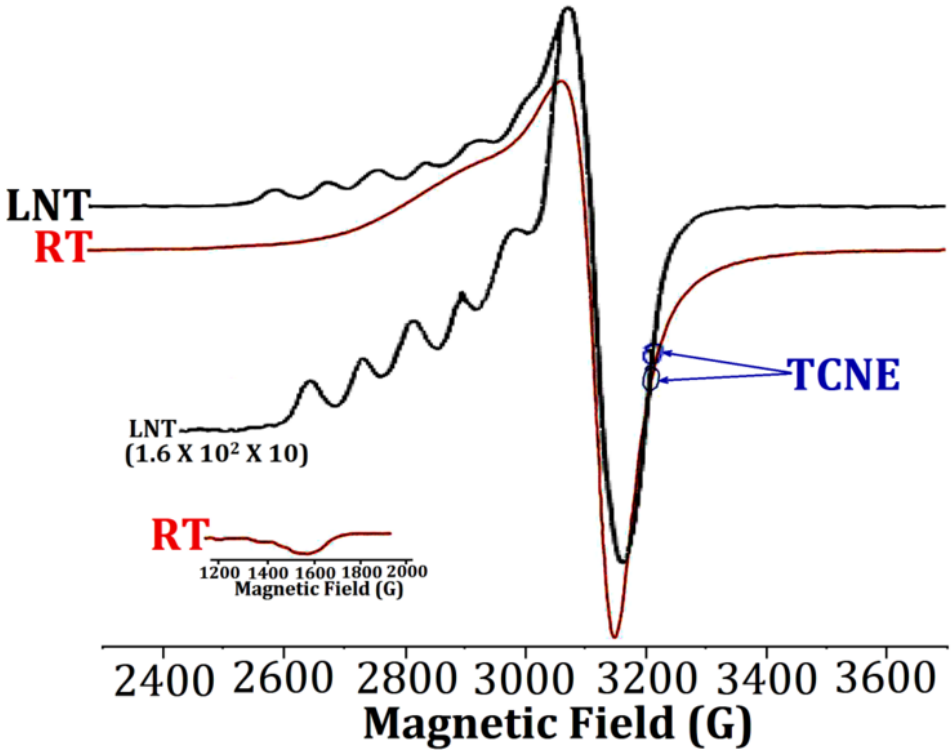

Fig. 17. EPR spectra of complex **4**.

3.7 Electrochemical Activity

Electrochemical properties of complexes **1-4** were studied using cyclic voltammetry (CV) and differential pulse voltammetry (DPV) in DMSO solution containing 0.1M tetra butyl ammonium perchlorate (TBAP) (Fig. 18 and 19). All complexes show two reduction potentials corresponding to two separate couples (1) and (2) in:

$$Cu^{II}\,Cu^{II} \rightleftharpoons Cu^{II}\,Cu^{I} \qquad (1)$$

$$Cu^{II}\,Cu^{I} \rightleftharpoons Cu^{I}\,Cu^{I} \qquad (2)$$

The anodic counterparts of these redox waves are not well defined. The peak potentials beyond these equations (1) and (2) are due to the reduction of ligand moiety of complexes [74-77]. The CV of the five–coordinated complexes reported in the literature showed similar electrochemical properties [78]. Similar electrochemical observations were made from the DPV experiments (Fig. 19). The obtained electrochemical data are summarized in Table 3.

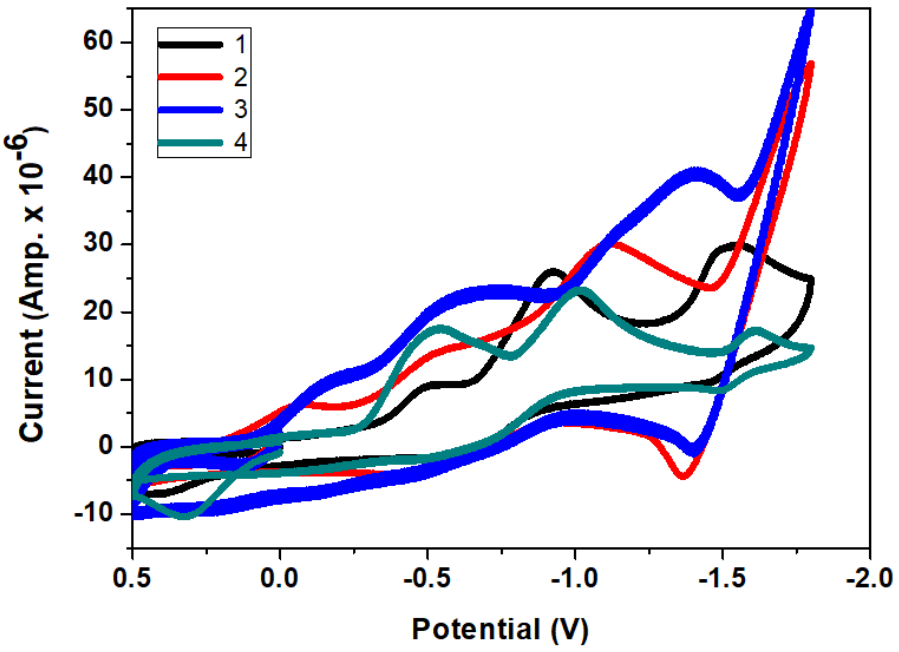

Fig. 18. Cyclic voltammograms for complexes **1-4** in DMSO at an Ag/AgCl electrode with scan rate 100 mVs^{-1} and temperature of 25˚C.

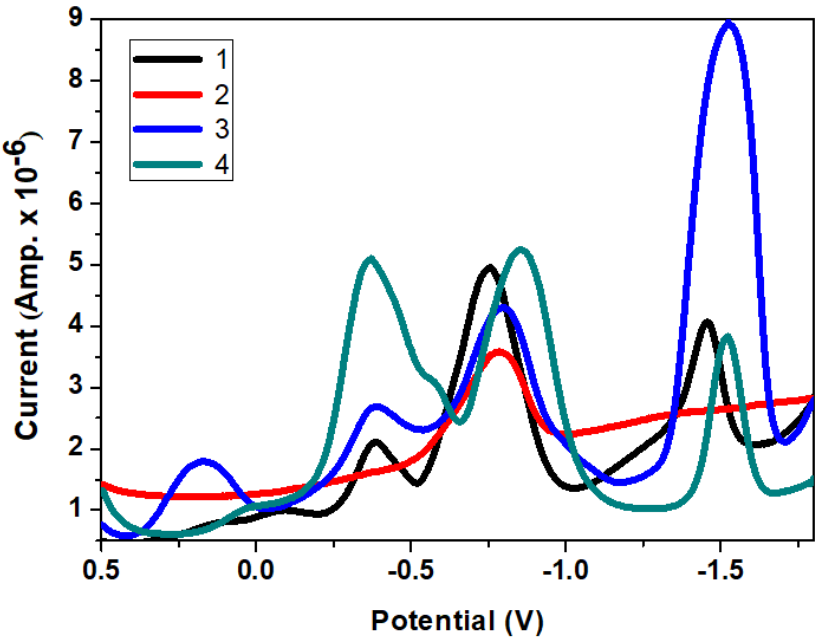

Fig. 19. Differential pulse voltammogram (DPV) of complexes **1-4** at room temperature using a scan rate of 20mVs^{-1} in DMSO at pulse amplitude of 50 mV.

Table 3 Electrochemical data for complexes **1-4** in DMSO (6.0 × 10^{-3} M).

Complex	E_{pc1} (V)	E_{pa1} (V)	E_{pc2} (V)	E_{pa2} (V)	DE_{pc1} (V)	DE_{pc2} (V)	ΔEpc (V)	$E^1_{1/2}$ (V)	$E^2_{1/2}$ (V)	$\Delta E_{1/2}$ (V)	K_{con}
1	-0.343	+0.257	-0.739	-0.435	-0.237	-0.576	0.339	-0.043	-0.587	0.544	1.5×10^9
2	-0.343	+0.308	-0.901	-0.730	-	-0.786					
3	-0.442	-	-1.176	-	-0.238	-0.633	0.395				
4	-0.379	-0.379	-0.831	-0.386	-0.373	-0.576	0.203	-0.287	-0.601	0.314	2.0×10^5

3.8 Mass spectra

The ESI-Mass of all complexes **1-4** were performed in positive mode. The mass spectrum of complexes gives the almost exact mass of the complexes. The molecular ion peaks of complexes are obtained at $[M + 2]^+$ ion mode. The mass spectra of complexes are shown in Fig. 20-23.

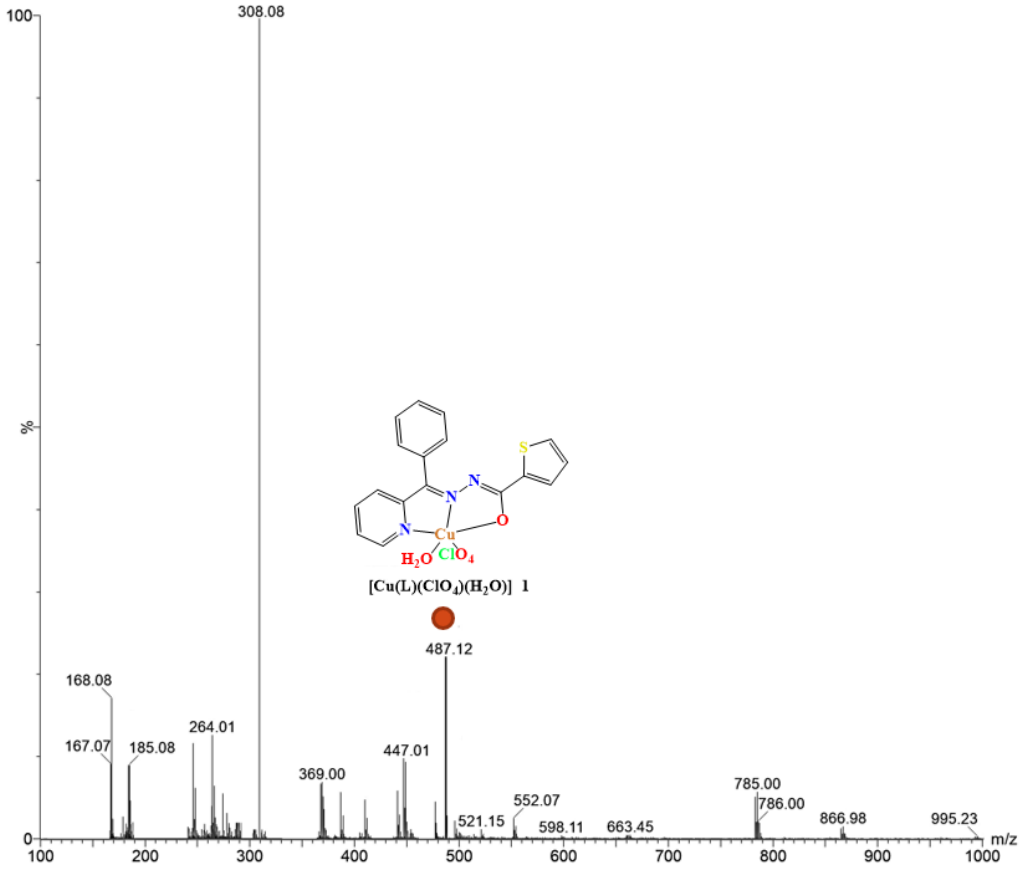

Fig. 20. Mass spectrum of complex **1.**

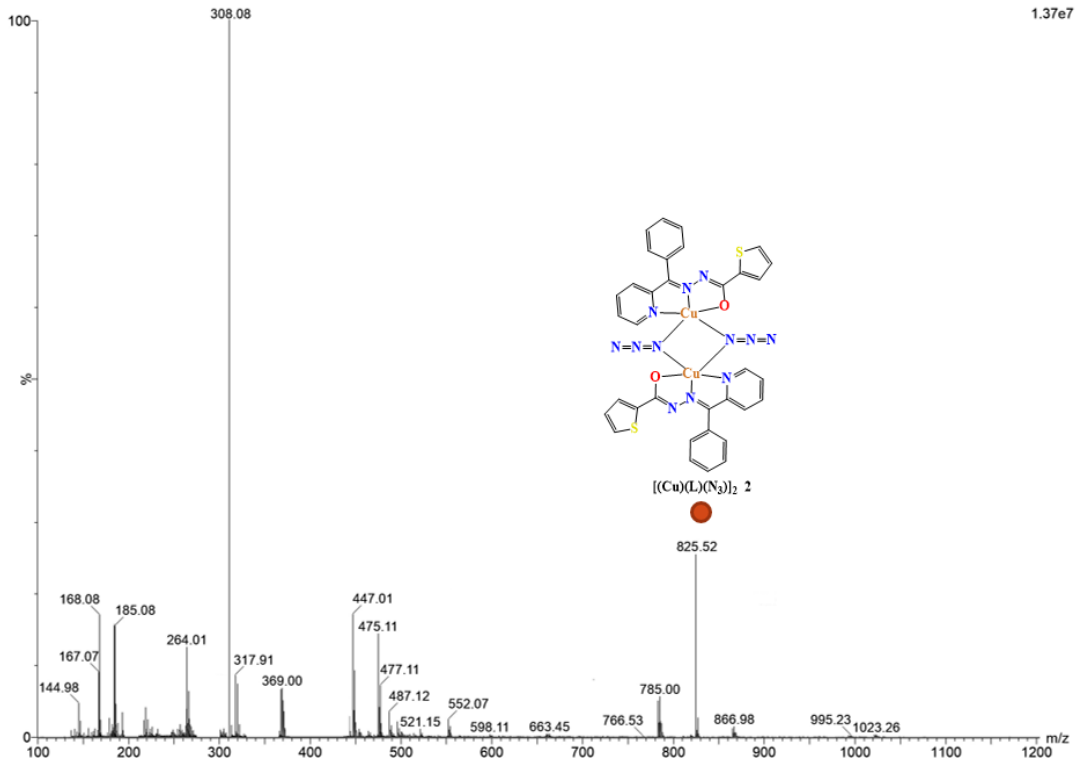

Fig. 21. Mass spectrum of complex **2.**

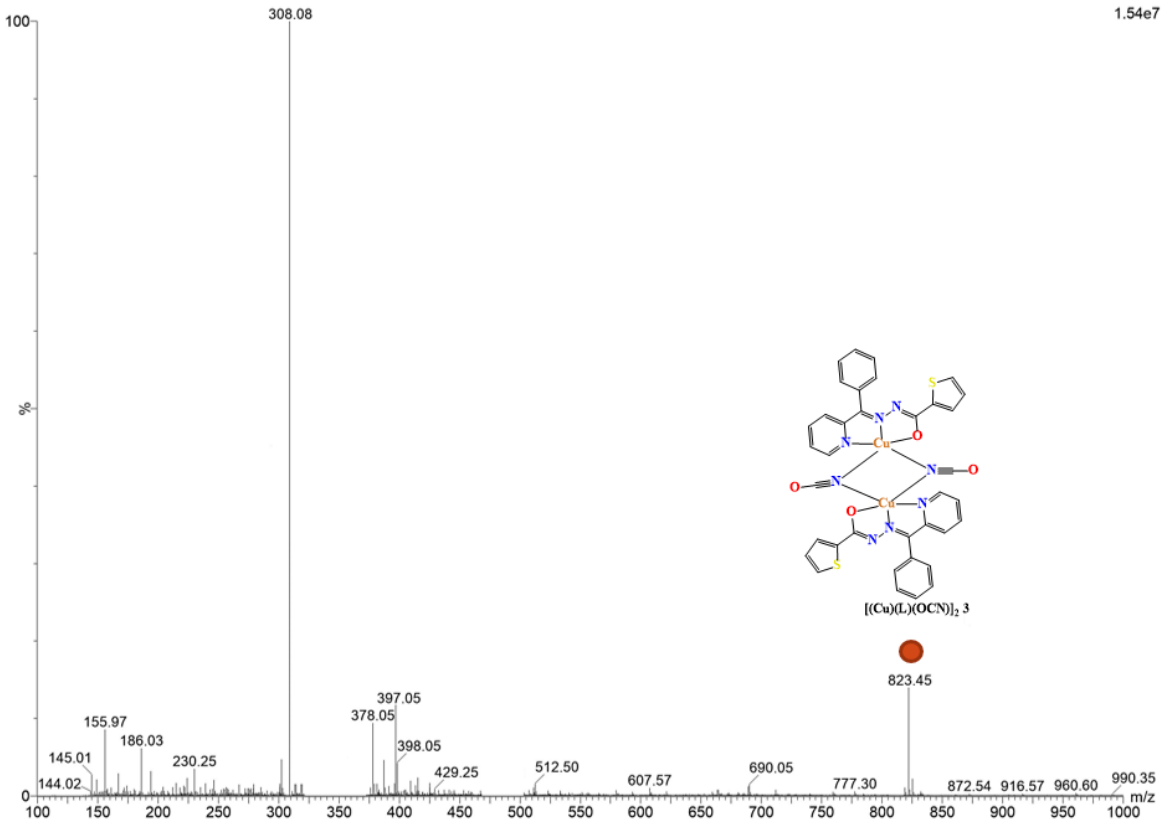

Fig. 22. Mass spectrum of complex **3.**

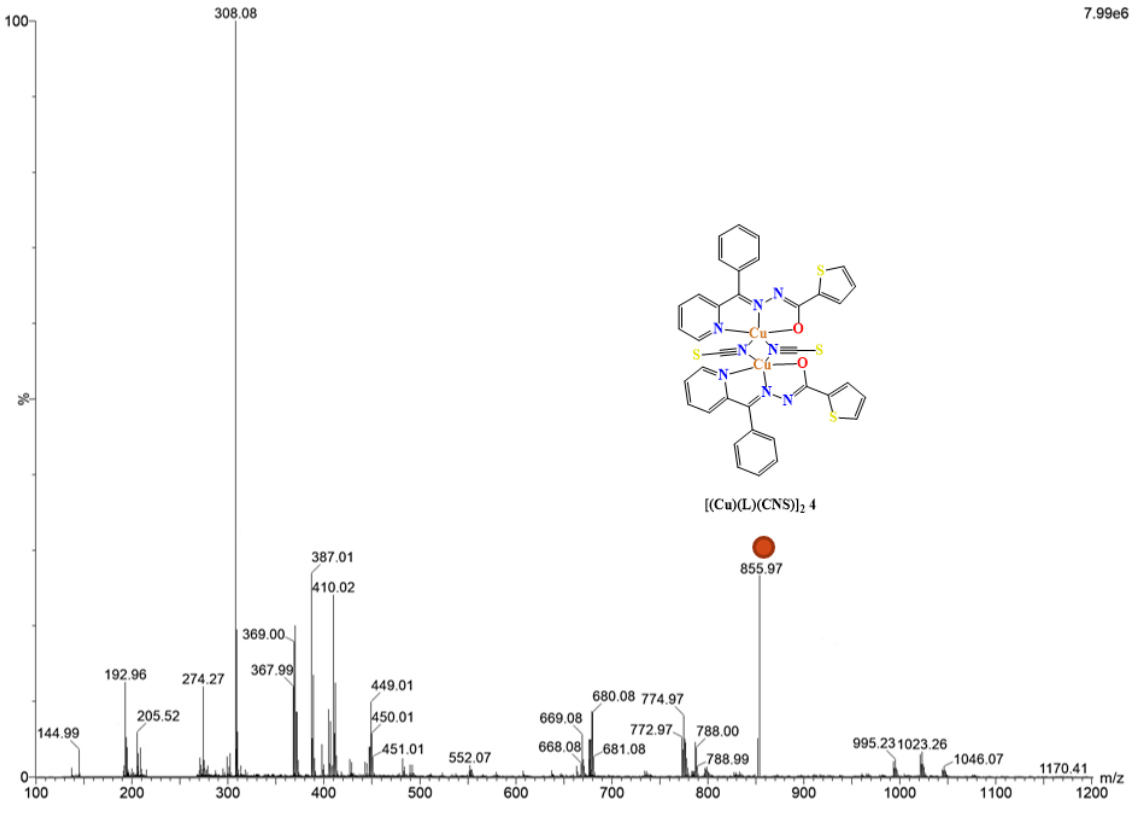

Fig. 23. Mass spectrum of complex **4.**

3.9 DFT Calculations

3.9.1 Optimized structures of complexes

B3LYP [79, 80] estimated interatomic distances and bond angles of **1-4** are given in Table. The optimized molecular structures are shown in Fig. 24-27. All calculations were performed with the GAUSSIAN09 program, [81] with the aid of the Gauss View visualization program. The coordination polyhedron of Cu atom is a distorted square pyramid in **1** with 3N 1O in the equatorial plane and 1O 1N in axial position (Fig. 24). whereas in binuclear complexes **2-4** each Cu atom is surrounded to 2N2O in equatorial and 1 O in axial position. The distorted square pyramidal geometry (τ_5 = β-α / 60° = 0.288) [82] of copper(II) ion in **1** is recognized by four bond lengths Cu(23)-O(21) = 1.839, Cu(23)-O(24) = 1.829, Cu(23)-N(2) = 1.877 and Cu(23)-N(14) = 1.864 Å at equatorial plane and Cu(23)-O(41) = 1.828 Å at axial position. Likewise, the coordination geometry of each copper centres in **2-4** may be described as a distorted square pyramid, as evidenced by the low value of the geometrical structural index (τ_5). The geometrical structural index (τ_5) falls in the range 0.01-0.117. The distortion in polyhedron results from the Jahn-Teller Cu^{2+} ions with d^9 configuration which is typical of a square-based pyramidal geometry. The slightly distorted square geometry of each copper(II) centers in these complexes (**2-4**) is in good agreement with the structural data (bond lengths and bond angles). The Cu-N equatorial distances remain in a range of 1.784-1.899 Å whereas Cu-O equatorial distances fall in a range of 1.862-1.877 Å in complexes (**1-4**). The Cu-Cu distances found to be 2.047, 2.192 and 1.187 Å for **2**, **3** and **4** respectively.

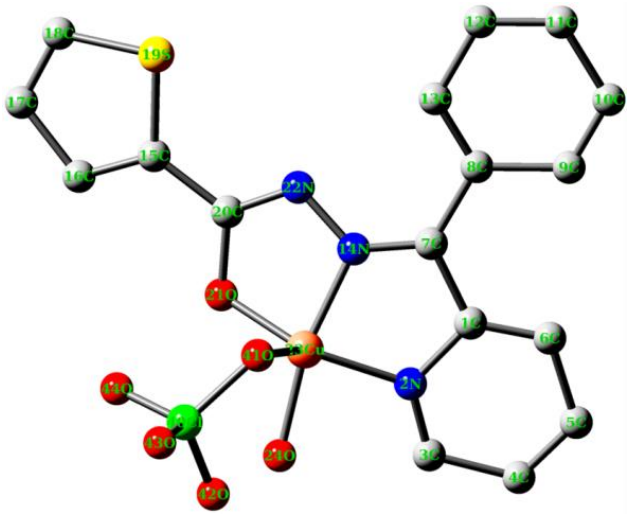

Fig. 24. Optimized structure of complex **1**.

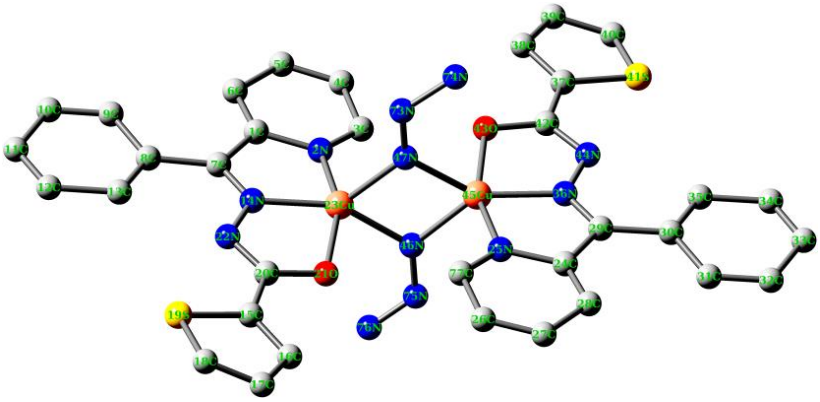

Fig. 25. Optimized structure of complex **2**.

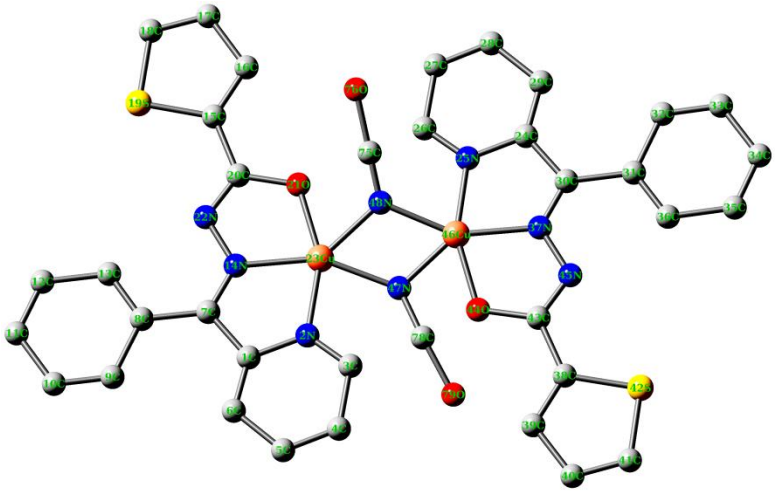

Fig. 26. Optimized structure of complex **3**.

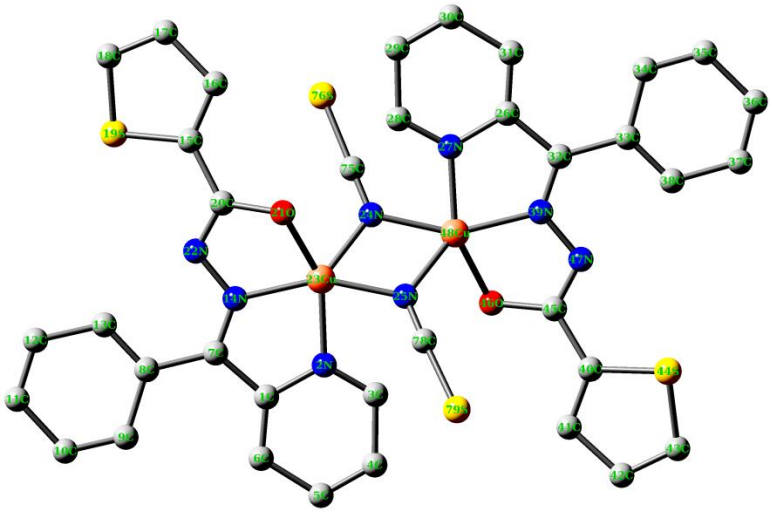

Fig. 27. Optimized structure of complex **4**.

Table 4 Theoretical Bond lengths [Å] and angles [°] for complexes **1-4**.

1			
Bond lengths			
Cu(23)-O(21)	1.839	Cu(23)-N(2)	1.877
Cu(23)-O(24)	1.829	Cu(23)-N(14)	1.864
Cu(23)-O(41)	1.828		
Bond angles			
N(2)-Cu(23)-N(14)	83.056	N(14)-Cu(23)-O(41)	99.619
N(2)-Cu(23)-O(21)	140.827	O(21)-Cu(23)-O(24)	104.205
N(2)-Cu(23)-O(24)	84.050	O(21)-Cu(23)-O(41)	95.204
N(2)-Cu(23)-O(41)	123.559	O(24)-Cu(23)-O(41)	88.476
N(14)-Cu(23)-O(21)	85.232		
2			
Bond lengths			
Cu(23)-N(2)	1.878	Cu(45)-N(25)	1.889
Cu(23)-N(14)	1.914	Cu(45)-N(36)	1.916
Cu(23)-N(46)	1.874	Cu(45)-N(46)	1.870
Cu(23)-N(47)	1.880	Cu(45)-N(47)	1.874
Cu(23)-O(21)	1.877	Cu(45)-O(43)	1.872
Bond angles			
N(2)-Cu(23)-N(14)	82.105	N(25)-Cu(45)-N(36)	81.144
N(2)-Cu(23)-O(21)	154.854	N(25)-Cu(45)-O(43)	156.836
N(2)-Cu(23)-N(46)	105.367	N(25)-Cu(45)-N(46)	93.170
N(2)-Cu(23)-N(47)	94.672	N(25)-Cu(45)-N(47)	103.671
N(14)-Cu(23)-O(21)	78.290	N(36)-Cu(45)-O(43)	79.002
N(14)-Cu(23)-N(46)	153.319	N(36)-Cu(45)-N(46)	136.155
N(14)-Cu(23)-N(47)	132.073	N(36)-Cu(45)-N(47)	149.790
O(21)-Cu(23)-N(46)	86.120	O(43)-Cu(45)-N(46)	109.425
O(21)-Cu(23)-N(47)	110.142	O(43)-Cu(45)-N(47)	87.938
N(46)-Cu(23)-N(47)	73.653	N(46)-Cu(45)-N(47)	73.885
3			
Bond lengths			
Cu(23)-N(2)	1.886	Cu(46)-N(25)	1.873
Cu(23)-N(14)	1.951	Cu(46)-N(37)	1.921
Cu(23)-N(47)	1.942	Cu(46)-N(47)	1.784
Cu(23)-N(48)	1.877	Cu(46)-N(48)	1.886
Cu(23)-O(21)	1.868	Cu(46)-O(44)	1.873
Bond angles			
N(2)-Cu(23)-N(14)	79.030	N(25)-Cu(46)-N(37)	79.857
N(2)-Cu(23)-O(21)	155.402	N(25)-Cu(46)-O(44)	156.532
N(2)-Cu(23)-N(47)	76.572	N(25)-Cu(46)-N(47)	134.993

N(2)-Cu(23)-N(48)	134.653	N(25)-Cu(46)-N(48)	74.255
N(14)-Cu(23)-O(21)	76.490	N(37)-Cu(46)-O(44)	77.222
N(14)-Cu(23)-N(47)	154.790	N(37)-Cu(46)-N(47)	141.740
N(14)-Cu(23)-N(48)	142.213	N(37)-Cu(46)-N(48)	152.616
O(21)-Cu(23)-N(47)	128.022	O(44)-Cu(46)-N(47)	65.995
O(21)-Cu(23)-N(48)	68.159	O(44)-Cu(46)-N(48)	129.159
N(47)-Cu(23)-N(48)	62.808	N(47)-Cu(46)-N(48)	65.632
4			
Bond lengths			
Cu(23)-N(2)	1.906	Cu(48)-N(24)	1.876
Cu(23)-N(14)	1.932	Cu(48)-N(25)	1.885
Cu(23)-N(24)	1.867	Cu(48)-N(27)	1.899
Cu(23)-N(25)	1.886	Cu(48)-N(39)	1.927
Cu(23)-O(21)	1.862	Cu(48)-O(46)	1.872
Bond angles			
N(2)-Cu(23)-N(14)	78.719	N(24)-Cu(48)-N(25)	67.230
N(2)-Cu(23)-O(21)	149.412	N(24)-Cu(48)-N(27)	75.097
N(2)-Cu(23)-N(24)	131.699	N(24)-Cu(48)-N(39)	153.720
N(2)-Cu(23)-N(25)	78.095	N(24)-Cu(48)-O(46)	124.697
N(14)-Cu(23)-O(21)	76.490	N(25)-Cu(48)-N(27)	131.324
N(14)-Cu(23)-N(24)	135.305	N(25)-Cu(48)-N(39)	136.903
N(14)-Cu(23)-N(25)	155.816	N(25)-Cu(48)-O(46)	77.904
O(21)-Cu(23)-N(24)	78.884	N(27)-Cu(48)-N(39)	79.107
O(21)-Cu(23)-N(25)	122.696	N(27)-Cu(48)-O(46)	150.736
N(24)-Cu(23)-N(25)	67.396	N(39)-Cu(48)-O(46)	77.688

3.9.2 Crucial Electronic parameters

Electronic properties yield deeper insights into the nature of molecules. Table 5 shows the electronic properties, computed at the level of B3LYP/LANL2DZ of the optimized copper(II) mono and binuclear complexes. Among these crucial electronic parameters, the energy of HOMO (E_{HOMO}) and LUMO (E_{LUMO}), energy gap (ΔE), ionization potential (I), electron affinity (IA), electronegativity (χ), chemical potential (μ), global hardness (η), global softness (S), electrophilicity index (ω), electron-donating capacity (ω^-) and electron-accepting capacity (ω^+). These electronic parameters are evaluated from the energies of HOMO and LUMO frontier orbitals of **1-4** complexes (Fig. 28-31). Frontier molecular orbitals are significant in ascertaining the optical properties as well as chemical reactivity of an entity. The energy gap (ΔE) is associated with stability and chemical hardness. Higher

chemical hardness reveals the lower reactivity of the entity [83, 84]. The lower energy gap (ΔE) shows lower kinetic stability or larger chemical reactivity and larger polarizability of the molecules. Among these complexes, **4** shows minimum (ΔE) in comparison to other complexes (**1-3**) (Table 5). As a consequence, the removal of electrons from the ground state HOMO to the excited state LUMO needs less energy. The ionization potential (I) and electron affinity (IA) reveals how easily electrons can be removed from ground state HOMO or can be added to the excited state LUMO frontier orbital resulting in either a cationic or anionic radical. Complex **3** shows the highest I (7.0996 eV) and the least EA is shown by **4**. As per the given permissible limits, all four complexes are air-stable. Likewise, ionization potential is also decided by the value of I. More the value of I more is the hard molecule and less soft. This concept is evidenced in Table. 5 Electronegativity (χ) and electrophilicity index (ω) give an idea of electron attracting power of the molecule. Complex **1** showed high I and ω. Values of electron-donating and electron-accepting capacity of **4** are minimum.

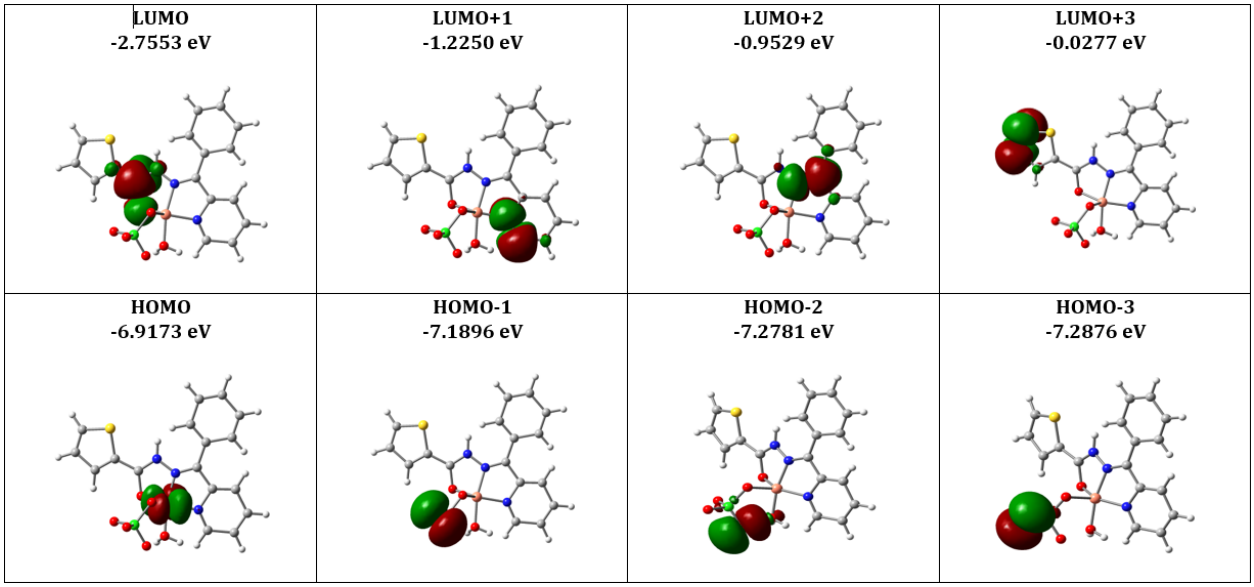

Fig. 28. HOMO-LUMO analysis of complex **1**.

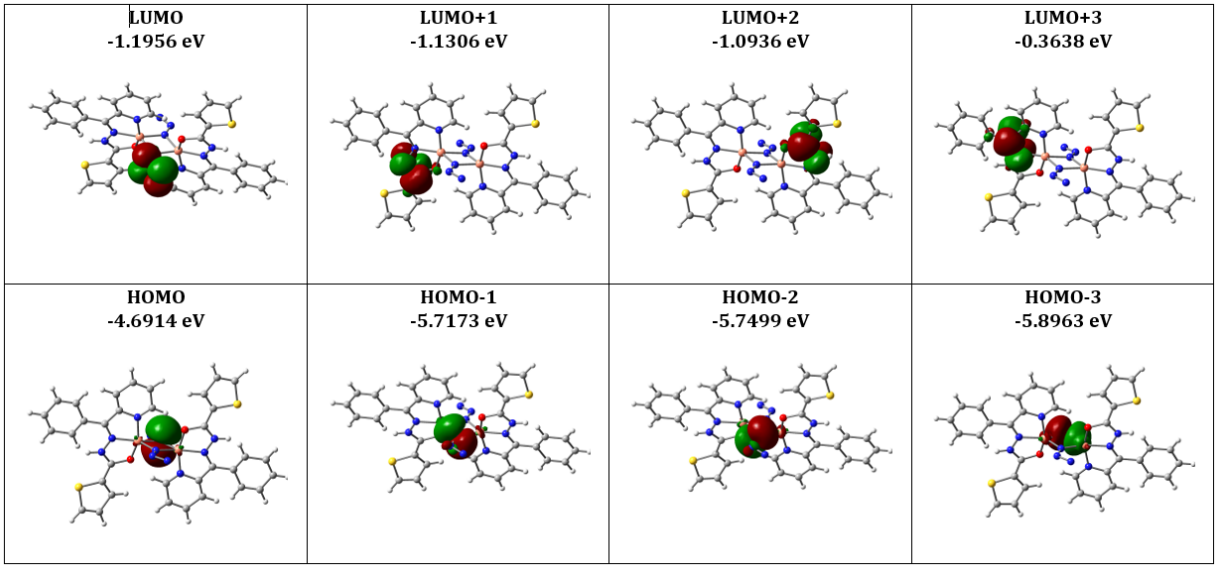

Fig. 29. HOMO-LUMO analysis of complex **2**.

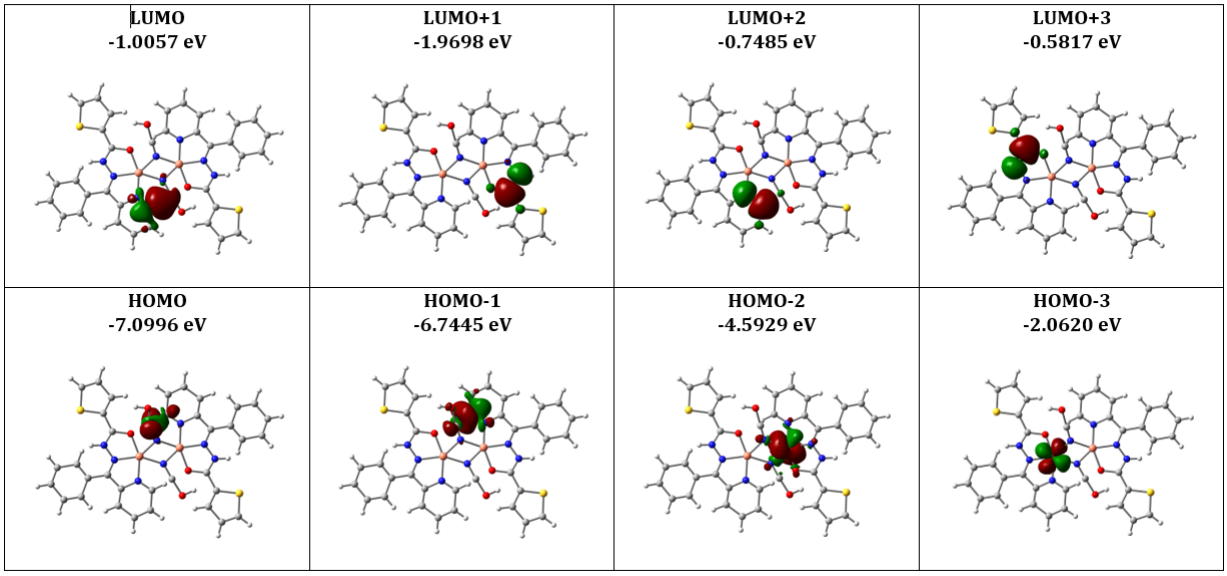

Fig. 30. HOMO-LUMO analysis of complex **3**.

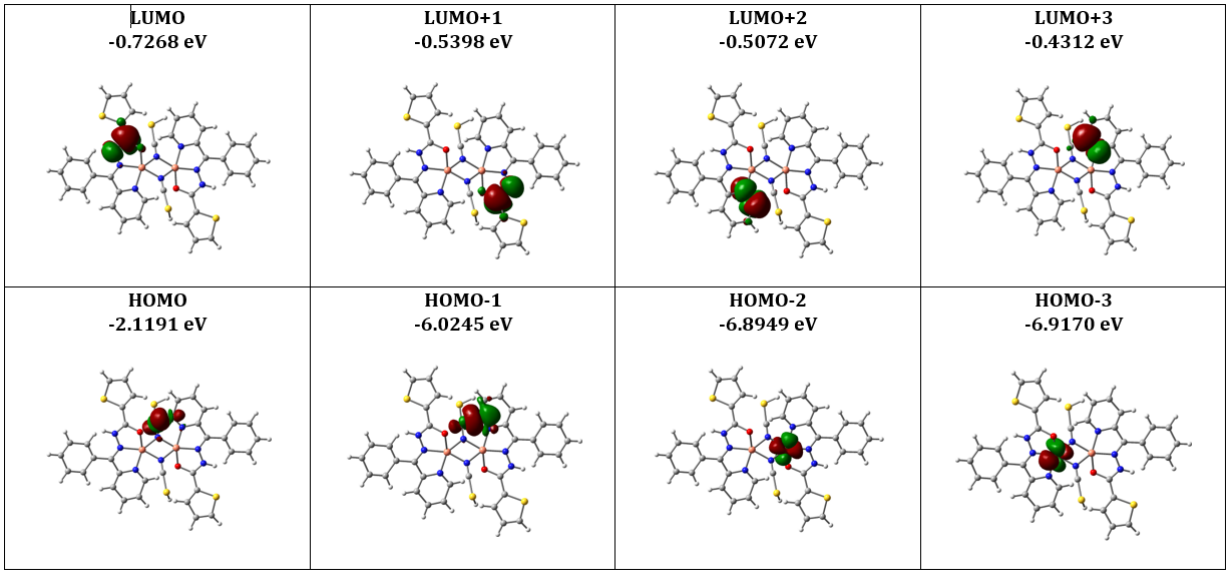

Fig. 31. HOMO-LUMO analysis of complex **4**.

Table 5 The crucial electronic parameters for complexes **1-4**.

Molecular Descriptor	Mathematical descriptor	1	2	3	4
E_{HOMO} (eV)	Energy of HOMO	-6.9173	-4.6914	-7.0996	-2.1191
E_{LUMO} (eV)	Energy of LUMO	-2.7553	-1.1956	-1.0057	-0.7268
Energy gap (eV)	$\Delta E = E_{HOMO} - E_{LUMO}$	4.162	3.4958	6.0939	1.3923
Ionization potential (eV)	$I = - E_{HOMO}$	6.9173	4.6914	7.0996	2.1191
Electron affinity (eV)	$EA = - E_{LUMO}$	2.7553	1.1956	1.0057	0.7268
Electronegativity (eV)	$\chi = (I+EA)/2$	4.8363	2.9435	4.0526	1.4229
Chemical potential (eV)	$\mu = - \chi$	-4.8363	-2.9435	-4.0526	-1.4229
Global hardness (eV)	$\eta = (I-EA)/2$	2.081	1.7479	3.0469	0.6961
Softness $(eV)^{-1}$	$S = 1/2\eta$	0.2403	0.2861	0.1641	0.7182
Electrophilicity index	$\omega = \mu^2/2\eta$	5.6198	2.4785	2.6951	1.4542
Electron donating capacity	$\omega- = (3E_{HOMO} + E_{LUMO})^2 / 16(E_{HOMO} - E_{LUMO})$	8.2981	4.1687	5.1023	2.252
Electro accepting capacity	$\omega+ = (E_{HOMO} + 3E_{LUMO})^2 / 16(E_{HOMO} - E_{LUMO})$	3.4618	1.2252	1.0497	0.829

3.9.3 Spin density

The surfaces of the spin density for mononuclear **1** and binuclear complexes (**2-4**) were estimated (Table 6). It is observed that most of the spin density is located on the copper centers. The spin populations on copper atoms are 0.677e **1**, 0.700e & 0.693e **2**, 0.734e & 0.747e **3** and 0.715e & 0.727e **4** in mono- and binuclear complexes respectively. On perusal of these spin density data, it is obvious that the spin population in binuclear complexes copper centers is larger than that in the mononuclear copper center. A similar trend was observed from the Mulliken population analysis (Table 6).

Table 6 Spin density of copper center for complexes **1-4**.

Complex	Spin density	Mulliken Population
1	0.677e	0.505e
2	0.700e, 0.693e	0.553e, 0.581e
3	0.734e, 0.747e	0.711e, 0.703e
4	0.715e, 0.727e	0.616e, 0.615e

3.10 Catalytic activity

All the synthesized mono and binuclear complexes exhibit catalytic activity towards the dismutation of superoxide anions at physiological pH. The superoxide dismutase (SOD) catalytic activities were carried out in a phosphate buffer of pH 7.8 by the NBT assay method [70, 85-88]. The SOD graph of complexes is shown in Fig. 32. The concentrations of catalysts required to yield 50% inhibition of the reduction nitro blue tetrazolium chloride (NBT) defined as IC_{50} were calculated (Table 7). The catalytic parameters compared to the similar systems of biologically important ligands as well as values of best SOD mimics reported in the literature are also given for comparison point of view. The relative high SOD activity of complexes **1-4** show good SOD activity may be attributed to the flexible nature of hydrazone ligand, which can facilitate the reduction of copper(II) to copper(I) associated with variation of coordination geometry and the accommodation of copper(I) [89].

The catalytic rate constant (k_{McCF}) was also calculated for all complexes using the formula $k_{McCF} = k_{NBT} \times [NBT]/IC_{50}$, where $k_{NBT} = 5.94 \times 10^{-4}$ (mol L^{-1}) S^{-1} is second-order rate constant for NBT [90]. The k_{McCF} values of **1-4** are 16.63, 13.86, 9.78 and 11.09 respectively. On perusal of k_{McCF} values, it is indicated that **1-4** can be used as an antioxidant superoxide

scavenger. Based on SOD data, it is obvious that **1-4** is more efficient antioxidant scavengers than the standard antioxidant (vitamin c) [90, 91]. The SOD activities of complexes **1-4** are similar to that of square pyramidal mononuclear complex **1** (Table 7) [92]. The binuclear complexes dissociate in the solution and therefore yield similar SOD activity. The catalytic mechanism is shown in scheme 5. In step (i) the inner sphere electron transfer takes place in between copper(II) centre of complexes and the coordinate superoxide anion (O_2). In step (ii) the subsequent cleavage of the copper-X (X = ClO_4^-, N_3^-, NCO^-& NCS^-) bond in assisted by protonation of the solvent and the oxygen molecule is released. In step (iii) oxidation of copper(I) to copper(II) by the second molecule $O_2^{\cdot -}$ reforms the bond with X along with transfer of proton to the peroxide ion in step ii.

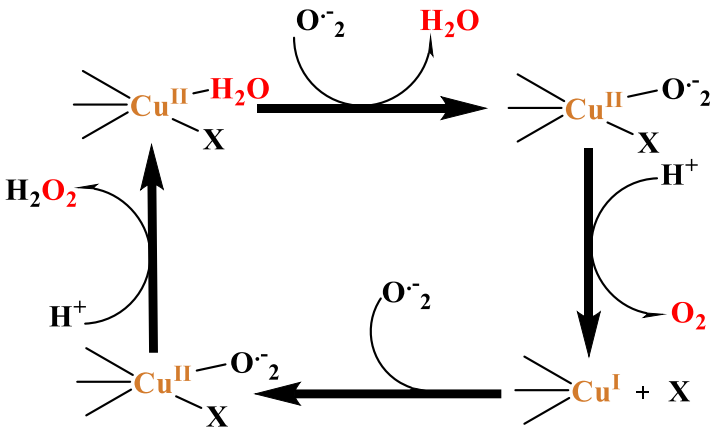

Scheme 5 The proposed catalytic mechanism.

Table 7 The SOD activity, IC_{50} values and k_{McCF} values for complexes **1-4**.

Complex	IC_{50}(µmol)	SOD activity (µmol^{-1})	k_{McCF} (mol L^{-1}) S^{-1}	Ref.
1	20	50.00	16.63	This work
2	24	41.666	13.86	This work
3	34	29.411	9.78	This work
4	30	33.333	11.09	This work
[Cu_2(µ-SCN)$_2$(L)$_2$]	24	41.66	13.86	78
[(L^1)Cu(µ-CH_3COO)$_2$Cu(L^1)]	35	28.57	9.50	70
[(L^1)Cu(µ-NO_3)2Cu(L^1)]	26	38.46	12.79	91
Vc	852	1.17	0.39	92

Where L = N'-[(Z)-phenyl(pyridin-2-l)methylidene]acetohydrazide, L^1 = N'-[(E)-phenyl(pyridin-2-yl)methylidene]benzohydrazide.

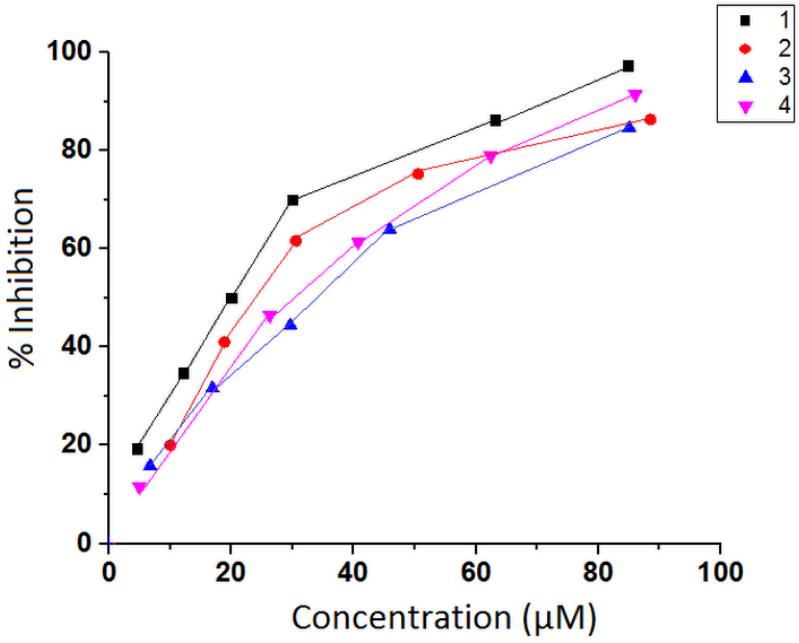

Fig. 32. SOD graph of complexes **1-4**.

4 Conclusions

In this chapter, we have reported the synthesis of a new Schiff base ligand, N'-(phenyl-pyridine-2-yl-methylene)-thiophene-2-carboxylic acid hydrazide (HL) and its metal complexes. The ligand and its complexes are well characterized by analytical and spectral method. The molar conductance values of the complexes **1-4** in DMSO at room temperature are observed in the range 8.34–18.24 (Ω^{-1} cm^2 mol^{-1}) indicating that they are non-electrolytic nature. The distorted square pyramidal geometry (τ_5 = β-α/60° = 0.288) of copper(II) ion in complex **1** the coordination geometry of each copper centres in **2-4** may be described as a distorted square pyramid, as evidenced by the low value of the geometrical structural index (τ_5). The geometrical structural index (τ_5) falls in the range 0.01-0.117 in complexes **2-4**. The distortion in polyhedron results from the Jahn-Teller Cu^{2+} ions with d^9 configuration which is typical of a square-based pyramidal geometry. The G value of these complexes is also of less than 4, revealing the interaction in between two dipole units. As these complexes are binuclear in nature, therefore the nature of interaction is dipole-dipole intramolecular interaction. The catalytic rate constant (k_{McCF}) was also calculated for all complexes. The k_{McCF} value of **1-4** are 16.63, 13.86, 9.78 and 11.09, respectively. On perusal of k_{McCF} values, it is clearly indicated that **1-4** can be used as an antioxidant superoxide scavenger.

References

1 G. Tamasi, L. Chiasserini, L. Savini, A. Sega, R. Cini, J. Inorg. Biochem. 99 (2005) 1347-1359.

2 S. Banarjee, A. Ray, S. Sen, S. Mitra, D.L. Hughes, R.J. Butcher, S.R. Batten, D.R. Turner, Inorg. Chim. Acta 361 (2008) 2962-2700.

3 S. Banerjee, S. Sen, S. Basak, S. Mitra, D. L. Hughes, C. Desplanches, Inorg. Chim. Acta 361 (2008) 2707-2714.

4 P.E. Aranha, M.P.D. Santos, S. Romera, E.R. Dockal, Polyhedron 26 (2007) 1373-1382.

5 P.V. Bernhardt, P. Chin, P.C. Sharpe, J.Y.C. Wang, D.R. Richardson, J. Biol. Inorg. Chem. 10 (2005) 761-777.

6 B. Bottari, R. Maccari, F. Monforte, R. Ottana, E. Rotondo, M.G. Vigorita, Bioorg. Med. Chem. Lett. 10 (2000) 657-660.

7 J. Easmon, G. Puerstinger, T. Roth, H.H. Fiebig, M. Jenny, W. Jaeger, G. Heinisch, J. Hofmann, Int. J. Cancer 94 (2001) 89-96.

8 D.S. Kalinowski, P.C. Sharpe, P.V. Bernhardt, D.R. Richardson, J. Med. Chem. 51 (2008) 331-344.

9 B.K. Kaymakcioglu, S. Rollas, Farmaco. 57 (2002) 595-599.

10 S.K. Sridhar, M. Saravanan, A. Ramesh, Eur. J. Med. Chem. 36 (2001) 615-625.

11 O. Pourlimardan, A.C. Chamayou, C. Janiak, H.H. Monfared, Inorg. Chim. Acta 360 (2007) 1599-1608.

12 L.H.S.A. Terra, M. Encarnacion, V. Suarez-Iha, Spectrosc. Lett. 30 (1997) 625-639.

13 A. Roy, S. Banerjee, R.J. Butcher, C. Desplanches, S. Mitra, Polyhedron 27 (2008) 2409-2415.

14 U. Roy, B. Chand, G. Mostafa, J. Cheng, T.H. Lu, C. Sinha, Polyhedron 22 (2003) 2587-2594.

15 S. Shit, P. Talukder, J. Chakraborty, G. Pilet, M.S.El. Fallah, J. Ribas, S. Mitra, Polyhedron 26 (2007) 1357-1363.

16 A. Sreekanth, U.L. Kala, C.R. Nayar, M.R.P. Kurup, Polyhedron 23 (2004) 41-47.

17 W.W. Sun, X.B. Qian, C.Y. Tian, E.Q. Gao, Inorg. Chim. Acta 362 (2009) 2744-2748.

18 S. Naiya, C. Biswas, M.G.B. Drew, C.J. Gomez-García, J.M. Clemente-Juan, A. Ghosh, Inorg. Chem. 49 (2010) 6616-6627.

19 P. Talukar, A. Datta, S. Mitra, G. Rosair, M.S.E.l. Fallah, J. Ribas, Dalton Trans. (2004) 4161-4167.

20 S. Koner , S. Saha, T. Mallah, K.I. Okamoto, Inorg. Chem. 43 (2004) 840-842.

21 S. Khan, S. Sproules, L. Natrajan, K. Harms, S. Chattopadhyay, New J. Chem. 42 (1918) 1634-1641.

22 F. Valach, M. Dunaj-Jurco, J. Garaj, M. Hvastijova, C. Czech, Chem. Commun. 39 (1974) 380-386.

23 M.L. Boillot, O. Kahn, C.J. O'Connor, J. Gouteron, S. Jeannin, Y. Jeannin, J. Chem. Soc. Chem. Commun. (1985) 178-180.

24 T. Mallah, M.-L. Boillot, O. Kahn, J. Gouteron, S. Jeannin, Y. Jeannin, Inorg. Chem. 25 (1986) 3058-3065.

25 M. Mikuriya, S. Kida, I. Murase, Bull. Chem. Soc. Jpn. 60 (1987) 1355-1359.
26 T. Mallah, O. Kahn, J. Gouteron, S. Jeannin, Y. Jeannin, J. O'Connor, Inorg. Chem. 26 (1987) 1375-1380.
27 O. Kahn, T. Mallah, J. Gouteron, S. Jeannin, Y. Jeannin, J. Chem. Soc. Dalton Trans. (1989) 1117-1126.
28 A.E. Mauro, S.I. Klein, J.S. Saldana, C.A.D. Simone, J.Z. Schpector, E.E. Castellano, Polyhedron 9 (1990) 2937-2939.
29 J.Z. Schpector, E.E. Castellano, C.A.D. Simone, G. Oliva, A.E. Mauro, Acta Cryst. Sect. C 47 (1991) 957-959.
30 M. Julve, M. Verdaguer, G.D. Munno, J.A. Real, G. Bruno, Inorg. Chem. 32 (1993) 795-802.
31 O.J. Parker, M.P. Wolther, G.L. Breneman, Acta Cryst. Sect. C52 (1996) 1089-1091.
32 R. Vicente, A. Escuer, E. Peralb, X. Solans, M.F. Bardia, Inorg. Chim. Acta 255 (1997) 1-7.
33 R.K.B. Singh, K.M.A. Malik, S.O.G. Mahalli, M.S.EI. Fallah, N.K. Karan, S. Mitra, Inorg. Chem. Commun. 4 (2001) 315-318.
34 Z. Koziskova, J. Kozisek , M. Kabesova, Polyhedron 9 (1990) 1029-1034.
35 C. Diaz, J. Ribas, N. Sanz, X. Solans, M. Font-Bardia, Inorg. Chim. Acta 286 (1999) 169-174.
36 O. Kahn, S. Sikorav, J. Gouteron, S. Jeannin, Y. Jeannin, Inorg. Chem. 22 (1983) 2877-2883.
37 J. Comarmond, P. Plumere, J.M. Lehn, Y. Agnus, R. Louis, R. Weiss, O. Kahn, I.M. Badarau J. Am. Chem. Soc. 104 (1982) 6330-6340.
38 I.B. Waksman, M.L. Boillot, O. Kahn, S. Sikorav, Inorg. Chem. 13 (1984) 4454-4459.
39 M.R. Maurya, N. Chaudhary, F. Avecilla, P. Adao, J.C. Pessoa, Dalton Trans. 44 (2015) 1211-1232.
40 M. Mishra, K. Tiwari, S. Shukla, R. Mishra, V.P. Singh, Spectro. Chim. Acta Part A132 (2014) 452-464.
41 R.N. Patel, Y.P. Singh, Y. Singh, R.J. Butcher, J.P. Jasinski, Polyhedron, 129 (2017) 164-181.
42 A.K. Singh, S. Thakur, B. Pani, E.E. Ebenso, M.A. Quraishi, A.K. Pandey, ACS Omega 3 (2018) 4695−4705.
43 A.A.R. Despaigne, G.L. Parrilha, J.B. Izidoro, P.R. Costa, R.G. Santos, O.E. Piro, E.E. Castellano, W.R. Rocha, H. Beraldo, Eur. J. Med. Chem. 50 (2012) 163−172.
44 G. A. Petersson, M.A.A. -Laham, J. Chem. Phys. 94 (1991) 6081–6090.
45 P. J. Hay, W. R. Wadt, J. Chem. Phys. 82 (1985) 270–283.

46 M.J. Frisch, G.W. Trucks, H.B. Schlegel, G.E. Scuseria, M.A. Robb, J.R. Cheeseman, G. Scalmani, V. Barone, B. Mennucci, G.A. Petersson, H. Nakatsuji, M. Caricato, X. Li, H.P. Hratchian, A.F. Izmaylov, J. Bloino, G. Zheng, J.L. Sonnenberg, M. Hada, M. Ehara, K. Toyota, R. Fukuda, J. Hasegawa, M. Ishida, T. Nakajima, Y. Honda, O. Kitao, H. Nakai, T. Vreven, J.A. Montgomery Jr., J.E. Peralta, F. Ogliaro, M. Bearpark, J.J. Heyd, E. Brothers, K.N. Kudin, V.N. Staroverov, R. Kobayashi, J. Normand, K. Raghavachari, A. Rendell, J. C. Burant, S.S. Iyengar, J. Tomasi, M. Cossi, N. Rega, J.M. Millam, M. Klene, J.E. Knox, J B. Cross, V. Bakken, C. Adamo, J. Jaramillo, R. Gomperts, R.E. Stratmann, O. Yazyev, A.J. Austin, R. Cammi, C. Pomelli, J.W. Ochterski, R.L. Martin, K. Morokuma, V.G. Zakrzewski, G.A. Voth, P. Salvador, J.J. Dannenberg, S. Dapprich, A.D. Daniels, O. Farkas, J.B. Foresman, J.V. Ortiz, J. Cioslowski, D.J. Fox, Gaussian 09, Revision D.01, Gaussian Inc., Wallingford CT, (2009).
47 R. Bauernschmitt, R. Ahlrichs, Chem. Phys. Lett. 256 (1996) 454–464.
48 M. Cossi, N. Rega, G. Scalmani, V. Barone, J. Comput. Chem. 224 (2003) 669–681.
49 T. Mosmann, J. Immunol. 65 (1993) 55-63.
50 R.T. Conley, Infrared Spectroscopy, Second Ed., Allyn & Bacon, Boston, (1966).
51 M. Sakamoto, Inorg. Chim. Acta 131 (1987) 139-142.
52 K. Nakamoto, Infrared Spectra of Inorganic and Coordination Compounds, Third ed., Wiley, New York, p.270, (1978).
53 S. Naiya, C. Biswas, M.G.B. Drew, C.J.G. García, J.M.C Juan, A. Ghosh, Inorg. Chem. 49 (2010) 6616-6627.
54 S. Sen, S. Mitra, D.L. Hughes, G. Rosair, C. Desplanches, Polyhedron 26 (2007) 1740-1744.
55 U. Singha, M.M. Dara, S. Anayutullaha, H. Alamb, N. Manzoorb, S.A.A. Thabaitic, A. A. Hashmi, J. Coord. Chem. 68 (2015) 2096-2106.
56 U. Mukhopadhyay, I. Bernal, S.S. Massoud, F.A. Mautner, Inorg. Chim. Acta 357 (2004) 3673-3682.
57 Y. Song, D.R. Zhu, K.L. Zhang, Y. Xu, C.Y. Duan, X.Z. You, Polyhedron 19 (2000) 1461-1464.
58 S. Banerjee, S. Sen, S. Basak, S. Mitra, D.L. Hughes, C. Desplanches, Inorg. Chim. Acta 361 (2008) 2707-2714.
59 A. Shaabani, A.A. Khandar, H. Mobaiyen, N. Ramazani, S.S. Balula, L.C. Silva Polyhedron, 80 (2014) 166-172.
60 Y. Anjaneyulu, R.P. Rao, Synth. React. Inorg. Met-Org. Chem. 257 (1986) 257-261.
61 N. Raman, A. Kulandaisamy, C. Thangaraja, Trans. Met. Chem. 29 (2004) 129–135.
62 S.A. Sallam, Trans. Met. Chem. 31 (2006) 46-55.
63 M.S. Nair, R.S. Joseyphus, Spectrochimica Acta Part A 70 (2008) 749–753.
64 Y. Guo, X. Hu, X. Zhang, X. Pu, Y. Wang, RSC Adv. 9 (2019) 41737-41744.
65 T.R. Felthouse, D.N. Hendrickson, Inorg. Chem. 17 (1978)444–456.
66 J.A. Weil, J.R. Bolton, Electron Paramagnetic Resonance, 2nd Ed. John Wiley & Sons: Hobroken, NJ, (2007).
67 M. Vicente, R. Bastida, A. Macıas, L. Valencia, C.F.G.C. Geraldes, C.D. Brondino,

Inorg. Chim. Acta 358 (2005) 1141–1150.
68 A. Tamayo, J. Casabo, L. Escriche, P. Gonzalez, C. Lodeiro, A.C. Rizzi, C.D. Brondino, M.C.G. Passeggi, R. Kivekas, R. Sillanp, Inorg. Chem. 46 (2007) 5665–5672.
69 A.K. Patel, R.N. Jadeja, H. Roy, R.N. Patel, S.K. Patel, R.J. Butcher, M. Cortijo, S. Herrero, Polyhedron 186 (2020) 114624.
70 F.T. Greenaway, L.J. Norris, Inorg. Chim. Acta 145 (1988) 219-284.
71 M.A. Ali, A.H. Mirza, R.J. Fereday, R.J. Butcher, J.M. Fuller, S.C. Drew, L.R. Gahan, G.R. Hanson, B. Moubaraki, K.S. Murray, Inorg. Chim. Acta 358 (2005) 3937-3948.
72 M.H.S.A. Hamid, A.A. Mohammad, M.H. Aminul, V.B. Paul, M. Boujemaa, S.M. Keith, Inorg. Chim. Acta 362 (2009) 3648-3656.
73 K. Das, A. Datta, C. Sinha, J.H. Huang, E. Garribba, C.S. Hsiao, C.L. Hsu, Chemistry Open 1 (2012) 80-89.
74 P. Zahello, Inorganic Electrochemistry: Theory, practice and applications, The Royal Society of Chemistry, U.K. 2003, p11a.
75 D.E. Richardson, H. Taube, Inorg. Chem. 20 (1991) 1278-1285.
76 R.N. Patel, Y. Singh, Y.P. Singh, A.K. Patel, N. Patel, R. Singh, R.J. Butcher, J.P. Jasinski, E. Colacio, M.A. Palacios, New J. Chem. 42 (2018) 3112-3116.
77 N. Chitrapriya, V. Mahalingam, M. Zeller, K. Natarajan, Inorg. Chim Acta 363 (2010) 3685-3693.
78 Y. Singh, R.N. Patel, S.K. Patel, R.N. Jadeja, A.K. Patel, N. Patel, H. Roy, P. Bhagriya, R. Singh, R.J. Butcher, J.P. Jasinski, S. Herrero, M. Cortijo, Inorg. Chim. Acta 503 119371 (2020).
79 G.A. Petersson. M.A.A. Laham, J. Chem. Phys. 94 (1991) 6081–6090.
80 P.J. Hay, W.R. Wadt, J. Chem. Phys. 82 (1985) 270–283.
81 R. Bauernschmitt, R. Ahlrichs, Chem. Phys. Lett. 256 (1996) 454–464.
82 A.W. Addison, T.N. Rao, J. Reedijk, J.V. Rijn, J.C. Verschoar, J. Chem. Soc. Dalton Trans. 1349-1356 (1984).
83 A. Arab, M. Habibzadeh, Comput. Theor. Chem. 1068 (2015) 52-56.
84 A.B. Deilami, M. Salehi, A. Amiri, A. Arab, J. Mol. Struct. 1181 (2019) 190-196.
85 C. Beauchamp, I. Fridovich, Anal. Chem. 44 (1971) 276-287.
86 R.G. Bhirud, T.S. Srivastav, Inorg. Chim. Acta 173 (1990) 121-125.
87 R.N. Patel, Y.P. Singh, Y. Singh, R.J. Butcher, M. Zeller, RSC Adv. 109 (2016) 107379-107398.
88 R.N. Patel, S.K. Patel, D. Kumhar, N. Patel, A.K. Patel, R.N. Jadeja, N. Patel, R.J. Butcher, M. Cortijo, S. Herrero, Polyhedron 188 (2020) 114687.
89 G. Tabbi, W.L. Driessen, J. Reedijk, R.P. Bonomo, N. Veldman, A.L. Spek, Inorg. Chem. 36 (1997) 1168-1175.
90 Y. Singh, R.N. Patel, Y.P. Singh, A.K. Patel, N. Patel, R. Singh, R.J. Butcher, J.P. Jasinski, E. Colacio, M.A. Palacios, Dalton Trans. 46 (2017) 11860-11874.
91 R.N. Patel, D.K. Patel, V.P. Sondhiya, K.K. Shukla, Y. Singh, A. Kumar, Inorg. Chim. Acta 405 (2013) 209-217.
92 Y. Li, Z.Y. Yang, J.C. Wu, Eur. J. Med. Chem. 45 (2010) 5692-5701.

Chapter 2

Copper(II) complexes with hydrazide blocking ligands

Part (B): Copper(II) tetrahedral complex derived from N'-[(2E,3Z)-4-hydroxy-4-phenylbut-3-en-2-ylidene]acetohydrazide: Synthesis, molecular structure, quantum chemical investigations, antioxidant and antiproliferative properties

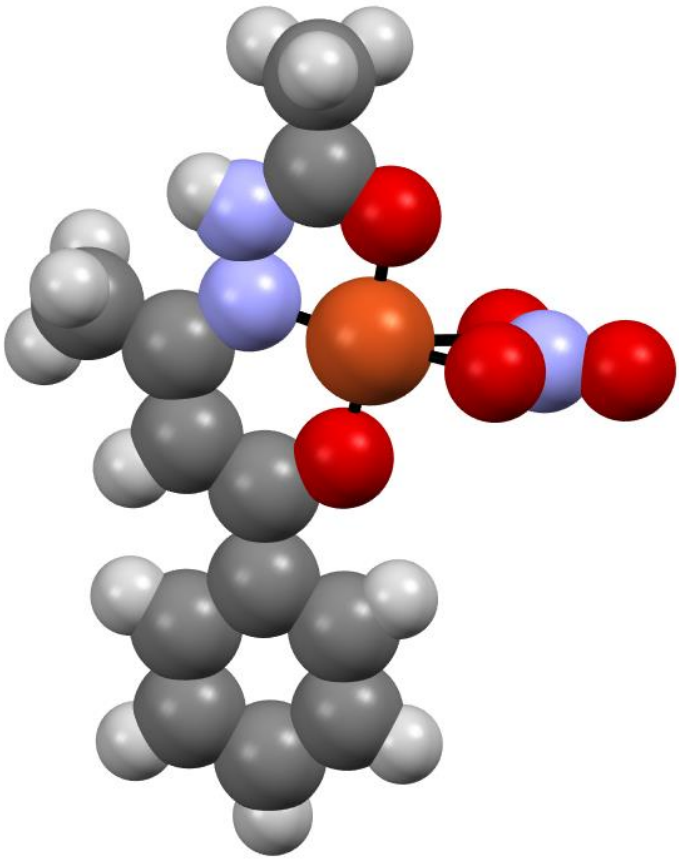

1 Introduction

Few copper(II) complexes have acquired much attention owing to their unusual structural features and biological importance [1, 2]. In this context, copper(II) complexes having unusual structural features in four coordinate is pseudo tetrahedral geometry. The geometry of metal centers in these complexes remains nearly tetrahedral. The geometry index for four coordinate complexes is given by $\tau_4 = 360- (\theta_1 – \theta_2)/141$, where θ_1 and θ_2 are the two largest angles. The values of τ_4 range from 1 for perfect tetrahedral geometry to zero for a perfect square planar geometry. Therefore, the pseudo tetrahedral geometry may consider as intermediate geometry of all within the range of zero to unity. The value of τ_4 should be close to the value of tetrahedral with τ_4 ~1.0 in pseudo tetrahedral complexes. These copper(II) complexes show unusual electronic and EPR spectral features [3-8]. Such spectroscopic behavior is shown by blue copper proteins (Type 1). The unique feature of Type 1 copper centers is the very intense absorption in the red spectral region. It is observed that such bands are due to ligand to metal charge transfer electronic transition. Such four coordinate complexes having intermediate geometry should be exceptionally useful models for copper redox proteins [9].

Schiff base is a versatile tridentate ligand. These are the organic compounds with biological importance [10-12]. Schiff base (hydrazones) have been widely used for the synthesis of transition metal complexes. Several biological properties of copper(II) complexes with hydrazone have been synthesized and characterized [13-15].

In this part of thesis one copper(II) complex using HL = N'-[(2E,3Z)-4-hydroxy-4-phenylbut-3-en-2-ylidene]acetohydrazide was synthesized. This complex was synthesized and characterized by various physicochemical techniques. The solid-state structure has been determined using single-crystal X-ray analysis. The geometry for this complex has been pseudo tetrahedral τ_4 = 0.81. The density functional theory was used to compute the molecular structure, HOMO-LUMO and natural bond order (NBO) analysis. The binding of the Schiff base to the copper(II) has been explored using X-band epr spectral measurements. Similarly, electrochemical behavior has been studied using cyclic voltammetry and differential pulse voltammetry. The antioxidant SOD activity has been collected. Antiproliferative and cancer properties in vitro of the complex have also been collected using human cancer cell lines including human cell lines, IMR 32 (Neuroblastoma), MCF 7 (Breast cancer), HepG2 (Hepatocellular carcinoma) and L132 (lung cells).

2 Experimental

2.1 Materials and Instrumentation

Solvents were dried and distilled before their use standard procedures [16]. Reagent-grade chemicals were used throughout, and HPLC-grade solvents were employed for spectroscopic studies. The metal nitrates $Cu(NO_3)_2 \cdot 5H_2O$ (98.0% purity) and was purchased from Sigma-Aldrich Chemical Co. Pvt. Ltd. and used as received.

2.2 Synthesis of ligand HL

To a solution of 1-benzoyl acetone (1.62 g, 10 mmol) in absolute ethanol (50 ml), acetyl hydrazide (0.7 8g, 10 mmol) was added. The resulting solution was refluxed at 75 °C for 3 hrs. The yellowish solution was filtered and the filtrate was kept for slow evaporation at room temperature to yield a light-yellow polycrystalline sample. The Schiff base was washed with ethanol and dried over fused $CaCl_2$.

M.P.: 125 °C. Yield: ~ 78%. Anal. Calc. for $C_{12}H_{14}N_2O_2$ (218.26 g mol^{-1}): Elemental Analysis: C, 66.07; H, 6.47; N, 12.86%; Found: C, 66.06; H, 6.48; N, 12.84%. FTIR bands (KBr, cm^{-1}): ν(C=O) 1601, ν(C=N) 1571. ^{1}H NMR (DMSO-d_6) δ: 12.1 (s, 1H, OH), 10.3 (s, 1H, -NH-), 7.8-7.3 (m, 6H, Ar-H), 2.2 (s, 2H, C-CH_3), 1.99 (s, 3H, CH_3) ppm. ^{13}C NMR (DMSO-d_6) δ: 169 (C-OH), 154 (C=O), 144 (CH=N-), 131-91 (Ar-C), 23.3 (-CO-CH_3), 16.1 (CH-CH_3) ppm.

2.3 Synthesis of Complex [Cu(HL)(NO_3)]

The Schiff base ligand (0.281g, 1.0 mmol) was dissolved in methanol (20 mL). A solution of $Cu(NO_3)_2.3H_2O$ (0.241 g, 1.0 mmol) in methanol (20 mL) was added dropwise to the above solution with stirring for 5 hrs to give a green clear solution. The resulting solution was filtered. The filtrate was left for slow evaporation at room temperature. Plate-like crystals were formed from the solution two weeks later. These crystals were washed with hot distilled water and then ethanol to remove impurities. The crystals were dried under a vacuum.

Yield: ~ 73%. Anal. Calc. for $C_{12}H_{13}CuN_3O_5$ (342.79 g mol^{-1}): Elemental Analysis: C, 43.62; H, 4.51; N, 11.51%; Found: C, 43.65; H, 4.52; N, 11.78%. FTIR bands (KBr, cm^{-1}): ν(C=O) 1593, ν(C=N) 1563. ESI-Mass (m/z): 344.18.

2.4 X-Ray Crystallography

X-Ray data was collected on Bruker CCD area detector with graphite monochromatized MoKα radiation (λ = 0.71073 Å). The diffraction data was solved by using SHELXS-97 [17, 18] software and refined by a full-matrix least-squares technique based on F2. The calculation was performed by using the SHELXS-97 [19, 20] crystallographic software package. Non–hydrogen atoms were refined anisotropically and all hydrogen atoms were geometrically fixed and allowed to refine using a riding model. Atomic scattering factors were taken from International Tables for X-ray Crystallography [21]. Molecular drawings were obtained using the ORTEP program. Crystals suitable for single-crystal X-ray analysis of complex were grown by slow evaporation of the reaction mixtures at room temperature. These crystals were mounted on polymer loops and used for data collection. Crystal data of complex were collected on a Rigaku Oxford Diffraction Gemini Eos diffractometer using graphite monochromated Mo-Kα radiation. The structure was solved by direct methods by using SHELX [22] and refined with SHELXL-2014 [23]. All the non-hydrogen atoms were refined anisotropically and all the hydrogen atoms were geometrically fixed and refined using a riding model.

2.5 Physical measurements

Infrared (IR) spectra were recorded on a Bruker spectrophotometer at normal temperature. KBr pellets were prepared by grinding the sample with KBr (IR grade), in the range of 400 to 4000 cm^{-1}. NMR spectra of HL were recorded in DMSO-d_6 on Bruker Advance 400 (FT-NMR) multinuclear spectrometer. Electronic absorption spectra (300–900 nm) were recorded with a Shimadzu UV-Vis recording spectrophotometer UV-1601 in solution. ESI Mass spectrometry was recorded on a XEVO G2-XS QTOF. The electrochemistry of the complex (3×10^{-3} M) in DMSO containing 0.1 M tetra-butylammonium perchlorate (TBAP) as supporting electrolyte was determined at room temperature by cyclic voltammetry (CV) using a three-electrode system under de-aerated conditions and a BAS 100 electrochemical analyzer. A glassy-carbon electrode and platinum wire were used as the working electrode and the counter electrode, respectively. The reversibility of the electrochemical process was evaluated by standard procedures and all potentials were recorded against an Ag/AgCl reference electrode. All measurements were carried out at 298 K under nitrogen. All solutions were purged with nitrogen gas before measurements. The low and room temperature electron paramagnetic resonance (EPR)

spectra were obtained with a Varian E-line Century Series Spectrometer equipped with a dual cavity and operating at X-band with 100 kHz modulation frequency. Varian quartz tubes were used for obtaining the EPR spectra of the polycrystalline samples and frozen solutions with tetracyanoethylene (TCNE) as a marker (g = 2.00277). Magnetic susceptibility of the polycrystalline sample was obtained by the Gouy balance using mercury(II) tetrathiocynato cobaltate(II) as calibrating agent (χ_g = 16.44 x 10^{-6} c.g.s. units) diamagnetic correction were taken from Pascal tables.

2.6 Computational method

Full geometry optimizations were carried out using the density functional theory (DFT) method at the B3LYP level for complex [24]. All elements except Cu were assigned the 6-31G(d) basis set [25]. LANL2DZ with effective core potential for Cu atom was used [26]. The vibrational frequency calculations were performed to ensure that the optimized geometries represent the local minima and that there is only a positive Eigenvalue. In the computational model, the cationic complex was taken into account. All calculations were performed with the GAUSSIAN09 program [27], with the aid of the Gauss View visualization program. Vertical electronic excitations based on B3LYP optimized geometries were computed using the time-dependent density functional theory (TDDFT) formalism [28] in DMSO, using a conductor-like polarizable continuum model (CPCM) [29].

2.7 Anti-cancer activity of complex

2.7.1 Cell culture

Human cell lines, IMR 32 (Neuroblastoma), MCF 7 (Breast cancer), HepG2 (Hepatocellular carcinoma), L132 (lung cells) were procured from the National centre for cell science (NCCS), Pune and cultured in Dulbecco's Modified Eagle Medium (DMEM), supplemented with 10% fetal bovine serum (FBS) and 1% antibiotics solution. All the cell lines were maintained in a CO_2 incubator at 37° C temperature in a 5% CO_2 humidified environment.

2.7.2 Cytotoxicity Assay *in vitro*

Cytotoxicity of the present complex was measured using an MTT assay [30]. Cells were plated into 96 well plates at a density of 5000 cells/ well and allowed to adhere for

overnight. The synthesized compound was diluted in five different concentrations and cells were exposed for 24 hours. Further, cells were incubated for 4 hours with MTT solution. After incubation MTT solution was removed and formazone crystal was dissolved in 200µl of DMSO. End of the reaction, 0ptical density was measured at 540nm using an ELISA plate reader.

2.7.3 RNA Isolation and Gene Expression Study

Total RNA was isolated from cells using TRIzol® Reagent (Invitrogen). Cells were treated for 24 hours with YP01 and used for RNA extraction. The RNA pellet was dissolved in 25µl of DEPC water and used for further study. RNA was quantified using NanoDrop Spectrophotometer and quality was analyzed on 2% Agarose gel electrophoresis. 1µg of RNA was reverse transcribed using BIO-RAD iScript cDNA synthesis kit and cDNA was synthesized. Expression of Bax, Bcl2, Caspase-9 and p53 were studied using Real-Time PCR. β-actin was used as the reference gene. Primers of different gene was designed using NCBI Blast (Bcl2: F-5'GCCCGAGAACCTAATGGCTT 3', R-5'CTCAGGGACTCACTCTGCTG 3'; Bax: F - 5'GCCCTTTTGCTTCAGGGTTT 3', R-5'GGAAAAAGACCTCTCGGGGG 3'; p53: F- 5'CATAGTGTGGTGGTGCCCTA3', R-CACCTCAAAGCTGTTCCGTC; Caspase 9: F- 5'ATG GAC GAA GCG GAT CGG 3', R-5'CCCTGGCCTTATGATGTT 3' and β-actin: F- 5' CCACCATGTACCCTGGCATT 3', R-5' CGCTCAGGAGGAGCAATGAT 3'). Real-time PCR was performed on cDNA using Power up SYBR Green mix purchase from Thermo Fisher Scientific and used accordingly manufacturer instruction. The quantitative RT-PCR data were analyzed accordingly comparative threshold (Ct) method, and the fold inductions of samples were compared with the untreated sample.

2.7.4 Apoptosis Assay

Cell death was observed by dual staining using acridine orange and ethidium bromide (AO/EB). Coverslips were autoclaved and coated by Poly L- Lysine. The coverslip was kept in a six-well plate and HepG2 cells were incubated overnight. Cells were treated by compound for 24 hours. After incubation cells were washed with PBS and stained by AO/EB for 20 minutes. Cells were washed and observed under the microscope for analysis of cell death.

3 Results and discussion

The copper(II) complex was synthesized using 1-benzoyl acetone and acetyl hydrazide as a ligand (Scheme 1). The complex [Cu(HL)(NO_3)] has been synthesized by a general procedure based on mixing a methanolic solution of copper nitrate with a methanolic solution of the ligand in a 1:1 molar ratio Scheme 2. The complex has been characterized by FT-IR, UV-Vis, CV, ESI-Mass, Hirshfeld analysis and X-ray analysis. The SOD and anti-cancer activity of complex have been also evaluated.

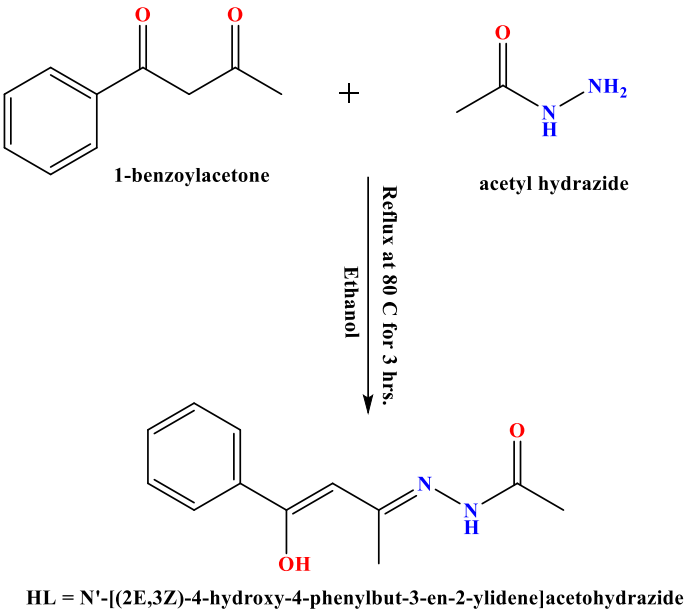

Scheme 1 Synthetic route for the preparation of the ligand (**HL**).

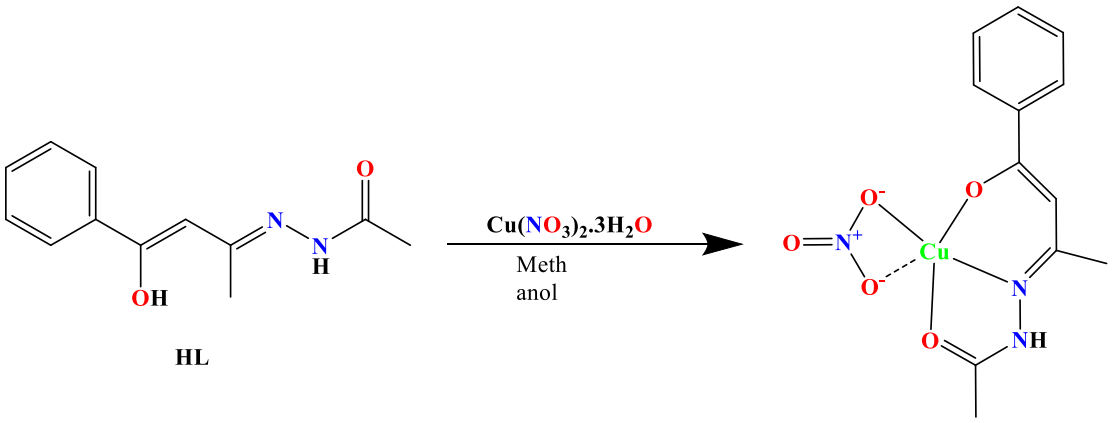

Scheme 2 Synthetic route of the complex **[Cu(HL)(NO_3)]**.

3.1 NMR spectra of Ligand

The ^{1}H and ^{13}C NMR spectra of ligand (HL) were recorded in DMSO-d_6 solvent. In ^{1}H NMR of spectra of ligand hydroxy (-OH) peak is obtained at 12.1 ppm. The NH peak is obtained at 10.3 ppm. All aromatic peaks along with aliphatic are obtained at the range of 7.8-7. ppm. Two methyl peaks are obtained at 1. and 2.2 ppm. In ^{13}C NMR (C-OH) peak and carbonyl (C=O), carbon peaks are obtained at 169 and 154 ppm. Similarly, azomethine carbon (CH=N) peak is obtained at 144 ppm. All other carbon peaks are obtained at 131-92 ppm. Two methyl carbon peaks are obtained at 16 and 23 ppm. The ^{1}H and ^{13}C NMR spectra are shown in Fig. 1 and 2.

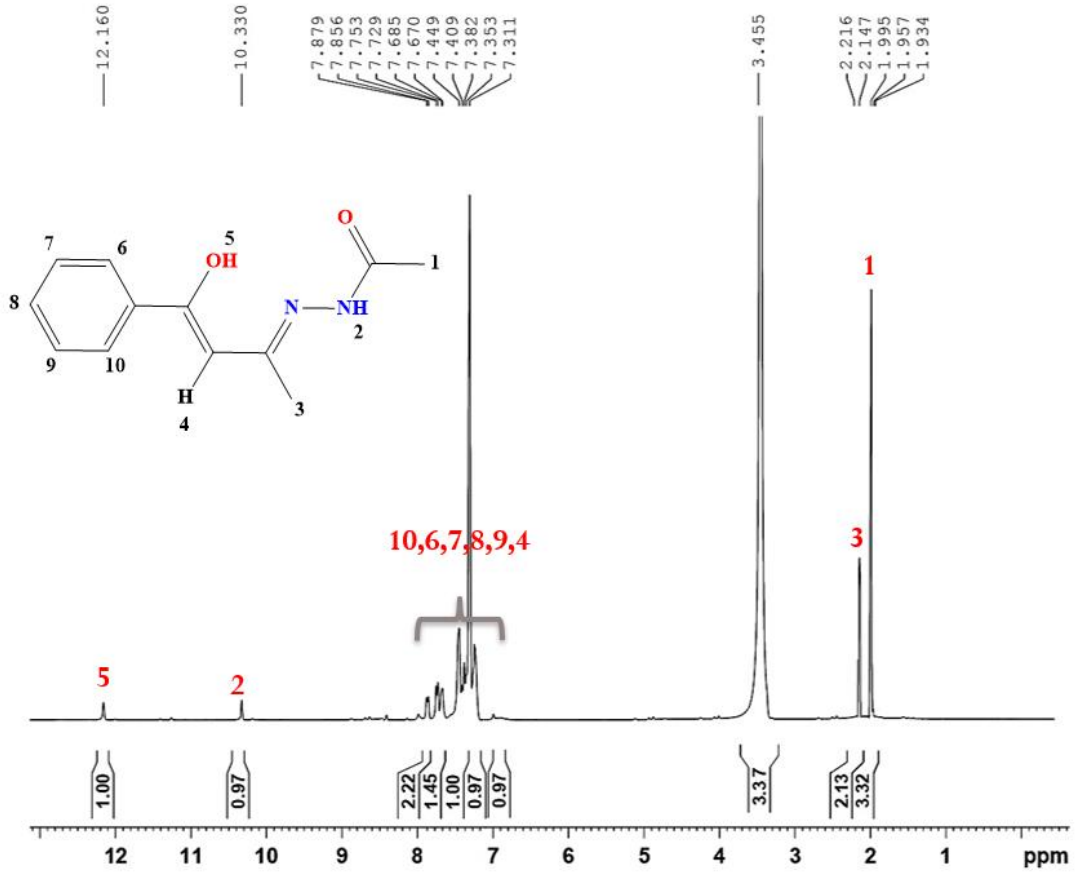

Fig. 1. ^{1}H NMR spectra of the ligand HL.

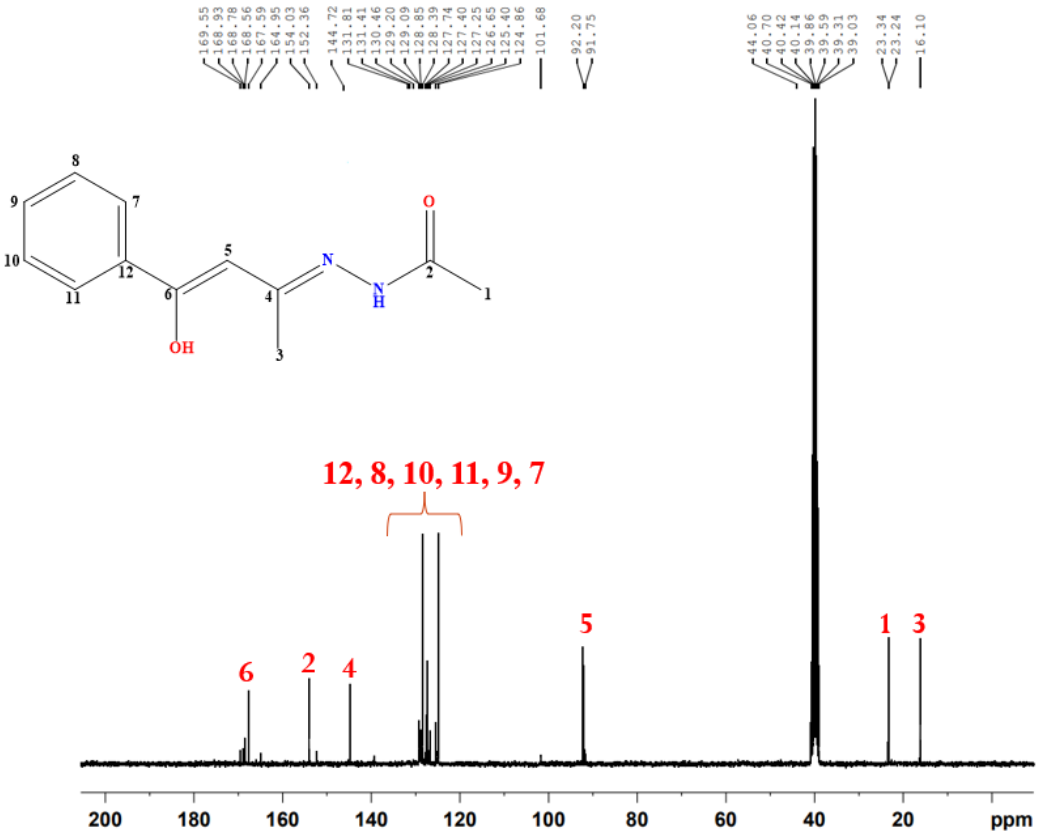

Fig. 2. ^{13}C NMR spectra of the ligand HL.

3.2 Crystal structure of complex

An ORTEP view of the complex with its atom numbering scheme is shown in Fig. 3. Single crystallographic data and molecular structure refinement data are presented in Table 1. The selected bond lengths and bond angles are shown in Table 2. This complex crystallizes in the triclinic space group (*P*-1). The copper(II) centre in this complex is four coordinated by two oxygen atoms (O1 and O2) and one nitrogen atom (N1) of the Schiff base and one oxygen atom (O3) of the nitrate ligand, forming a pseudo tetrahedral geometry. The oxygen atom of nitrate is weakly coordinated with copper(II) centre. In this complex, the Cu(II) centre in an approximate pseudo-tetrahedral geometry is ascertained by the value of τ-index ($\tau_4 = 360^0 - (\alpha + \beta) / 141^0$), where α and β are the two largest angles in four coordinate complexes [31]. The value of τ_4 would range from 1.00 for a perfect tetrahedral geometry to zero for a perfect square planar geometry. For this complex τ_4 is 0.81. Therefore, the geometry of copper ions is approximately tetrahedral. The Cu−N and Cu−O bond distances of this complex are comparable to those of some reported four coordinate geometry of Cu(II) complexes [32-34]. The selected B3LYP/LAN2DZ calculated bond distances and bond angles (presented in the next section) are also given in Table 2. Theoretically calculated bond distances and bond angles in the theoretical model complex are in good agreement with the

corresponding experimental X-ray data [35-37]. The root means square deviation (RMSD) has also been calculated and is shown in Table 2. From the perusal of theoretical and experimental data, a better agreement has been obtained with RMSD = 0.001 for bond distances and 0.974 for bond angles. The crystal lattice is aggregated through $C-H\cdots O$ hydrogen in bonds and π···π (aryl and metal chelate) interactions. The $C-H\cdots O$ hydrogen bonds are formed between hydrogen atoms of Schiff base and coordinated nitrate oxygen atoms of the adjacent complex molecule (C2H2A···O) with a distanced (H···A) of 2.713Å. Thus, two hydrogen bonds resulting in a dimer-like association between pairs of complexes in an extended heterosynthon (motif) R_2^2 (16) Fig. 4. The π···π (aryl-metal chelate) interactions [centroid-centroid distances = 3.763Å] that occurs between π clouds of the phenyl ring and π clouds of five-membered chelate rings (Fig. 5). Noncovalent interactions (π−π) and hydrogen bonds form the supramolecular network. Hydrogen bonds (Table 3) also play a central role in the structure, function and dynamics of biological and chemical models [38]. Thus, hydrogen bonding and π···π interactions establish in form of the dimer in the crystal "network".

(a)

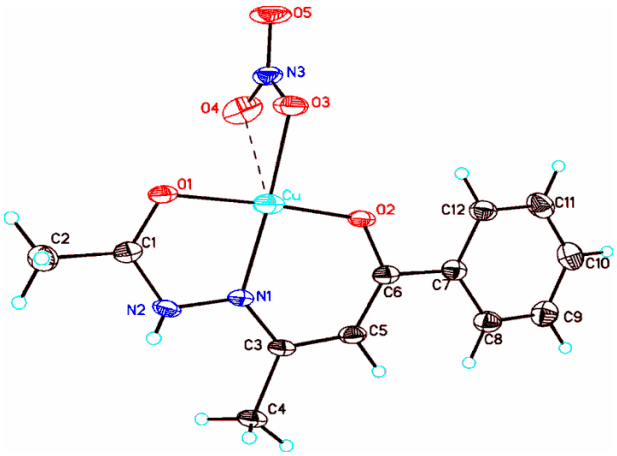

(b)

Fig. 3(a). Crystal image and **(b)** ORTEP view of the complex [Cu(L)(NO_3)].

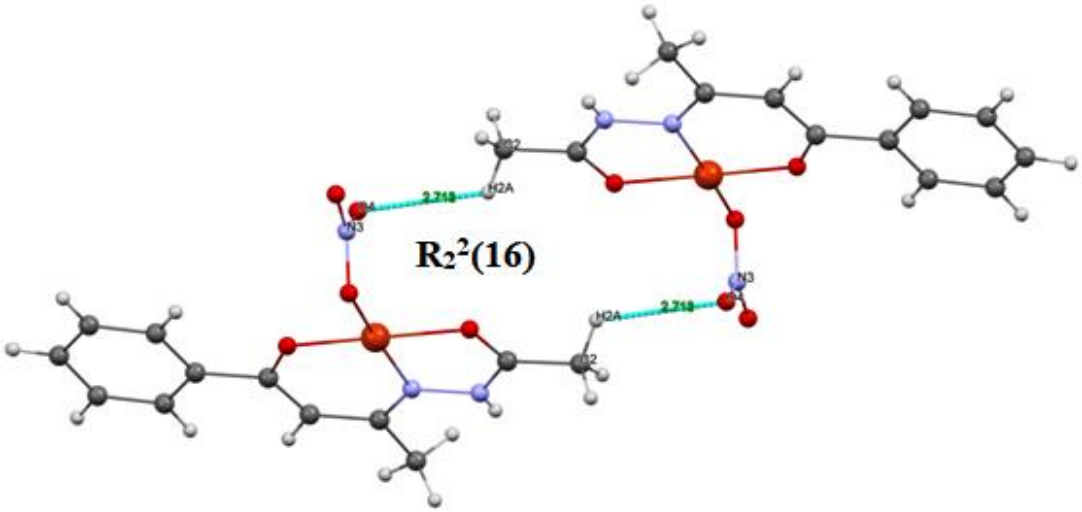

Fig. 4. Intermolecular H-bonding interactions with heterosynthon motif of complex [Cu(L)(NO_3)].

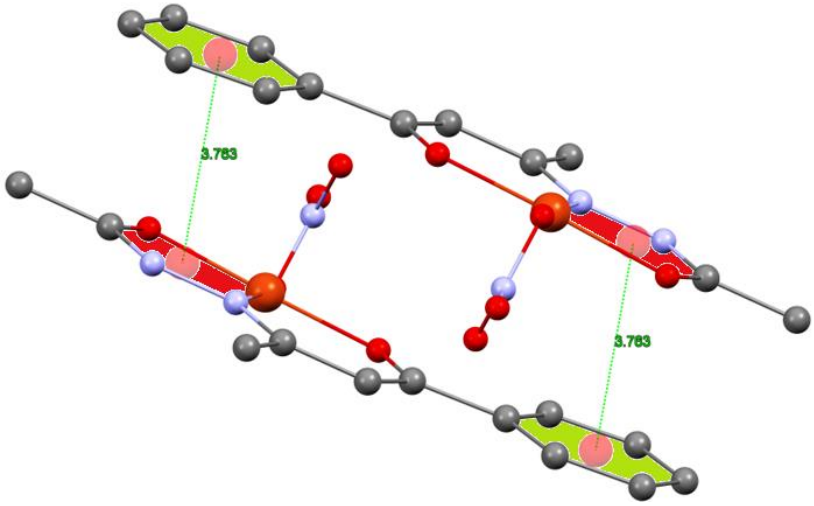

Fig. 5. π···π interactions in the complex [Cu(L)(NO_3)].

Table 1 Crystallographic data and structure refinement for the complex [Cu(L)(NO_3)].

Empirical formula	**$C_{12}H_{13}CuN_3O_5$**
Formula weight	342.79
Temperature (K)	150(2)
Crystal system	Triclinic
Space group	*P -1*
a (Å)	7.065(5)
b (Å)	8.976(5)
c (Å)	11.218(5)
α(°)	85.878(5)
β(°)	72.158(5)
γ(°)	87.699(5)

Volume ($Å^3$)	675.3(7)
Z	2
ρ_{calc}g/cm^{-1}	1.686
M (mm^{-1})	1.643
F(000)	350
Crystal size (mm^3)	0.21 x 0.17 x 0.14
2Φ range for data collection (°)	1.911 to 25.863
Index ranges	-8<=h<=6, -11<=k<=10, -13<=l<=13
Reflections collected	2533
Independent reflections	2533 [R(int) = 0.0184]
Data / restraints / parameters	2533 / 0 / 196
Goodness-of-fit on F^2	1.042
Final R indices [I>=2σ(I)]	R1 = 0.0599, wR2 = 0.1775
R indices (all data)	R1 = 0.0624, wR2 = 0.1813
Largest diff. peak/hole ($eÅ^{-3}$)	0.732 and -0.750

Table 2 Bond lengths [Å] and bond angles [°] for the complex. (esd's are reported in parathesis).

Bond length	XRD	DFT
Cu-O(2)	1.881(3)	1.881
Cu-N(1)	1.917(3)	1.918
Cu-O(4)	2.591(4)	2.591
Cu-O(3)	1.984(3)	1.984
Cu-O(1)	1.954(3)	1.955
RMSD		0.001
Bond angle		
O(2)-Cu-N(1)	93.91(12)	93.902
O(2)-Cu-O(1)	175.35(11)	174.671
N(1)-Cu-O(3)	170.23(14)	173.071
O(1)-Cu-O(3)	91.01(14)	90.997
O(1)-Cu-O(4)	91.01(13)	91.006
N(1)-Cu-O(1)	82.07(12)	82.074
O(2)-Cu-O(3)	93.26(14)	93.275
O(2)-Cu-O(4)	90.04(13)	90.050
N(1)-Cu-O(4)	133.11(14)	133.098
O(3)-Cu-O(4)	53.48(14)	53.482
RMSD		0.974

Table 3 Hydrogen bonds for complex [Cu(L)(NO_3)] [Å and °].

D-H...A	d(D-H)	d(H...A)	d(D...A)	<(DHA)
N(2)-H(2N)...O(5)#1	0.62(4)	2.27(4)	2.858(5)	160(5)
C(2)-H(2C)...O(5)#1	0.98	2.55	3.297(6)	132.9

3.3 DFT based frontier orbital analysis

The six important α and β molecular orbitals (MOs), viz., HOMO-2, HOMO-1, HOMO, LUMO, LUMO+1 and LUMO+2 were analysed for the present complex (Fig. 6). HOMO (highest occupied molecular orbital) and LUMO (lowest occupied molecular orbital) are collectively referred to as frontier orbitals and are important parameters for describing chemical behaviours [39]. The HOMO orbitals are primarily electron donors whereas LUMO is electron acceptors. Similarly, the gap between HOMO and LUMO describes the chemical stability of molecules [40]. The computed energies of six α-spin state molecular orbitals (HOMO-2 to LUMO+2) for the complex are -5.440 eV, -5.368 eV, -4.730 eV, -5.795 eV, -4.051 eV and -0.996 eV respectively and energy gap (ΔE) between (HOMO – LUMO), (HOMO-1 – LUMO+1), (HOMO-2 – LUMO+2) for the complex are 1.065 eV, 1.317 eV and 4.444 eV respectively. Similarly, six MOs energies of β-spin states (HOMO-2 to LUMO+2) are also estimated for the complex viz., -5.437 eV, -9.307 eV, -4.765 eV, -5.790 eV, -5.088 eV and 1.086 eV while the energy gap between (HOMO – LUMO), (HOMO-1 – LUMO+1), (HOMO-2 – LUMO+2) are 1.025 eV, 0.219 eV and 4.351 eV respectively. The presence of single unpaired electrons in the HOMO justifies paramagnetic behaviour of the complex and hence HOMO is termed as singly occupied molecular orbital (SOMO). In HOMO – LUMO structure, LUMO+2 is mainly concentrated on the C=N group whereas HOMO-2 is mainly localized on the phenyl ring of Schiff base in the α-spin state. α-LUMO is mainly localized on C=O group of the Schiff base. The remaining α-HOMO-1, α-HOMO and α-LUMO+1 are localized on nitrate moiety of the complex. Similarly, β-LUMO+2 mainly localized on the C=O group and β-HOMO-2 on the phenyl ring of Schiff base ligand β-HOMO-1 and β-LUMO are localized on nitrate moiety of the complex. Only β-LUMO+1 localized on the central atom of the complex.

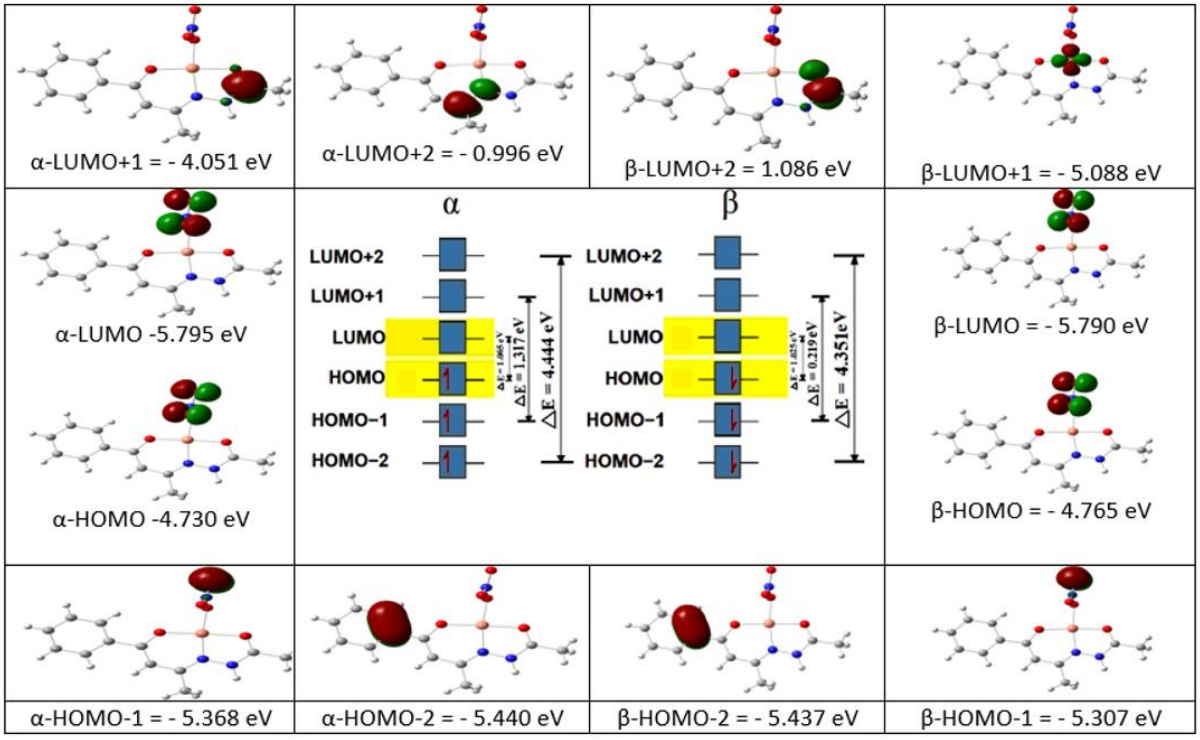

Fig. 6. HOMO-LUMO structure with energy level diagram of complex **[Cu(L)(NO_3)]**.

3.4 Natural bond orbital (NBO) analysis

The NBO analysis of complex was done by B3LYP/LANL2DZ level basis set. The selected bond lengths and angles are given along the crystallographic data (Table 1). The observed bond lengths and angles exactly tally with the experimentally observed values. The NBO analysis is used to predict the delocalization of electron density between occupied Lewis-type orbitals and unoccupied non-Lewis NBOs (Rydberg), which correlate to a stabilizing donor-acceptor interaction [41]. As per NBO analysis, all of the interactions between the copper(II) ions and all of the nitrogen and oxygen donor atoms were regarded as coordination bonds (N→Cu or O→Cu). Such type of interactions attribute to a donation of the electron density from the lone pair orbital on the nitrogen or oxygen atoms, LP(N) or LP(O) to the antibonding orbital on the copper ion LP^*(Cu). The selected orbitals involved in the strongest LP(N) → LP^*(Cu) and LP(O) → LP^*(Cu) interactions are depicted in Fig. 7. The natural atomic configuration for Cu^{2+} = +0.641, O_1 = -0.431, O_2 = -0.324, O_3 = -0.294 and for N_1 = -0.323. Similarly, natural electronic configuration of Cu is: [Core] 4s (0.31) 3d (9.35) 4p (0.34) and natural population analysis of Cu is: core electrons (17.9954), valence electrons on 4s, 4p and 3d orbital (9.9979) and Rydberg electrons on 4p, 4d and 5p orbitals (0.01047) give 27.99338 electrons. Before complexation, the charge on copper is +2, while the charge of the

copper(II) ion in complex is +0.641. These shows that ligand transfer own negative charge to copper(II) ion during complex formation.

Donor	Acceptor	Interaction
LP(N)	LP*(Cu)	LP(N)→ LP*(Cu)
LP(O)	LP*(Cu)	LP(O)→ LP*(Cu)

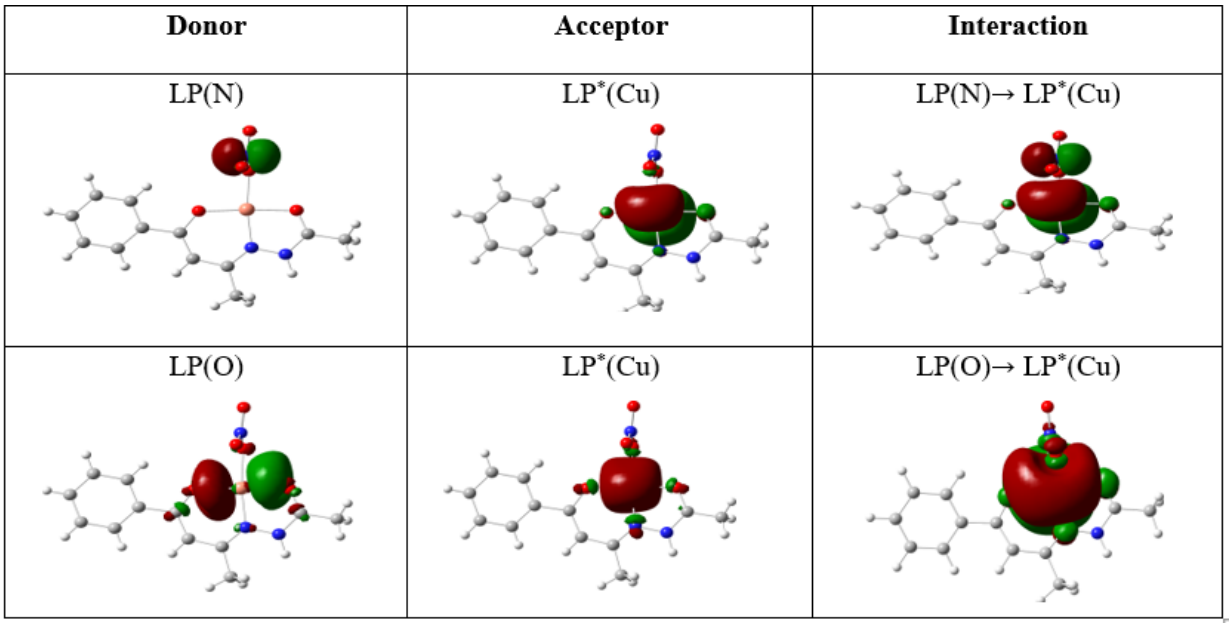

Fig. 7. The donor and acceptor orbitals involved in the LP(N) → LP*(Cu) and LP(O) → LP*(Cu) interactions [Cu(L)(NO_3)].

3.5 Hirshfeld Surface Analysis

Molecular Hirshfeld surfaces [42] in the crystal structure were constructed on the basis of the electron distribution calculated as the sum of spherical atom electron densities [43, 44]. For a given crystal structure and a set of spherical atomic densities, the Hirshfeld surface is unique [45]. The normalized contact distance (d_{norm}) based on both d_e and d_i (where d_e is distance from a point on the surface to the nearest nucleus outside the surface and d_i is distance from a point on the surface to the nearest nucleus inside the surface) and the vdW radii of the atom, as given by eq 1 enables identification of the regions of particular importance to intermolecular interactions [42]. The combination of d_e and d_i in the form of two-dimensional (2D) fingerprint plot [46, 47] provides a summary of intermolecular contacts in the crystal [42]. The Hirshfeld surfaces mapped with d_{norm} and 2D fingerprint plots were generated using the Crystal-Explorer 2.1 [48]. Graphical plots of the molecular Hirshfeld surfaces mapped with d_{norm} used a red-white-blue colour scheme, where red highlight shorter contacts, white represents the contact around vdW separation, and blue is for longer contact. Additionally, two further coloured plots representing shape index and

curvedness based on local curvatures are also presented in this paper [49].

$$d_{norm} = \frac{d_i - r_i^{vdW}}{r_i^{vdW}} + \frac{d_e - r_e^{vdW}}{r_e^{vdW}} \quad (1)$$

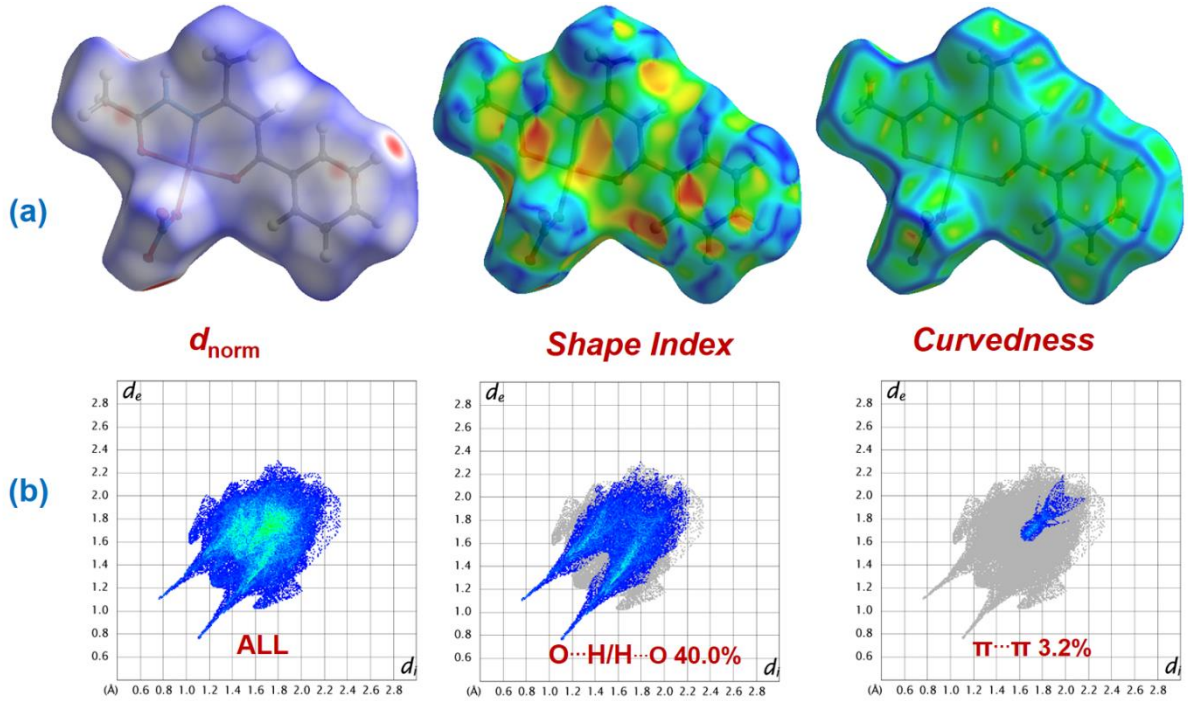

Fig. 8(a) Hirshfeld surfaces mapped with d_{norm}, shape index and curvedness for the complex; **(b)** Fingerprint plots for the complex showing percentages of contact contributed to the total Hirshfeld surface area in the complex.

The Hirshfeld surfaces for the copper complex is shown in Fig. 8. For gain idea about the molecular framework especially the aromatic and chelate rings the surfaces are plotted as transparent. The d_{norm} surface is mapped between -0.25 to 1.25 Å range, shape index plots are constructed between -0.8 to 0.8 Å while curvedness plots are mapped in the range -3.0 to 0.3 Å. In this complex, the O···H interactions as described in crystal structure description (*vide supra*) can be seen as the large circular deep red depressions and the weaker π···π interactions is shown as the faint red shaded area.

Another salient result of the Hirshfeld surface analysis are the fingerprint plots (Fig. 8(b)). In this plot, the complementary regions are presented in such a manner where one molecule act like donor ($d_e > d_i$) and another as acceptor ($d_e < d_i$). Also, the total fingerprint plot can be cleaved in several fragments to lay emphasis on specific atom pair close contacts. This helps to estimate the varied contributions of interactions that are present in the molecule.

The fingerprint plots of the complex show equal sized pair of spikes as the light blue region. The most important interaction in the complex is the O···H/H···O interaction which appear as discrete spikes 0.7 Å < (d_e + d_i) < 2.2 Å in the total fingerprint plot of the complex. This is the most dominant interaction existing in the complex with total contribution of 40.0% in the total Hirshfeld surface area. Apart from this the complex exhibit π···π interaction which appears in 1.6 Å < (d_e + d_i) < 2.2 Å in the middle of the fingerprint area with net contribution of 3.2%.

3.6 FTIR spectral studies

The FTIR spectrum of the complex was analyzed in comparison with that of free ligand (HL) in the region 4000-400 cm^{-1}. The IR data gave the evidence for the coordination of ligand (HL) to the copper(II) ion via two oxygen and one nitrogen atoms. The characteristic ν(N−H), ν(C=O), ν(C=N) and ν(N−N) bands appeared at 3257, 1593, 1563 and 1090 cm^{-1} in the complex. The IR spectrum of the ligand shows absorption bands of ν(N−H), ν(C=O), ν(C=N) and ν(N− N) at 3253, 1580, 1603 and 1103 cm^{-1}. From the perusal of complex and ligand IR absorption bands, it is clear that ν(N−H) remains unshifted, which shows that NH is not deprotonated upon complexation. The absorption band of the C=O is downward shifted in the metal complex. Therefore, carbonyl oxygen is coordinated with metal ions as confirmed by the X-ray structure [50-52]. The absorption band of C=N is also downward shifted and therefore, it is reasonable to consider that azo nitrogen (>C=N) is coordinated to the metal [53]. The band due to ν(N−N) is seen in both HL and metal complex but upshifted in metal complex, suggesting coordination of the nitrogen atom of >N− N< group to the metal (Fig. 9 and 10). In metal complex new bands at 1450, 1388 and 1031 cm^{-1} displayed are due to a coordinated nitrate ion. The coordinated unidentate nitrate displayed these bands owing to the $\nu_{asym}(NO_2)$, $\nu_{sym}(NO_2)$ and ν(NO) vibrating modes [54-56]. One non-ligand band seen at 436 cm^{-1} corresponds to ν(M−O) stretching vibration.

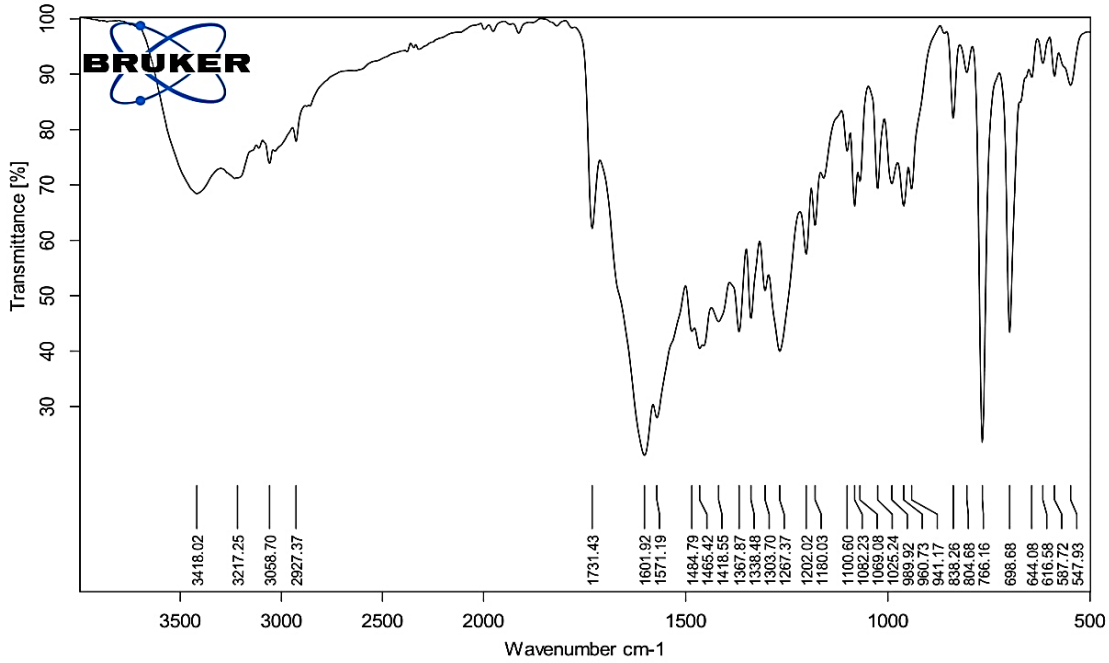

Fig. 9. FTIR spectrum of ligand **HL**.

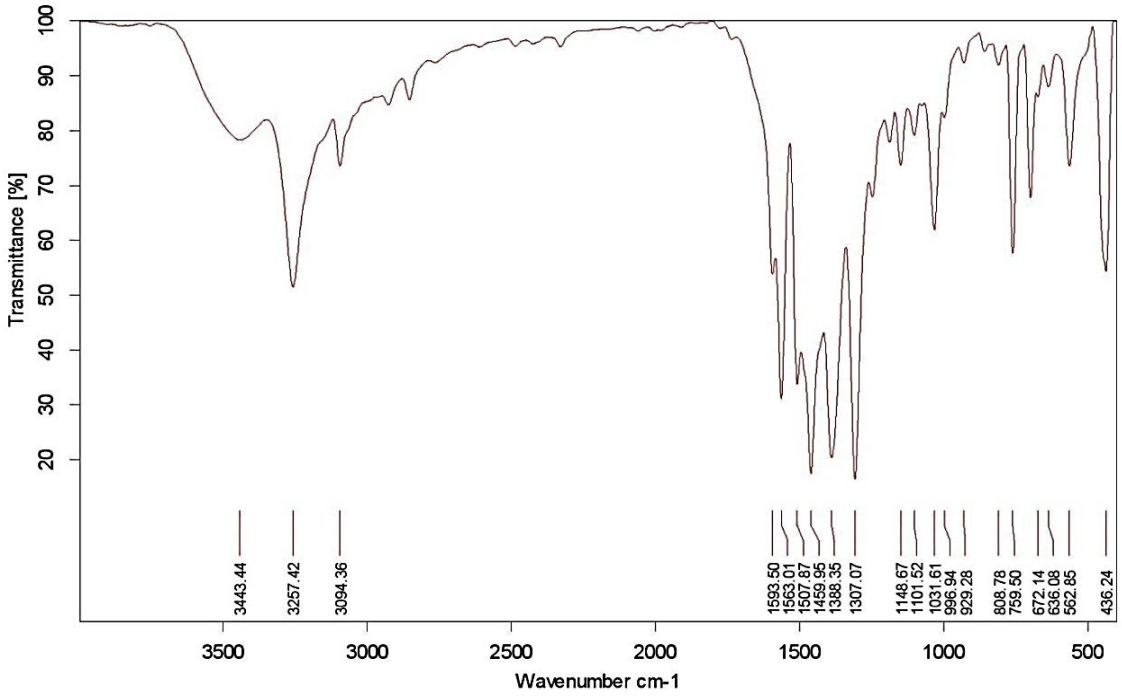

Fig. 10. FTIR spectrum of complex **[Cu(L)(NO_3)]**.

3.7 Electronic spectral studies

The ligand field absorption spectrum is also measured. The absorption bands of complex in DMSO are shown in Fig. 11. The visible absorption spectra is observed by the intense bands at a shorter wavelength. The band originates at 614 nm has $^2T_2 \rightarrow {}^2E$ transition.

The most striking spectroscopic feature is the appearance of a band at 408 nm due to ligand to metal charge-transfer (LMCT) transition. One more high-energy intense band observed at 303 nm is due to the $\pi\cdots\pi^*$ transition of the Schiff base. Such spectral features have already been discussed in several pseudo-tetrahedral copper(II) complexes [57-59].

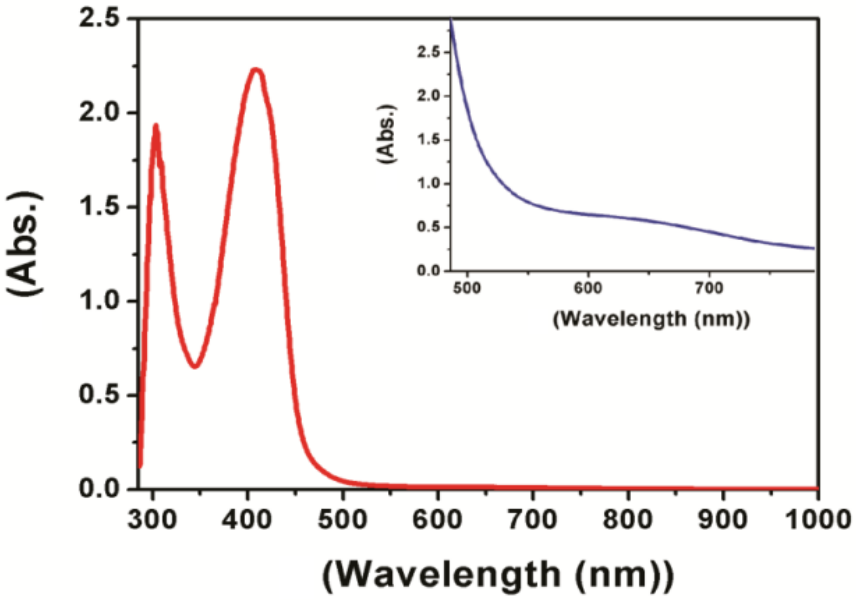

Fig. 11. Absorption spectra of 1×10^{-3} M DMSO solution of the complex **[Cu(L)(NO$_3$)]**.

3.8 Electrochemical studies

The redox properties of this complex were investigated in DMSO (0.003 mL^{-1}) using cyclic voltammetry. Tetra butyl ammonium perchlorate (TBAP) was used as a supporting electrolyte. Cyclic voltammograms were recorded with 100 and 200 mVs^{-1} scan rates vs Ag/AgCl as the reference electrode. This complex shows a redox wave with ΔE_p (E_{pa} - E_{pc}) = 0.172 V and the current I (I_{pa} - I_{pc}) = 1.16µA, with the average formal potential $E_{1/2}$ (E_{pa} + E_{pc} / 2) = 0.08 V. From these features of the redox wave seems to be a reversible electrode process as assigned to the Cu^{II} / Cu^{I} complex [60, 61]. In the CV of this complex at a more negative potential (~ -0.45V), one more reduction wave was seen due to the reduction of ligand moieties (Fig. 12). In general, a transition metal complex has a potential window in between + 0.65 V to - 0.33 V. Such complexes showing reduction potential in this range may be effective superoxide mimic [62]. Observed anodic hump at ~ + 0.95 V revealing that the reduced species is weakly adsorbed on the electrode interface [63].

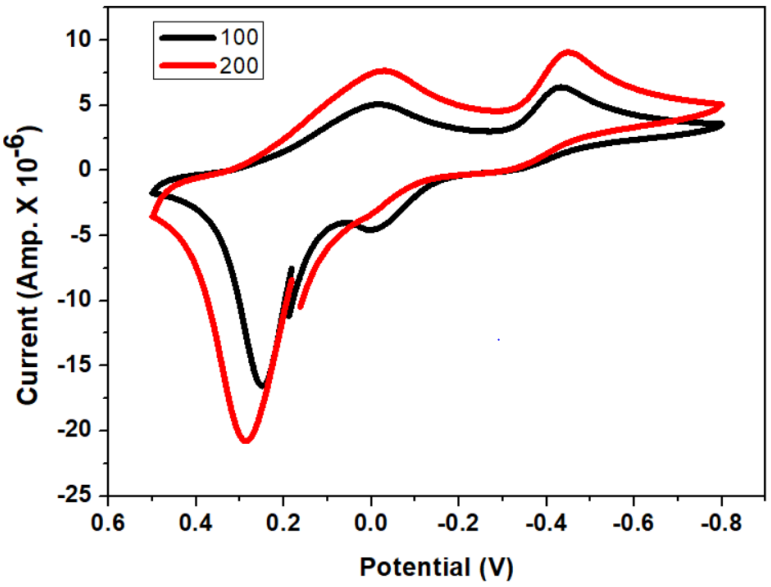

Fig. 12. Cyclic voltammograms of the complex **[Cu(L)(NO_3)]** in DMSO.

3.9 Epr spectral study

Epr spectra of complex recorded in polycrystalline at room temperature and in DMSO solution at liquid nitrogen temperature (LNT). The polycrystalline spectrum (RT) exhibited a broad absorption at <g> = 2 (Fig. 13). The frozen DMSO solution epr spectrum showed the typical four-line patterns expected for coupling of the electron to the 3/2 spin of a copper nucleus. The hyperfine coupling constant ($A_{\parallel}$ = 175 × 10^{-4} cm^{-1}) and g-value ($g_{\parallel}$ = 2.228, $g_{\perp}$ = 2.075) are very close to those found for similar pseudo-tetrahedral copper(II) complexes [64-66]. The estimated g-value is $g_{\parallel} > g_{\perp} > 2.0023$. This is indicative of an S = ½ system with axial symmetry and a $d_{x^2-y^2}$ ground state [67-69].

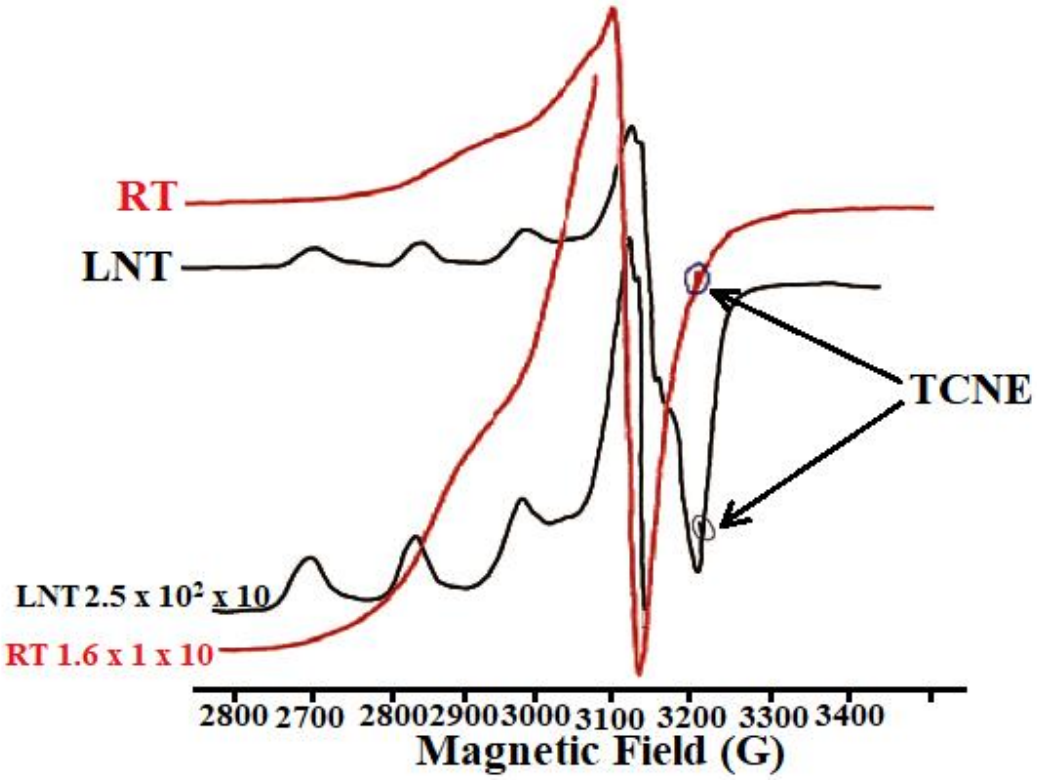

Fig. 13. Epr spectra of the complex **[Cu(L)(NO_3)]**.

3.10 Magnetic moment

Room temperature magnetic susceptibility was examined in the polycrystalline state shows that the present complex is paramagnetic. The observed magnetic moment is in the range expected for a spin-free d^9 (S = ½) system. The observed magnetic moment (μ_{eff}) 1.79 BM is quite close to the value except for complex having one copper ion. The spin-only magnetic moment value is in the range similar to other reported pseudo-tetrahedral copper(II) complexes [70].

3.11 ESI-Mass

ESI-Mass analyses of complexes were performed. The molecular ion peak was obtained at 344.18. The ESI-Mass spectrum of the complex is shown in Fig. 14.

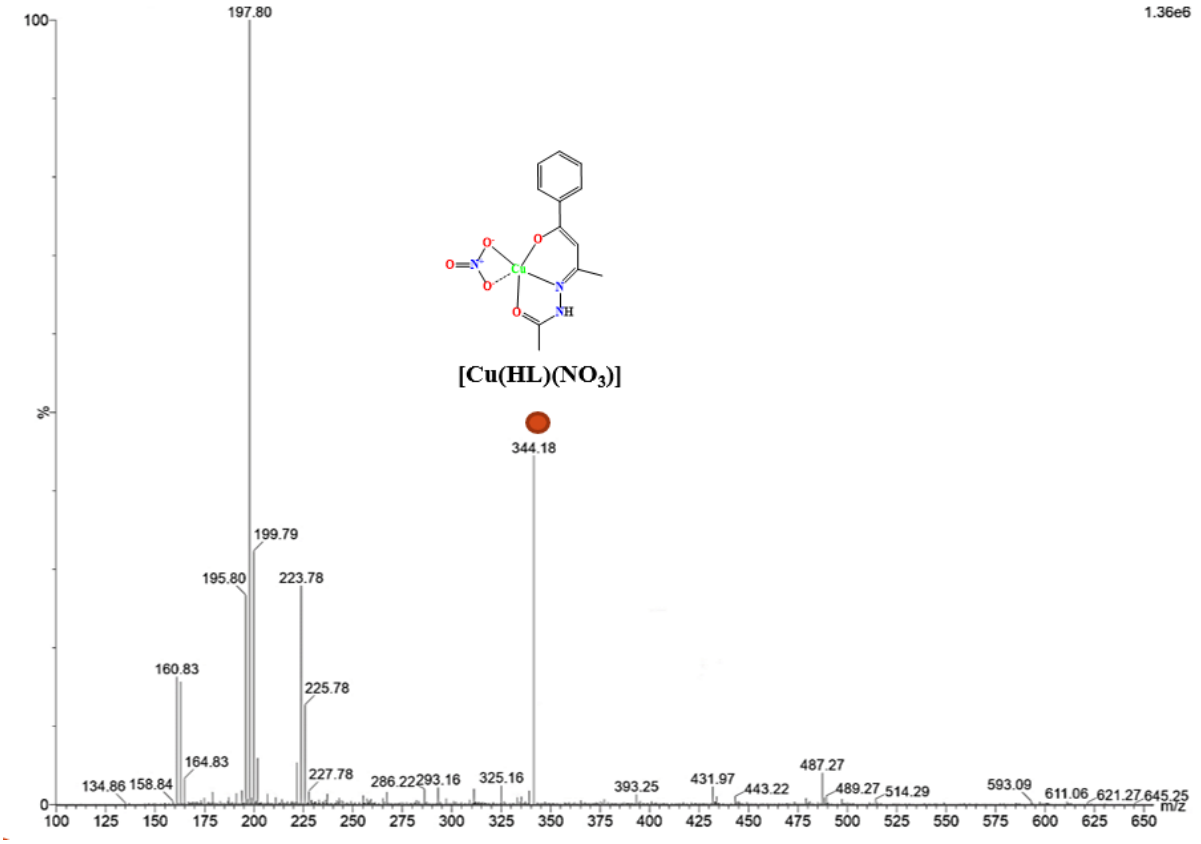

Fig. 14. The ESI-Mass spectrum of the complex**[Cu(L)(NO$_3$)].**

3.12 Antioxidant superoxide dismutase

The *in vitro* antioxidant superoxide dismutase mimetic activity of this complex was measured using the alkaline DMSO-nitroblue tetrazolium (NBT) assay system [71-73]. A plot of percent inhibition of NBT versus concentration of complex is shown in Fig. 15. The concentration (μM) equivalent to the unit of SOD activity (IC_{50} value) 16 μM. As the reaction proceeds, the reduction of NBT to MF^{+} was measured at 560 nm. The estimated IC_{50} value of the present complex is compared with the IC_{50} value of similar mononuclear complexes reported in the literature [74-76]. SOD activity was also evaluated and compared with known systems as shown in Table 4.

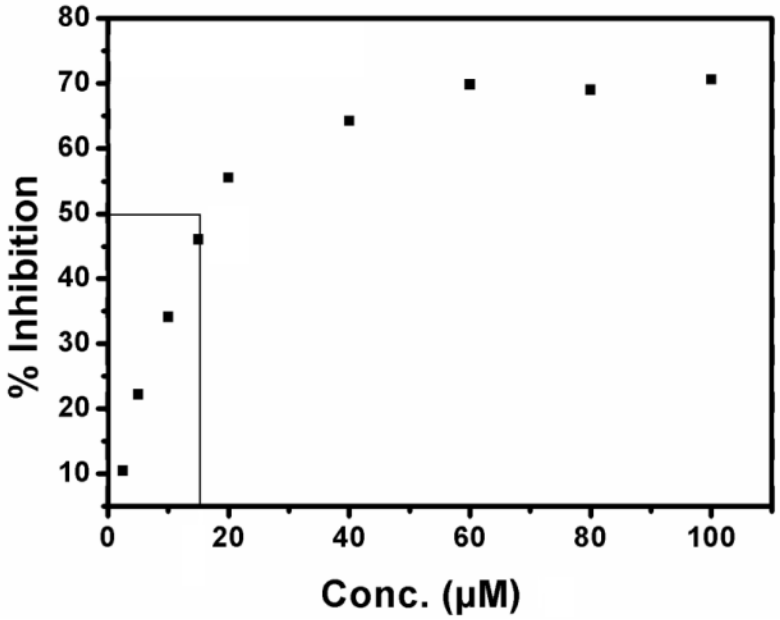

Fig. 15. A plot of % inhibition of NBT reduction vs concentration of complex **[Cu(L)(NO_3)]**.

Table 4 SOD activity data of complex.

S.No.	Complex	IC_{50} (μM)	SODActivity (μM^{-1})	$k_{cat}(M^{-1}S^{-1})$	Reference
1.	[Cu(salicylate)$_2$]	16	16.50	20.79	73, 74
2.	[Cu(acetyl salicylate)$_2$]	23	43.48	14.36	73, 74
3.	[Cu(diisopopropylsalicylate)$_2$]	8.9	112.36	37.37	73, 74
4.	[Cu(L^1)(H_2O)(NO_3)]H_2O	8	125.00	41.58	75
5.	[Cu(L^1)(H_2O)] NO_3	6	166.67	55.44	75
6.	Native Cu–Zn SOD	-	0.04	25000	76
7.	[Cu(L)(NO_3)]	16	62.50	20.79	Present complex

L^1 = 4-chloro-2-{(E)-[2-(pyridin-2-yl)hydrazinylidene]methyl}phenol

The IC_{50} value of the present complex is almost similar to the reported SOD values of complexes. The suggested mechanism of catalytic activity of the present complex is shown in Scheme 3 [77, 78]. This Scheme describes the structural status for various steps of the superoxide anion $O_2^{\cdot-}$ disproportion mechanism. As per the given mechanism first, $O_2^{\cdot-}$ replaces a bound nitrate bind directly to the copper(II) centre and donates its electron. Second, the bound $O_2^{\cdot-}$ exchange rapidly between the axial and planar position of the pseudo tetrahedral, resulting in formation of oxygen molecules (O_2). Third, the oxygen molecule leaves and copper(II) centre reduces to copper(I). Fourth, a second $O_2^{\cdot-}$ attack on copper(II) centre and oxidises Cu(I) to Cu(II). Although these two species remain in equilibrium. As the

proton exchange between the substrate and buffer is a fast exchanging process, the $O_2^{\cdot-}$ further attacks with another proton from the solution to form H_2O_2 molecule. Finally, the pseudo tetrahedral copper(II) reforms and H_2O_2 leaves the systems, completing a catalytic cycle. The catalytic rate constant (k_{cat}) was also evaluated by the equation $k_{cat} = k_{NBT}$, [NBT]/IC_{50}, where k_{NBT} = 5.94 x 10^4 $(ML^{-1})^{-1}S^{-1}$ is the second-order rate constant for NBT [79, 80]. From value of k_{cat} it is clear that this complex can be used as a scavenger. The requirement for SOD activity are a medium strength donor power and flexibility of the used ligands, in order to facilitate the reduction and accommodation of copper(II), which is known to prefer tetrahedral environments [81-83]. The present complex is a pseudo tetrahedral geometry shows acceptable SOD activity similar to other complexes [75-77].

Copper(II) complexes have been reported to exhibit antiproliferative agents [84]. The present mononuclear complex may have similar antiproliferative properties. In this complex copper(II) ion occupies at labile positions of Schiff base and acts according to the established enzymatic mechanism [85-87] (Scheme 3). Thus, presumably, copper(II) centre in complex binds and oxidises $O_2^{\cdot-}$ to molecular oxygen (O_2). The resulting reduced form of the complex may reduce $O_2^{\cdot-}$, which, in presence of protons produces hydrogen peroxide (H_2O_2). Similar results were shown with human cancer cells *in vitro*, which is discussed in other parts of the text.

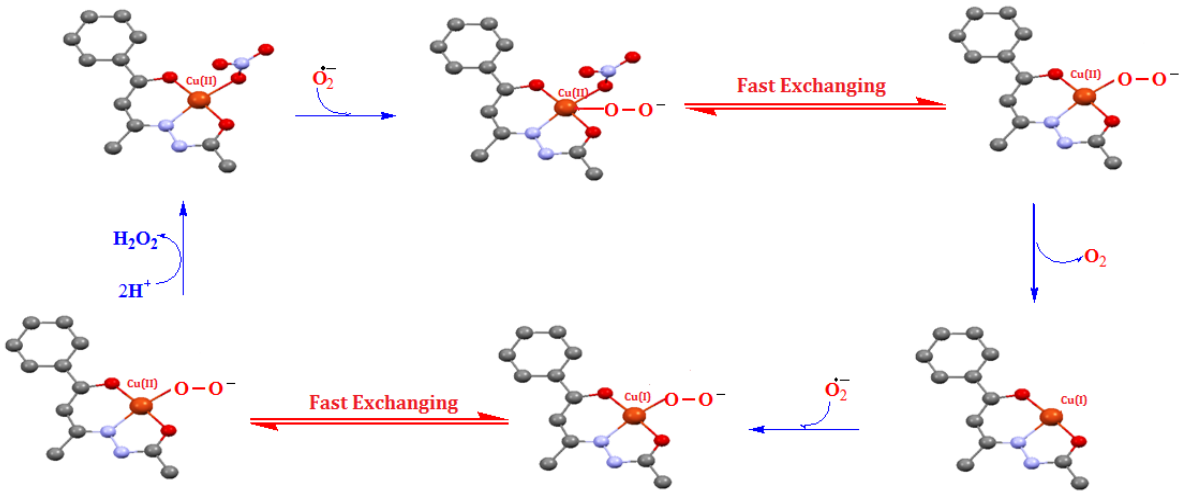

Scheme 3 The suggested mechanism of $O_2^{\cdot-}$ dismutation reaction catalyzed by the complex.

3.13 Anti-cancer activity of complex

3.13.1 Cytotoxicity assay

Anticancerous potential of the synthesized complex was evaluated using cytotoxicity assay. The complex showed considerable cytotoxic activity. After treatment of 24 hours, inhibition concentration 50 (IC_{50}) value was calculated using probit analysis against positive standard Cisplatin. THE derived IC_{50} value was shown in Fig. 16. Comparative effects of treatments *vs* cisplatin on various cell lines are given in Table 5. The complex was efficacious than cisplatin in its effect. HepG2 has shown effective percent inhibition 21.88±1.3µM) among other cell lines used for the study.

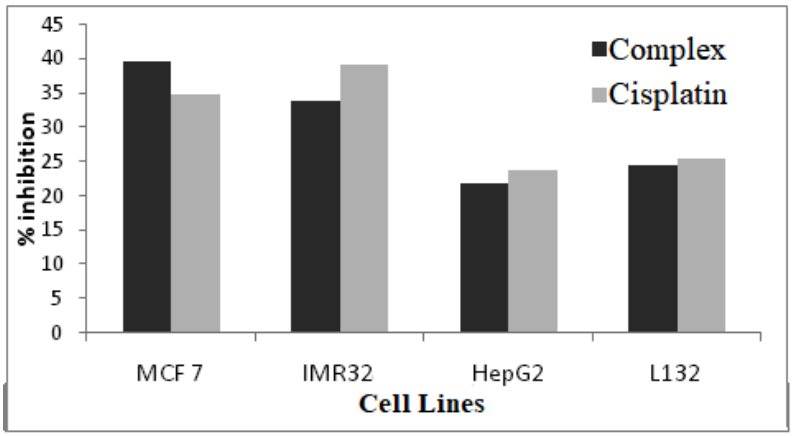

Fig. 16. Showing % inhibition (µM) of cells of various cell lines after 24 hours of synthesized compound treatment.

Table 5 The results *in vitro* cytotoxicity of the complex.

Compound	% inhibition			
	MCF 7	IMR 32	HepG2	L132
Complex	39.5±1.06	33.84±0.19	21.88±1.3	24.38±0.7
Cisplatin	34.59±1.4	38.99±0.78	23.66±2.1	25.33±0.87

3.13.2 Cell death analysis

Cells were treated by complex for 24 hours to observe cell death. Cells were stained by acredine orange (AO) and ethidium bromide (EB). Cells were stained by AO were live cells whereas stained by EB were necrotic cells but apoptotic cells were stained by AO and EB both (Fig. 17).

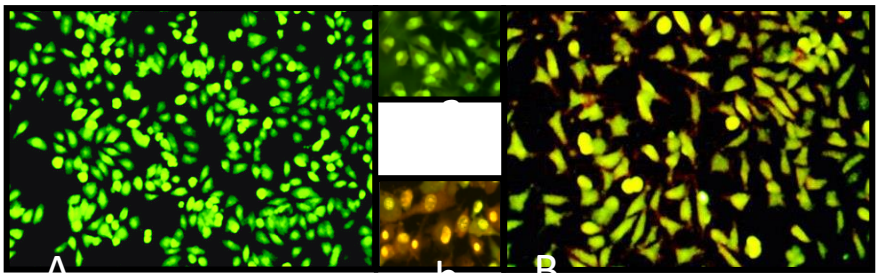

Fig. 17. Showing dual staining of HepG2 cells A) Untreated cells stained by acredine orange (Viable cells), cytoplasm and nucleus emitted green (a) fluorescence, B) Treated cells stained by acredine orange and ethidium bromide both, Inset picture (b) with apoptotic characteristic.

3.13.3 Gene expression study

HepG2 cells were treated by complex for 12 and 24 hours and fold change in expression was calculated. The level of Bax has observed fold increased after treatment of compound whereas expression of Bcl2 was down-regulated (Fig. 16). Furthermore, expression of p53 and caspase 9 were also fold elevated due to treatment of copper complex. Similar anti-proliferative properties were studied on copper(II) complex.

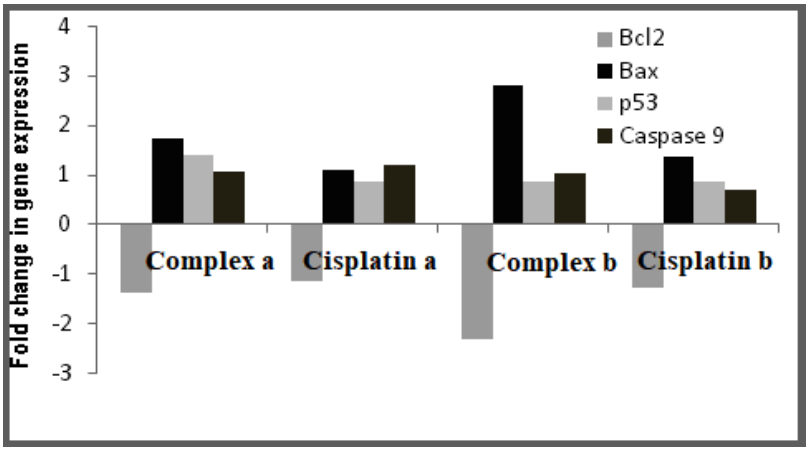

Fig. 18. Gene expression study after 12- and 24-hours exposure of selected compound on HepG2 cell line (a: 12 hours; b: 24 hours).

4 Conclusions

The new mononuclear complex ($Cu(HL)NO_3$) where HL = (N'-[(2E,3Z)-4-hydroxy-4-phenylbut-3-en-2-ylidene]acetohydraziede) was obtained. The Schiff base coordinates

through metal ion via two nitrogen and one oxygen atoms. Hence, Schiff base behaves as a tridentate ligand. The crystallographic data reveal that the metal ion is also coordinated to nitrate ligand forming pseudo-tetrahedral geometry. Such geometry around copper(II) is very less common. We have also characterized complex by various spectroscopic techniques. Spectroscopic features consistence of UV-Vis, IR, CV, Epr, Hirshfeld and XRD data with DFT calculations of four coordinated copper(II) complex used to understand the electronic structure of this pseudotetrahedral complex. The results obtained from DFT calculations have been compared with the experiment and showed good agreement. This complex showed good antioxidant SOD properties. The complex also exhibits good anticancer activity prominent anticancer properties *in vitro*. The antiproliferative properties of this complex have opened the avenues to design and synthesize new members of the same ligand framework to investigate a better anticancer drug.

References

1 J.W.L. Martin, J.H. Timmons, A.E. Martell, P. Rudolf, A. Clearfield, J. Chem. Soc. Chem. Comm. (1979) 999-1000.

2 O.P. Anderson, J. Becher, H. Frydendahl, L.F. Taylor, H. Tofflund, J. Chem. Soc. Chem. Commun. 699 (1936).

3 Y. Murakami, Y. Matsuda, K. Sakata, Inorg. Chem. 10 (1971) 1728-1734.

4 L. Bertini, A. Sigel, H. Sigel, Handbook on Metalloproteins, Marcel Decker, Inc., 2001.

5 A.M. Tondreau, T.J. Duignan, B.W. Stein, V.E. Fleischauer, J. Autschbach, E.R. Batista, J.M. Boncella, M.G. Ferrier, S.A. Kozimor, V. Mocko, M.L. Neidig, S.K. Cary, P. Yang, Inorg. Chem. 57 (2018) 8106-8115.

6 F.G. Herring, D.J. Patmore, A. Storr, J. Chem. Soc. Dalton Trans. 8 (1975) 711-717.

7 R.C. Rosenberg, C.A. Root, P.K. Bernstein, H.B. Gray, J. Am. Chem. Soc. 97 (1975) 2092-2096.

8 S.-K. Kang, H.-S. Kim, Y.-I. Kim, Bull. Korean Chem. Soc. 25 (2004) 1959-1962.

9 R. Malkin, "The copper-containing Oxidase" in Inorganic Biochemistry ed, G.L. Eichhorn Vol. 2., p. 289 (1973).

10 T.B. Chaston, R.N. Watts, J. Yuan, D.R. Richardson, Clin. Cancer Res. 10 (2004) 7365-7374.

11 X. Bao, Y. Xue, C. Xia, Y. Lu, N. Yang, Y. Zhao, Lett. Drug Des. Discov. 15 (2018) 31-36.

12 K. Hrušková, E. Potůčková, T. Hergeselová, L. Liptáková, P. Hašková, P. Mingas, P. Kovaříková, T. Šimůnek, K. Vávrová, Eur. J. Med. Chem. 120 (2016) 97-110.

13 G.M.A. El-Reash, O.A. El-Gammal, A.H. Radwan, Spectrochim. Acta A Mol. Biomol. Spectrosc. 121 (2014) 259-267.

14 C. Fan, H. Su, J. Zhao, B. Zhao, S. Zhang, J. Miao, Eur. J. Med. Chem. 45 (2010) 1438-1446.

15 Y. Gou, Y. Zhang, J. Qi, Z. Zhou, F. Yang, H. Liang, J. Inorg. Biochem. 144 (2015) 47-55.

16 D.D. Perrin, W.L.F. Armango, D.R. Perrin, Purification of Laboratory Chemicals; Pergamon: Oxford, U.K., (1986).

17 G.M. Sheldrick, SHELXS-97, Program for the Solution of Crystal Structures, University of Göttingen, Göttingen (Germany) (1997).

18 G.M. Sheldrick, Acta Crystallogr., A46, (1990) 467.

19 G.M. Sheldrick, SHELXL-97, Program for the Refinement of Crystal Structures, University of Göttingen, Göttingen (Germany) (1997).

20 G.M. Sheldrick, Acta Crystallogr., A64, (2008) 112.

21 E. Prince (Ed.), International Tables for Crystallography, Vol. C, Kluver, Dordrecht 2004, Tables 4.2.6.8 and 6.1.1.4.

22 G.M. Sheldrick, Acta Crystallogr., Sect. A: Fundam. Crystallogr. 71 (2015a) 3–8.

23 G.M. Sheldrick, Acta Crystallogr., Sect. C: Cryst. Struct. Commun. 71 (2015b) 3–8.

24 G.A. Petersson and M.A. Al-Laham, J. Chem. Phys. 94 (1991) 6081–6090.

25 P.J. Hay and W.R. Wadt, J. Chem. Phys. 82 (1985) 270–283.

26 M.J. Frisch, G.W. Trucks, H.B. Schlegel, G.E. Scuseria, M.A. Robb, J.R. Cheeseman, G. Scalmani, V. Barone, B. Mennucci, G.A. Petersson, H. Nakatsuji, M. Caricato, X. Li, H. P. Hratchian, A. F. Izmaylov, J. Bloino, G. Zheng, J.L. Sonnenberg, M. Hada, M. Ehara, K. Toyota, R. Fukuda, J. Hasegawa, M. Ishida, T. Nakajima, Y. Honda, O. Kitao, H. Nakai, T. Vreven, J. A. Montgomery Jr., J. E. Peralta, F. Ogliaro, M. Bearpark, J. J. Heyd, E. Brothers, K. N. Kudin, V.N. Staroverov, R. Kobayashi, J. Normand, K. Raghavachari, A. Rendell, J. C. Burant, S. S. Iyengar, J. Tomasi, M. Cossi, N. Rega, J.M. Millam, M. Klene, J.E. Knox, J.B. Cross, V. Bakken, C. Adamo, J. Jaramillo, R. Gomperts, R.E. Stratmann, O. Yazyev, A.J. Austin, R. Cammi, C. Pomelli, J.W. Ochterski, R.L. Martin, K. Morokuma, V. G. Zakrzewski, G.A. Voth, P. Salvador, J.J. Dannenberg, S. Dapprich, A.D. Daniels, O. Farkas, J.B. Foresman, J.V. Ortiz, J. Cioslowski and D. J. Fox, Gaussian 09, Revision D.01, Gaussian Inc., Wallingford CT, (2009).

27 R. Bauernschmitt, R. Ahlrichs, Chem. Phys. Lett. 256 (1996) 454–464.

28 M. Cossi, N. Rega, G. Scalmani, V. Barone, J. Comput. Chem. 224 (2003) 669–681.
29 T. Mosmann, J. Immunol. 65 (1993) 55-63.
30 Y. Ebrahimipour, I. Sheikhshoaie, A. Crochet, M. Khaleghi, K. M. Fromm, J. Mol. Struct.1072 (2014) 67-76.
31 L. Yang, D.R. Powell, R.P. Houser, Dalton Trans. (2007) 955-964.
32 V. Manivannan, B.K. Dirghangi, C.K. Pal, A. Chakravorty, Inorg. Chem. 36 (1997) 1526-1528.
33 V.Y. Kukushkin, T. Nishioka, D. Tudela, K. Isobe, I. Kinoshita, Inorg. Chem. 36 (1997) 6157-6165.
34 K. Malek, M. Vala, J. Swiatek-Kozlowska, L.M. Proniewicz, New J. Chem. 28 (2004) 477-483.
35 S. Nawaz, A. Ghaffar, W. Zierkiewicz, M.M-ul-Mehboob, Khurram, M.N. Tahir, A.A. Isab, S. Ahmad, J. Mol. Struct. 1137 (2017) 784-791.
36 N. Goel, N. Kumar, J. Mol. Struct. 1071 (2014) 60-70.
37 Nidhi Goel, U.P. Singh, J. Phys. Chem. A. 117 (2013) 10428-1043.
38 G.A. Jeffrey, W. Saenger, Hydrogen bonding in biological structures, Springer-Verlag: Berlin (1996).
39 D. Shoba, S. Periandy, M. Karabacak, S. Ramalingam, Spectrochem. Acta A 83 (2011) 540-552.
40 K. Fukui, Science 218 (1982) 741-754.
41 S. Nawaz, A. Ghaffar, W. Zierkiewicz, M.M. –ul-Mehboob, Khurram, M.N. Tahir, A.A. Isab, S. Ahmad, J. Mol. Struct. 1137 (2017) 784-791.
42 M.A. Spackman, J.J. McKinnon, Cryst. Eng. Comm. 4 (2002) 378-392.
43 M.A. Spackman, P.G. Byrom, Chem. Phy. Lett. 267 (1997) 215-220.
44 J.J. McKinnon, A.S. Mitchell, M.A. Spackman, Chem-Eur. J. 4 (1998) 2136-2141.
45 J.J. McKinnon, M.A. Spackman, A.S. Mitchell, Acta Crystallogr. Sec. B 60 (2004) 627-668.
46 A.L. Rohl, M. Moret, W. Kaminsky, K. Claborn, J.J. McKinnon, B. Kahr, Cryst. Growth Des. 8 (2008) 4517-4525.
47 A. Parkin, G. Barr, W. Dong, C.J. Gilmore, D. Jayatilaka, J.J. McKinnon, M.A. Spackman, C.C Wilson, Cryst. Eng. Comm. 9 (2007) 648-652.
48 S.K. Wolff, D.J. Greenwood, J.J. McKinnon, D. Jayatilaka, M.A. Spackman, Crystal Explorer 2.0; University of Western Australia: Perth, Australia, 2007.
49 J.J. Koenderink, A.J. van Doorn, Image Vision Comput. 10 (1992) 557-564.
50 B.D. Wang, Z.Y. Yang, Q. Wang, T.K. Cai, P. Crewdson, Bioorg. Med. Chem. 14 (2006) 1880–1888.
51 Y.H. Li, Z.Y. Yang, B.D. Wang, Transition Met. Chem. 31 (2006) 598–602.
52 Q. Wang, Y. Wang, Z.Y. Yang, Chem. Pharm. Bull. 56 (2008) 1018–1021.
53 Y.P. Singh, R.N. Patel, Y. Singh, D.C.-Lazarte, R.J. Butcher, Dalton Trans. 46 (2017) 2803-2820.
54 K. Nakamoto, Infrared and Raman Spectra of Inorganic and Coordination compounds, Wiley-Inter science, New York, 3rd edn. (1996).
55 M. Mkaryannis, C. M. Mikulski, L. I. Pytlewski and M. M. Labes, Inorg. Chem., 13,

(1974) 1146–1151.

56 K. Nakamoto, Infrared Spectra of Inorganic and Coordination Compounds, Wiley-Interscience, New York, N.Y., 2nd edn, (1970).

57 D. A. Gangi, R.R. Durand, J. Chem. Soc., Chem. Commun. 9 (1986) 697-699.

58 H. Yokoi, A.W. Addison, Inorg. Chem.16 (1977) 1341-1349.

59 R.L. Belford, M. Calvin, G. Belford, Chem. Phys. 26 (1957) 1165-1174.

60 A.W. Addison, H.M.J. Hendriks, J. Reedijk, L.K. Thompson, Inorg. Chem. 20 (1981) 103-110.

61 C. Liu, J. Cao, W. –T. Deng, B. –H. Chen, J. Chem. Crystallogr. 41 (2011) 806-810.

62 W.–H. Koppenol, F. Levine, T.–L. Hatmaker, J. Epp, J. –D. Ruch. Arch. Biochemistry Biophys. 251 (1986) 594-599.

63 H. Zhou, Z.-H. Peng, Z.-Q. Pan, Y. Song, Q.-M. Huang, X.-L. Hu, Polyhedron 26 (2007) 3233-3241.

64 K. Jeyasubramanian, S. Thambidurai, R. Murugesan, J. Inorg. Biochem. 72 (1998) 101-107.

65 K.H. Lee, W.R. Lee, U.–S. Choi, Bull. Korean Chem. Soc. 15 (1994) 545-549.

66 S.–K. Kang, H.–S. Kim, Y.–I. Kim, Bull. Korean Chem. Soc. 25 (2004) 1959-1962.

67 B.J. Hathaway, D.E. Billing, Coord. Chem. Rev. 5 (1970) 143-207.

68 B.J. Hathaway, Struct. Bonding. 57 (1984) 55-118.

69 E. Garriba, J. Micera, J. Chem. Educ. 83 (2006) 1229-1232.

70 C.J. O'Connor, Prog, Inorg. Chem. 29 (1982) 203-208.

71 R.N. Patel, Y.P. Singh, Y. Singh, R.J. Butcher, M. Zeller, RSC Adv. 6 (2016) 107379-107398.

72 R. Konecny, J. Li, C.L. Fisher, V. Dillet, D. Bashford, L. Noodleman, Inorg. Chem. 38 (1999) 940-950.

73 R.G. Bhirud, T.S. Srivastava, Inorg. Chim. Acta 173 (1990) 121-125.

74 J.E. Weder, C.T. Dillon, T.W. Hambley, B.J. Kennedy, P.A. Lay, J.R. Biffin, H.L. Regtop, N.M. Davies, Coord. Chem. Rev. 232 (2002) 95-126.

75 M.H. Jones, W. Levason, C.A.M. Auliffe, S.G. Murray, D.M. Johns, Bioinorganic Chem. 8 (1978) 201-213.

76 C.T. Dillon, T.W. Hambley, B.J. Kennedy, P.A. Lay, O. Zhou, N.M. Davies, J.R. Biffin, H.L. Regtop, Chem. Res. Toxicol. 16 (2003) 28-37.

77 P.J. Hart, M.M. Balbirnie, N.L. Ogihara, A.M. Nersissian, M.S. Weiss, J.S. Valentine, D. Eisenberg, Bio. Chem. 38 (1999) 2167-2178.

78 I. Bertini, L. Banci, M. Piccioli, C. Luchinat, Cord. Chem. Rev. 100 (1990) 67-103.

79 S. Durot, C. Policar, F. Cisnetti, F. Lambert, J.-P. Renault, G. Pelosi, G. Blain, H.K. -Youssoufi, J.-P. Mahy, Eur. J. Inorg. Chem. 2005 (2005) 3513-3523.

80 Z.–R. Liao, X.–F. Zheng, B.–S. Luo, L.–R. Shen, D.–F. Li, H.–L. Liu, W. Zhao, Polyhedron 20 (2001) 2813-2821.

81 M.P. Quinlan, N. Sullivan, T. Grodzicker, Proc. Natl. Acad. Sci. USA 84 (1987) 3283-3287.

82 L.L. Costanzo, G.D. Guidi, S. Giuffrida, E. Rizzarelli, G. Vecchio, J. Inorg.

Biochem. 50 (1993) 273-281.

83 L.L. Costanzo, G.D. Guidi, S. Giuffrida, E. Rizzarelli, G. Vecchio, J. Inorg. Biochem. 54 (1994) 257-265.

84 C.J.D. Weydert, B.B. Smith, K.C. Kregel, J.M. Ritchie, C.S. Davis, L.W. Oberley, Free Radical Bio. Med. 34 (2003) 316-329.

85 P.J. Hart, M.M. Balbirnie, N.L. Ogigara, A.M. Nersissian, M.S. Weiss, J.S. Valentine, D. Eisenberg, Biochemistry 38 (1999) 2167–2178.

86 S. Mukhopadhyay, D. Mandal, P.B. Chatterjee, C. Desplanches, J.P. Sutter, R.J. Butcher, M. Chaudhury, Inorg. Chem. 43 (2004) 8501–8509.

87 I.A. Koval, P. Gamez, C. Belle, K. Selmeczi, J. Reedijk, Chem. Soc. Rev. 35 (2006) 814–840.

Published Paper from this Chapter

ELSEVIER

Journal of Molecular Structure

Volume 1185, 5 June 2019, Pages 341-350

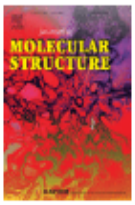

Pseudo-tetrahedral copper(II) complex derived from *N*′-[(2E,3Z)-4-hydroxy-4-phenylbut-3-en-2-ylidene]acetohydrazide: Synthesis, molecular structure, quantum chemical investigations, antioxidant and antiproliferative properties

Abhay Kumar Patel [a], R.N. Jadeja [a] ✉, H. Roy [b], R.N. Patel [c], S.K. Patel [c], R.J. Butcher [d]